ALMA MATER STUDIORUM - UNIVERSITÀ DI BOLOGNA

DOTTORATO IN

INGEGNERIA CIVILE E AMBIENTALE

Ciclo XXVI

Settore Concorsuale di afferenza: 08/B3-TECNICA DELLE COSTRUZIONI

Settore Scientifico disciplinare: ICAR/09-TECNICA DELLE COSTRUZIONI

The effect of two-dimensional squat elements on the seismic behavior of building structures

Michele Palermo

COORDINATORE

Prof. Alberto Lamberti

RELATORE:

Prof. Tomaso Trombetti

CORRELATORE:

Prof. Enrique Hernandez-Montes

Prof. Filip Filippou

Dr. Stefano Silvestri

Esame finale anno 2014

ABSTRACT

This thesis reports a study on the seismic response of two-dimensional squat elements and their effect on the behavior of building structures. Part A is devoted to the study of unreinforced masonry infills, while part B is focused on reinforced concrete sandwich walls.

Part A begins with a comprehensive review of modelling techniques and code provisions for infilled frame structures. Then state-of-the-practice techniques are applied for a real case to test the ability of actual modeling techniques to reproduce observed behaviors. The first developments towards a seismic-resistant masonry infill system are presented. Preliminary design recommendations for the seismic design of the seismic-resistant masonry infill are finally provided.

Part B is focused on the seismic behavior of a specific reinforced concrete sandwich panel system. First, the results of in-plane pseudostatic cyclic tests are described. Refinements to the conventional modified compression field theory are introduced in order to better simulate the monotonic envelope of the cyclic response. The refinements deal with the constitutive model for the shotcrete in tension and the embedded bars. Then the hysteretic response of the panels is studied according to a continuum damage model. Damage state limits are identified. Design recommendations for the seismic design of the studied reinforced concrete sandwich walls are finally provided.

.

ACKNOWLEDGMENTS

I am very grateful to my supervisor Prof. Tomaso Trombetti for his continuous technical guidance and brilliant suggestions during the entire period of my research work in Bologna.

I would like to thank Prof. Enrique Hernandez-Montes, Prof. Luisa Maria Gil-Martin, Prof. Filip Filippou and Dr. Tesser for their guidance during my foreign research periods in Granada and Berkeley.

I am thankful to all my Department colleagues at the University of Bologna (Giada, Simonetta, Sabina, Stefano, Luca) for providing a congenial working atmosphere and sharing ideas.

I also want to thank my parents for their inspiration, although far away from me. Special thanks also to my brother for his constant help and encouragement during these last three years.

To my Parents

Table of contents

List of Figures

List of Tables

1. Foreword

1.1. BACKGROUND AND MOTIVATIONS

Squat structural walls (in particular reinforced concrete walls) and infill walls (in particular unreinforced masonry walls) find wide applications in building structures, especially for low-rise buildings where they may provide a large contribution in carrying the lateral loads due to earthquake excitations.

Despite a large research effort has been devoted to the study of reinforced concrete (RC) slender shear walls since the 1960s with the result of a comprehensive knowledge of their seismic behavior and in detailed design rule and prescriptions aimed at obtaining a desired (high) ductile response, less researches has been focused on the assessment of the seismic behavior of squat walls, which, due to their inherent geometrical aspect (i.e. low aspect ratios), are characterized by a quite complex behavior involving the interaction between flexural, shear and sliding mechanisms of failures due to their inherent aspect ratio. RC squat walls are generally characterized by a "quasi" brittle behavior (substantially different from that of typical RC slender walls which are often analyzed as cantilever beams with a plastic hinge at the base. Moreover, it has been recognized that actual building code equations typically overestimate the peak shear strength capacity of squat reinforced concrete shear walls (Whyte and Stojadinovic 2013, Paulay and Priestley 1982) by factors as large as 2 (from test data compiled by Gulec 2005 design equations were shown to over predict, in the worst cases, the peak shear strength by a factor larger than 3). In fact, in most design codes the formulations to predict the shear strength are typically based on flexural mechanisms of failure rather than shear mechanisms of failure which is proved to be very effective for slender walls. Nonetheless, as already mentioned, squat walls tend to fail in shear and/or in sliding shear because their geometry restricts them from bending easily. Both these shear failure modes are undesirable because they constitute

a quasi-brittle response, such that the structural element loses strength and stiffness rapidly with small increments of inelastic deformation. During the last decades various experimental investigations have been carried out in order to assess the seismic response of squat walls showing a significant scatter not only between experimentally measured and predicted strength but also within different experiments (see the PEER report by Orakcal *et al.* 2006).

Unreinforced masonry is commonly used in frame building structures as infill to either protect the inside of the structure from the environment or to separate inside spaces. The seismic behavior of infilled frame structures involves a complex interaction between the reinforced concrete frame and the unreinforced masonry walls. The topic arose a lot of interest during the last decades and a number of design rules and recommendations have been developed based on theoretical and experimental researches. Nonetheless, recent earthquakes (such as Duzce 1999, L'Aquila 2009, Darfield 2010) confirmed how the interaction between the infills and the frame plays a fundamental rule in the seismic performance of those structures and therefore its deep understanding is crucial for both cases of assessment and retrofitting of existing structures and also for the design of new constructions.

1.2. PROBLEM DESCRIPTIONS AND OBJECTIVES

Based on the introductory discussion, it appears that the assessment of the seismic response of squat two-dimensional elements such as masonry infills and reinforced concrete sandwich walls still represents a challenging task provided that their geometrical configuration determine a complex interactions between (i) flexural and shear behavior for the case of reinforced concrete walls and (ii) reinforced concrete frame and unreinforced masonry infills for the case of infilled frames.

The objectives of the present thesis are to provide insight into the seismic behavior of unreinforced masonry infills and reinforced concrete shear walls (with special attention devoted to reinforced concrete sandwich walls). Both experimental and numerical investigations are necessary for a reliable understanding of the seismic behavior of such elements.

1.3. ORGANIZATION OF THE THESIS

The thesis is organized in two parts: part A and part B. Part A is focused on unreinforced masonry infills and is composed of four chapters (from chapter 2 to chapter 5), while Part B is focused on reinforced concrete sandwich walls and is also composed of four chapters (from chapter 6 to chapter 9).

The objective of part A is to assess the performances of a novel seismic-resistant unreinforced masonry infill system and introduce design recommendations for the seismic design of unreinforced masonry infills. The objective of part B is to assess the seismic performances of reinforced concrete sandwich squat walls with the purpose of introducing design procedures for building structures composed of reinforced concrete sandwich squat walls.

Chapter 2 deals with existing unreinforced masonry infills. First, the main aspects of the seismic response of existing unreinforced masonry infills are briefly described. Then, actual code approaches for the assessment of the seismic response of reinforced concrete frames with masonry infills are discussed. Finally, the expected mechanical properties of existing masonry as obtained from a large literature review are summarized.

State-of-the-practice for the assessment of the seismic response of an existing RC infilled frame is critically discussed in Chapter 3 through a case study dealing with an existing building which collapsed after the 2009 L'Aquila earthquake.

Chapter 4 presents the first developments towards an innovative unreinforced masonry infill of superior energetic and structural properties through the use of traditional materials (clay bricks and mortar) and innovative technologies (nanoparticles and innovative additives) within a national research project. Only preliminary results are presented provided that the research is still under development.

Part A ends with Chapter 5 which provides simple design recommendation for the seismic design of the innovative masonry infills.

In Chapter 6 the structural system objective of the entire Part B of the thesis, made of reinforced concrete sandwich panels and developed during the last two decades by an Italian Firm (Nidyon Costruzioni Srl, http://www.nidyon.net/) through a large experimental campaign, is introduced, with special attention on the description of cyclic tests aimed at assessing the seismic response of both planar panels and of a full-scale 2-story H-shaped structure. A full description of the experimental tests is beyond the scope of the present work and has been the objective of a previous Ph.D thesis (Ricci 2012). Therefore, only the information necessary for a better understanding of the interpretation of the test results are recalled.

Chapter 7 provides an interpretation of the experimental results described in Chapter 5 according to the conventional shear theories for reinforced concrete members (i.e. the modified compression field theory, MCFT (Vecchio and Collins 1986), and rotating-angle softening-truss model, RA-STM (Belarbi and Hsu 1994) and according to the recently proposed refined compression field theory, RCFT (Gil-Martin *et al.* 2009) which has originally proposed for conventional RC walls and is here adapted for the case of the RC sandwich panels.

Chapter 8 provides an interpretation of the experimental results described in Chapter 5 using a concrete damage model developed for the seismic analyses of RC members by researchers at the University of Padua (Tesser *et al.* 2011).

Part B ends with Chapter 9 which provides design recommendations for the seismic design of the studied reinforced concrete sandwich walls.

Finally, Chapter 10 summarizes the main findings of the previous chapters. Recommendations for future research topics are finally provided.

PART A: Unreinforced Masonry Infills

Part A is focused on unreinforced masonry infills and is composed of four chapters (from chapter 2 to chapter 5). Its objective is to assess the performances of a novel seismic-resistant unreinforced masonry infill system and introduce simple design recommendations for the seismic design of unreinforced masonry infills.

2. Modelling of unreinforced masonry infills and relative code provisions for the design of frame structures

2.1. INTRODUCTION

Masonry is one of the oldest construction materials which is worldwide currently in use for reasons that include accessibility, functionality, and cost. It has been used for hundreds of years for the constructions of various civil works from simple roadways to complex monumental buildings. Masonry has also commonly been used in frame building structures as infill, in order to partition the inside of the structure from the external environment or to subdivide internal spaces. In both cases, for long time and still nowadays, it is of common practice to ignore infills during the design and analysis of frame structures. The reluctance of practical engineers to consider the contribution of the infills was due to limited knowledge of the complex interaction between the infills and the frame and lack of practical methods for the prediction of stiffness, strength, and cyclic behavior of the infills. Moreover, the assumption of neglecting the frame to masonry interaction was motivated by the brittle behavior of the masonry panels and was intended to be a conservative assumption.

Extensive research has been done during the last 50 years to determine how the presence of masonry infills influences the in-plane and the out-of-plane behavior of frame structures. Experimental researches on single infilled panels include the works of Benjamin and Williams 1958; Holmes 1963; Stafford-Smith 1968; Moghaddam and Dowling 1987; Dawe *et al*. 1989; Mander *et al*. 1993; Mehrabi *et al*. 1994; Negro and Verzeletti 1996; Durrani and Haider 1996; Pires *et al*. 1998; and Fardis *et al*. 1999b). Studies of tests on multi-story multi-bay s can be found in Liauw and Kwan 1985a; Gergely *et al*. 1994; Mosalam 1996; Mosalam *et al*. 1997a, b. Shaking tests on infilled frame specimens were carried out by Fardis *et al* 1999a, Zarnic *et al*. 2001 and Dolce *et*

al. 2005. These studies provide evaluations of (i) the importance of infill wall confinement from bounding frames, (ii) the types of failure that can be observed in the infill and/or in the frame members, (iii) the stiffness and strength of the infilled frames, (iv) the degradation of strength upon load reversals, (v) the energy dissipated. Based on experimental tests results, a number of models ranging from simple equivalent strut models to more complex nonlinear micro-models, have been proposed through the years for the analyses of infilled frame with masonry infills.

This chapter provides an overview of a number of issues related to masonry infills and their interaction with the surrounding frames, from material properties to code provisions. First, a research dealing with the mechanical properties of actual masonry has been conducted through the analyses of available experimental tests collected from the scientific literature. The aim is to provide expected values to be used for analysis purpose or to compare with the performance of other systems. Then, a review of the fundament analytical models to be used for the analyses of infilled frame structures is given. Finally, some code approaches to the seismic design of masonry infilled RC frame structures are described.

2.2. THE EXPECTED SEISMIC PERFORMANCE OF EXSTING MASONRY INFILLS

The behavior of infilled frames under lateral loadings has been the objective of a number of researchers (Holmes 1961, Stafford-Smith 1962, 1966, 1967, Mainstone and Weeks 1970, Dawe and Seah 1989, Flanagan *et al.* 1992, Mander *et al*. 1993, Wood 1978, Liauw and Kwan 1985, Fiorato *et al*. 1970, Klingner and Bertero 1976, Kahn and Hanson 1979, Bertero and Brokken 1983, Zamic and Tomazevic 1990, Meharabi *et al.* 1994, Colangelo 2005.

These studies have identified a number of complicated failure mechanisms that can be possibly caused by the frame-panel interaction, depending by the infill strength and stiffness relative to the surrounding frame and stiffness. The most typical mechanisms of failure in the case of a strong frame are broadly summarized in Figure 2.1. In the

case of infills stronger than the surrounding frame, columns shear failure, or beam-to-column joints failure may be also observed.

The different mechanisms of failure depend on a number of factors including the geometrical configuration (i.e. the aspect ratio), the mechanical properties of the brick and mortar, the presence of vertical joints fill with mortar, the masonry-to-infill strength and stiffness, the brick-to-mortar strength. Therefore, the knowledge of order of magnitudes of the main mechanical properties for the single components (brick and mortar) and for the masonry assembly is of fundamental importance in order to have reliable prediction of the most probable mechanisms of failure either for the assessment of an existing building or for the design of a new building.

A large literature research has been conducted in order to evaluate expected mechanical properties of the basic components of unreinforced masonry (i.e. clay masonry bricks and mortar) and of small masonry assemblies. The next sections provide a summary of those properties. Most of the data here summarized are available online in the Reluis web site (in the section MADA:MAsonry Database, http://www.reluis.it/index.php?option=com_content&view=article&id=255%3Amada-masonry-database&catid=34%3Anews-reluis&lang=en) and in the master thesis by Raffa 2012.

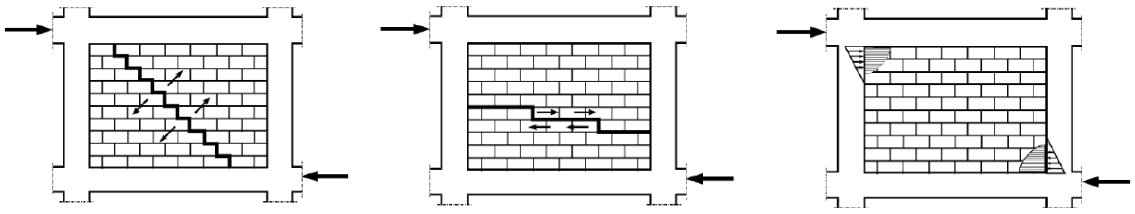

(a) (b) (c)

Figure 2.1: (a) Diagonal shear failure; (b) sliding shear failure; (c) corner crushing.

2.2.1. The mechanical properties of clay brick units

Experimental tests including compression tests and tensile tests on bricks are considered. In detail, only full and hollow clay bricks have been considered. The database containing the list of the references and the data can be found in the Appendix 1. A Large part of the data refers to masonry produced in Italy, either new masonry or existing masonry extracted from existing buildings.

To sum up, the analysis of the data leads to the following observations:

- The average compression strength of hollow clay bricks along the directions of holes and perpendicular to the direction of the holes is equal to approximately 20 MPa and 5 MPa, respectively. Full clay bricks are characterized by an average compression strength equal to 70 MPa.
- The average elastic modulus of hollow clay brick is equal to 10000 MPa, while the average Poisson's ratio is equal to 0.25.
- The tensile strength was measured in very few tests and is equal, on average, to 3.5 MPa.

Note that all the data exhibit a large variability and therefore the values above summarized are only indicative of the order of magnitudes.

2.2.2. The mechanical properties of the mortar

As well known, the mechanical properties of the mortar are strongly dependent on its composition. Different mortar compositions, including hydraulic mortar, aerial mortar, cement-based mortar, high-strength mortar, are commonly used to realize the bed joints of masonry infills. The composition and main properties of the mortar considered in the present study can be found in the database reported in Appendix 1.

To sum up, the analysis of the data leads to the following observations:

- The compression strength of normal mortar (excluding high-strength mortar) is equal on average to 20 MPa, ranging from 2 MPa to 25 MPa. In some cases high-strength mortar exhibit the compression strengths of 60 MPa.

- The average elastic modulus is around 6000 MPa, while the average Poisson's ratio is equal to 0.16.
- The average tensile strength is around 1.5 MPa (from results of direct tensile tests) and 2.2 Mpa (from results of bend test).

2.2.3. The mechanical properties of masonry assemblies

The mechanical properties of masonry assemblies, with special regard to the shear strength, can be evaluated according to different experimental tests which in general may lead to substantially different values of strength, due to different mechanisms of failure which may occur. Actually, two different tests are used to measure the masonry shear strength: (i) triplet test, performed on a small masonry assembly composed of three bricks and two mortar joints (UNI EN 772), (ii) diagonal compression test performed on a small masonry square wall of 1m x 1m dimensions (ASTM E 519).

The works which have been collected in the database reported in Appendix 1 include both results of triplet tests and diagonal compression tests. Details regarding the interpretation of the test results can be found in the work of Calderini *et al*. 2010.

To sum up, the analysis of the data leads to the following observations:

- The average compression strength is equal to 5 MPa.
- The average elastic modulus is around 5000 MPa, while the average shear modulus is around 1300 MPa.
- The average shear strength as obtained from triplet tests is equal to 0.29 MPa, while the average shear strength as obtained from diagonal compression test is equal to 0.33.

2.2.4. Additional observations

The analysis of the data collected in Appendix 1 allows additional observation.

First of all, the main mechanical properties of the masonry assemblies exhibit a large variability due to a number of factors such as:

- Significant variability in the strength and deformation properties of the single components (i.e. brick and mortar);
- thickness of the bed joints;
- the water absorption capacity of both bricks and mortar;
- the geometrical assemblage of the bricks.

By Comparing the performance of contemporary masonry with ancient masonry (through the use of in situ experimental test, e.g. Binda *et al*. 2000) it appears that new masonry are characterized by higher shear modulus (from 2 to 10 times higher) although realized with hollow bricks. On the contrary, the presence of hollow bricks generally leads to a more brittle behavior.

The use of cement-based mortar allows to obtain higher shear strength. The absence of vertical mortar joints significantly reduces the shear strength of masonry assemblies.

2.3. A REVIEW OF THE ANALITYCAL MODELS FOR INFILLED FRAME STRUCTURES

Two different modelling approaches can be found in the scientific literature in order to model the complex interaction between the masonry infill and the surrounding frame: (i) local or micro models and (ii) global or macro models (Crisafulli *et al.* 2010). Micromodels are generally FE models in which the interaction between the infill and the frame is modelled in details. Macromodels are based on a physical understanding of the behavior of the unfilled panel and make use of equivalent trusses to model the effect of the infill with the purpose of reproducing the global effect due to the frame-to-infill interaction in terms of stiffness, strength and hysteretic response.

2.3.1. Macromodels

Current seismic design codes (like EC8 – Part 1, ASCE 41-06) contain provisions for the calculation of the infill stiffness and strength based on the equivalent diagonal strut approach. During the early experimental tests of infilled frame with unreinforced masonry infills, the development of first diagonal cracks in the center of the panel was

observed, with the formation of gaps formed between the frame and the infill in the unloaded diagonal corners of the specimens, while full contact was observed in the two loaded diagonal corners. This behavior, initially observed by Polyakov 1960, led to the introduction of the equivalent compressive strut model.

According to this approach the masonry is modelled as a diagonal strut working only in compression. The strut is generally characterized by a thickness equal to the infill thickness and a width *a*.

The evaluation of the equivalent width, *a*, varies from one reference to the other. The most simple approaches (Holmes 1961, Paulay and Priestley 1992 and Angel *et al.* 1994) suggest the use of constant values of *a* between 12.5 to 33 percent of the diagonal dimension of the infill, with no regard for any infill or frame properties. Stafford-Smith and Carter 1969, Mainstone 1971 and others, derived more complex expressions to estimate the equivalent strut width, *a*, that consider parameters like the length of contact between the column/beam and the infill, as well as the relative stiffness of the infill to the frame. Appendix 3 provides details on the most used formulations to estimate the equivalent strut width, *a*, actually available in the scientific literature.

The equations collected in Appendix 3 for the evaluation of the width of the equivalent strut are to be used for the case of a full infill. In the case of partially infilled frame or perforated infilled frame appropriate reduction factor should be taken into account (Al-Chaar 2002). An alternative way to better account for the presence of openings in the wall makes use of multiple struts which may allow to more accurately account for the actual stress field within the panel and the actions transferred to the surrounding frame. Results of experimental tests conducted on infilled frame with various opening can be found in the work of Asteris *et al.* 2011.

Other reduction factor can be applied to reduce the width of the equivalent truss accounting for various effects such as existing damage (Al-Chaar 2002).

The equivalent strut used to model the masonry infill is pin-connected to the frame elements so that no moment transfer occurs. The stiffness of the strut is governed by

the actual modulus of elasticity of the masonry (E_m) and the cross-sectional area ($a \cdot t_{inf}$, being t_{inf} the thickness of the infill) although studies demonstrated that, in some cases, an effective elastic modulus larger than the actual masonry modulus should be adopted when push-over analyses are performed to better reproduce the experimentally measured initial stiffness of masonry infills (details and practical examples are provided by Al-Chaar 2002). The strength of the strut is determined by the minimum load required to reach either the masonry infill crushing strength (R_{cr}) or the masonry infill shear strength (R_{shear}). The component of these forces in the direction of the equivalent strut will be used to assign the strut a "compressive" strength.

When the equivalent strut model is used to perform non-linear cyclic analyses (cyclic push-over analyses) or non-linear dynamic analyses, an appropriate hysteretic behavior have to be defined, increasing not only the complexity of the analysis but also the uncertainties of the problem. Various hysteretic models have been proposed. Klingner and Bertero 1978 proposed three different hysteretic models of increasing complexity. The envelope curve is composed of a linear elastic branch up to the peak strength followed by an exponentially decreasing branch. Unloading was assumed to be elastic with stiffness equal to the initial stiffness, while stiffness degradation was considered in the reloading phase. The model showed poor agreements against experimental response. Later, similar models where proposed by Andreaus *et al*. 1985 and by Doudomis and Mitsopoulou 1986 assuming slightly different behaviors in the unloading and reloading phases. A different approach was used by Soroushian *et al*. 1988 which proposed an hysteretic model based on an exponential function to define the strength envelope and a polynomial equation to represent the hysteretic loops. Reinhorn *et al*. 1995 proposed a complex mathematical model which makes use of nine parameters in order to provide a smooth force-displacement response and reproduce strength degradation, stiffness decay and pinching. However, the implementation of the model does not appear straightforward, requiring the numerical integration of differential equations. Crisafulli *et al.* 1997 introduced an analytical model for the hysteric response of the equivalent truss based on a number of parameters which have to be experimentally calibrated. More recently, Cavaleri *et al.* 2005 proposed an hysteretic model based on the Klingner and Bertero 1978 model. The modifications

introduced by Cavaleri *et al.* (2005) are: (i) bi-linear slope of the unloading branch before the restoring force vanishes, (ii) new loading branch characterized by a zero value of the restoring force before the system begins to exhibit non zero stiffness; (iii) envelope strength curve for the strut characterized by exponential degrading, according to the experimental results.

It is worth to note that the nonlinear mechanisms which can be reproduced by using the equivalent truss are not able to easily account for important phenomena such as the mechanism of sliding shear or columns shear failure. A detailed description of such nonlinear mechanisms clearly requires the use of more complex models such as micromodels.

2.3.2. Micromodels

Finite elements modelling techniques have been extensively adopted to model infilled frames since the 1960s (Mallick and Severn 1967). The complex interaction between the infills and the surrounding frame requires the use of different elements: beam elements for the frame (beams and columns), two-dimensional elements for the masonry infill and interface elements for the infill-to-frame interaction. Obviously, the use of a complex two-dimensional mesh of finite elements allows a more accurate description of the geometry and a better description of local effects such as cracking, crushing and local interaction, despite an increase in the computational effort.

Generally, two-dimensional membrane elements are enough for in-plane analyses. Most of the material models proposed for masonry infills are adapted from concrete material models. They can be grouped in order of increasing complexity.

The simplest models represent the masonry as an equivalent homogenous material (Danasekar 1984). The presence of the mortar joints is considered in an average or smeared sense. This class of model is suitable for the analyses of large structures in the case of a local stress analysis is not required. Homogenization techniques are required to define the stress-strain behavior of the equivalent homogenous material and appropriate failure criteria have to be introduced.

In the second class of models, the masonry is represented as a two-phase material. Bricks and mortar are modelled with specific material models, while interface elements are used in order to reproduce the brick-to-mortar interface, accounting for debonding, slip or separation. Interface elements are typically modelled as friction elements according to the Mohr-Coulomb theory. This approach clearly requires a large number of elements and a great computational effort and therefore its use is generally restricted the analyses of small specimens, mainly as a research tool.

A balanced compromise between the two approaches is based on the use of two-dimensional elements to model the bricks and interface elements to model the interaction between the mortar joint and the bricks, without explicitly modelling the mortar (Lofty and Singh 1994, Page 1978, Meharabi and Shing 1994). In the first proposed model within this class (Page 1978) the brick is assumed to behave elastically. Later developments considered a more realistic behavior, introducing a non-linear constitutive laws for the bricks, thus allowing to account for the cracking.

In both cases of homogenous models or more complex two-phases models the cracking phenomenon is typically treated using the smeared approach. This model does not keep track of each individual cracks, but rather the effect of cracks is simulated by modifying the stresses and stiffness of the elements. The approach can be considered suitable only in the cases where the behavior is not controlled by few cracks. It has been pointed out (Shing and Mehrabi 2002) that the inclusion of interface elements to account for the development of discrete cracks allows a significant improvement of the accuracy of the numerical results. Nonetheless, the a priori knowledge of cracks location and orientation is required.

2.4. CODE PRESCRIPTIONS FOR THE SEISMIC DESIGN OF MASONRY INFILLS

In this section a review of seismic code provisions for unreinforced masonry infills is given. ASCE 41-06 contains detailed provisions for the evaluation of stiffness, strength and displacement capacity of unreinforced masonry infills. Those provisions are reviewed in section 2.4.1. EC8 does not provide details relevant to the modeling of

masonry infills; on the contrary, it discusses a number of issues related to the infill-to-frame interactions providing design considerations for the frame surrounding the infills. Those specifications are reviewed in section 2.4.2.

2.4.1. ASCE 41-06 approach for the modelling of unreinforced masonry infills

In addition to complex finite element models accounting for the interaction between the infills and the surrounding frame and for the post-yielding behavior of the frame and the cracking of the infills, ASCE 41-06 permit the use of the simple approach based on equivalent struts. The elastic in-plane stiffness of a full unreinforced masonry infill panel prior to cracking can be represented with an equivalent diagonal compression strut of width *a* (Mainstone 1971):

$$a = 0.175\left(\lambda_h h_{col}\right)^{-0.4} D_{\inf} \qquad \textbf{(2.1)}$$

Where λ_h is given by (Stafford-Smith and Carter 1969):

$$\lambda_h = \left[\frac{E_m t_{\inf} \sin 2\theta}{4 E_c I_{col} h_{\inf}}\right]^{0.25} \qquad \textbf{(2.2)}$$

and:

h_{col} column height

h_{inf} infill height

E_m masonry elastic modulus

E_c concrete elastic modulus

I_{col} column modulus of inertia

L_{inf} infill length

D_{inf} infill diagonal

θ strut inclination

The equivalent strut is characterized by the same thickness and elastic modulus of the infill panel it represents. For global structural analysis purposes, the compression struts representing infill stiffness of solid infill panels may be placed concentrically across the diagonals of the frame, effectively forming a concentrically braced frame system. In this configuration, however, the forces imposed on columns (and beams) of the frame by the infill are not represented. To account for these effects, compression struts may be placed eccentrically within the frames. If the numerical models incorporate eccentrically located compression struts, the results should yield infill effects on columns directly. Alternatively, global analyses may be performed using concentric braced frame models, and the infill effects on columns (or beams) may be evaluated at a local level by applying the strut loads onto the columns (or beams).

The expected infill shear strength, V_{inf}, shall be calculated according to:

$$V_{\text{inf}} = A_n f_v \qquad \textbf{(2.3)}$$

Where A_n is the net area of the infill cross section and f_v is the masonry shear strength.

It has to be noted that Eq. (2.3) assumes a unique mechanism of failure, i.e. sliding shear. Therefore, it is recommended to compare the strength as obtained from Eq. (2.3) with the strength associated to the diagonal compression mechanism of failure (Al Chaar 2002).

The non-linear envelope of the strut suggested by ASCE 41-06 is schematically represented in Figure 2.2. Values of the ultimate drift, e, are between 0.5% and 1.2 % depending on the ratio of frame-to-infill strengths, β, and on the aspect ratio (L_{inf} / h_{inf}). Values of ultimate drifts, e, are given in Table 7-9 of ASCE 41-06.

The expected flexural and shear strengths of columns adjacent to an infill panel shall exceed the forces resulting from one of the following conditions:

- The application of the horizontal component of the expected infill strut force at a distance $l_c = a / \cos\theta$ from the top or bottom of the infill panel.
- The shear force resulting from development of expected column flexural strengths at the top and bottom of a column with a reduced height equal to l_c.

The lower-bound of the out-of-plane strength of an infill panel (in pounds per square foot), Q_{out}, shall be determined according to:

$$Q_{out} = \frac{0.7 f_m^{'} \lambda_2}{(h_{\inf} / t_{\inf})} \cdot 144 \qquad \textbf{(2.4)}$$

Where

f'_m masonry compressive strength

λ_2 slenderness ratio (values are given in Table 7-11 of ASCE 41-06)

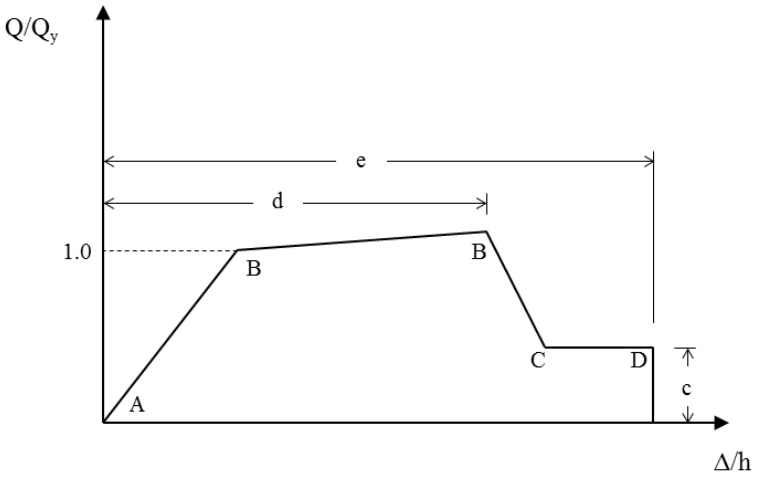

Figure 2.2: Backbone curve representing the non-linear envelope response of the strut

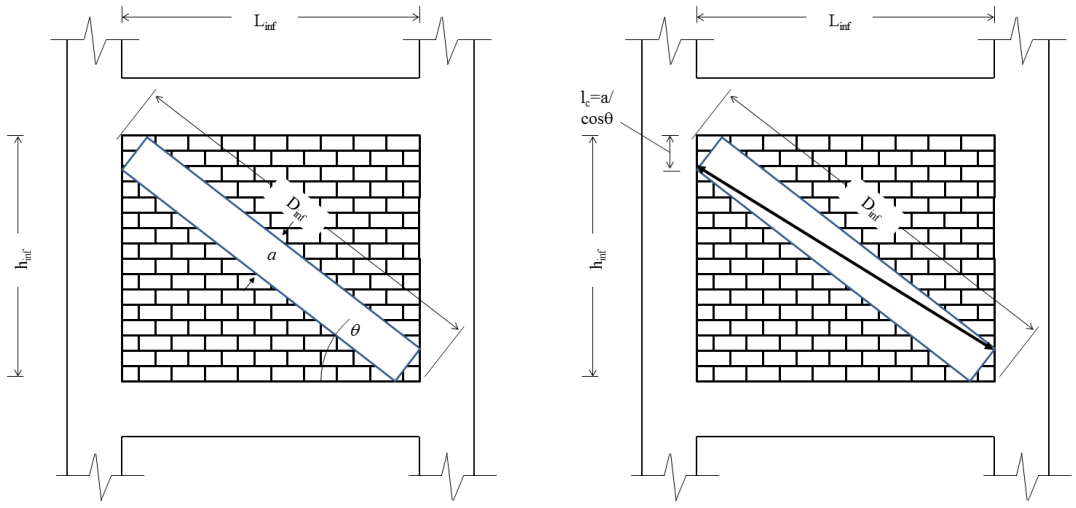

(a) (b)

Figure 2.3: (a) Diagonal strut analogy; (b) Forces applied to the columns

2.4.2. EC8 provisions for infilled frame structures

EC8 does not provide specific indications on the analytical model to be used for infilled structures, although the use of the equivalent strut model is suggested. On the contrary, the following issues due to the infill-to-frame interaction are discussed:

- Fundamental period of infilled frame structures.
- Planar and height irregularities due to an uneven distribution of infills.
- Additional design rules for frame members surrounding the infills.

The fundamental period T_1 of an infilled frame structure can be estimated according to the following equation:

$$T_1 = C_t H^{3/4} \quad \textbf{(2.5)}$$

With:

$$C_t = 0.075 / \sqrt{A_c} \quad \textbf{(2.6)}$$

and

$A_c = \sum A_i \left(0.2 + (l_{wi} / H)\right)^2$ effective area of the masonry infills at the bottom storey.

l_{wi} effective length of the i-th infill at the bottom storey.

E_c length of the i-th infill at the bottom storey.

H building height

In the case of severe special irregularities due to an uneven in-plan distribution of infills it is recommended to use spatial models (i.e. 3D models) for the structural analysis of the building, explicitly including the presence of the infills. The infills with significant openings should be neglected in the numerical model. It is also recommended to perform a sensitivity analysis by varying the location of the infills (e.g. removing some infills, typically the ones at the perimeter) and their mechanical properties. Particular attention has to be given to the design of perimeter frames which

can be affected by significant torsional amplifications (especially those located at the flexible side, the farther from the center of stiffness). To account for these irregularities it is suggested to double the in-plan accidental eccentricity (from 0.5 to 0.1).

In the case of significant irregularities along the height of the building due to the absence or significant reduction of infills it is recommended to increase the effects of the seismic actions. The magnification factor η can be evaluated according to:

$$\eta = \left(1 + \Delta V_{Rw} / \sum V_{Ed}\right) \leq q \qquad \textbf{(2.7)}$$

Where:

ΔV_{Rw} storey strength reduction with respect to that of adjacent storey.

$\sum V_{Ed}$ sum of the seismic force at the considered storey.

q behavior factor.

The local effects on the frame members (beams and columns) due to the infill-to-frame interaction are considered through specific recommendations. It is recommended to assume the entire column height as critical length for the column at the ground level. For the case of partially infilled frame, the following recommendations are given:

- the entire column height has to be assumed as critical height for the design of the stirrups;
- verify in shear a length $l_c = a/\cos\theta$, starting from the beam-column joint, for the smaller of the two design shear forces given by the horizontal component of the diagonal force transmitted by the diagonal truss and the shear corresponding to the column plastic moment (capacity design).

2.5. CONCLUSIONS

This chapter summarizes the main issues related to the seismic behavior of masonry infills. Average mechanical properties of unreinforced masonry infills have been identified through an extended research among the scientific literature. The data have

been organized in a database available in Appendix 1. Then, a review of the fundamental analytical models available for masonry infills has been provided. Finally, code provisions for infilled frame buildings have been bravely presented. All these issues will be used in the next chapters which provide an application of the state-of-the-practice to the analyses of an existing reinforced concrete with unreinforced masonry infills building which collapsed during the 2009 L'Aquila (Italy) earthquake.

3. The influence of masonry infills on the seismic response of reinforced concrete structures: the case of a building in L'Aquila

3.1. INTRODUCTION

This chapter is largely based on a recent work published by the author (Palermo *et al.* 2013) which provides a summary of the results of a joint research work between University of Bologna and Degenkolb Engineers (one of the largest earthquake engineering firm in the United States). The objective of the research work was to study a complex of seven reinforced concrete with masonry infills buildings located in Pettino (northwest of the urban center of L'Aquila), that arose a great interest in the seismic engineering community. Although the seven buildings were built in the mid-1980s adopting similar structural systems, they exhibited quite different responses to the 2009 L'Aquila (Italy) earthquake: two collapsed while the remaining five exhibited moderate to heavy damage.

On April 6, 2009 at 01:32:39 UTC (03:32:39 local time), a magnitude M_l=5.8 (Mw=6.3) earthquake struck a populated area in the Abruzzo region (central Italy). The epicenter was located within 10 km of the urban center of L'Aquila, capital of the region with approximately 70,000 inhabitants. The earthquake was the third strongest recorded in Italy in the last 50 years after the 1976 Friuli (M_w=6.4) and the 1980 Irpinia (M_w=6.9). Further, it is the strongest event providing strong motion records from accelerometer stations located very close to the epicenter (approximately 4-6 km, Bursi *et al.* 2009).

The earthquake caused a total of 305 deaths and 1500 injuries, destroyed or damaged an estimated 10000-15000 buildings, prompted the temporary evacuation of 70000-80000 residents, and left more than 24000 homeless. The building damage extended

over an area of approximately 600 square kilometers, including the urban center of L'Aquila and several villages of the middle Aterno Valley (approximately 5-10 km to the epicenter, ERII Special Earthquake Report, 2009).

Methods for the evaluation of the seismic response of existing building have been proposed since the 1980s (fib Bulletin 24 2003). The most recent international building codes for the seismic assessment and retrofitting of existing buildings (ASCE 41-06 and EC8) suggest approaches based on the introduction of specific limit states and knowledge factors (or confidence factors) accounting for the uncertainty related to the knowledge of the structure. Typically, three different values of the knowledge factor are admitted indicating whether the level of knowledge is "minimum", "usual", or "comprehensive". As far as the method of analysis is concerned, non-linear procedures, such as non-linear incremental static analyses, e.g. push-over analyses (Chopra and Goel 2002) or non-linear incremental dynamic analyses (Vamvatisikos and Cornell 2002) are generally adopted rather than linear approaches (such as linear static analysis or response spectrum analysis), commonly adopted for the design of new buildings. A detailed benchmark for the modeling of existing reinforced concrete frame building can be found in Goulet *et al.* 2007. Performance is quantified in terms of economic losses and collapse safety. The assessment includes site-specific seismic hazard analyses, non-linear dynamic structural response simulations to collapse, damage analyses, and loss estimation. Guidelines for the case of old reinforced buildings designed prior modern seismic design requirements can be found in Manfredi et al. 2007. When the original drawings are not available, the fundamental phase of the methodology proposed by Manfredi et al. 2007 lies in the application of the procedure called "Progetto Simulato", aimed at reconstructing the most probable geometrical and mechanical building details applying the state-of-the-art at the construction time of the building. An application of the EC8 procedures to an infilled reinforced concrete is detailed in Tanganelli et al. 2013.

The objective of this chapter is to investigate the possible reasons leading to the collapse of one of the two buildings which collapsed in Pettino. In detail, the state-of-

the-practice is applied in order to verify if common modeling and analyses techniques are suitable to perform a collapse analysis. The numerical analyses have been conducted according to the ASCE 41-06 procedures, while material properties have been determined following the prescription of the Italian building codes at the time of the design and construction of the studied building.

3.2. OBSERVED DAMAGE OF REINFORCED CONCRETE BUILDINGS

The building damage observed from the L'Aquila earthquake varied substantially depending on the building type, distance from the epicenter, age of construction, condition of the structure. In some locations, there was also evidence of local soil amplification effects (ERII Special Earthquake Report, 2009).

The mainshock caused heavy building damage in the center of L'Aquila, where MCS (Mercalli-Cancani-Sieberg) intensity varied between VIII and IX. Building damage was even more significant in some villages located in the middle Aterno Valley where intensities as high as IX-X were experienced in Castelnuovo and Onna (Table 3.1, from Galli et al. 2009). The effects of soil amplification with high level of damage (VIII) and some collapsed buildings were observed in Pettino, an area located in the northwest area of the center of the city. Figure 3.1 shows the distribution of the MCS intensity in the area struck by the earthquake (available on the INGV web site, http://www.mi.ingv.it/eq/090406/quest.html).

Reinforced concrete buildings in the L'Aquila region performed, on average, fairly well, considering the limited seismic design requirements imposed by the Italian code prior to 2009, and the severe ground shaking, substantially higher than the original design level. The most common damage affected the exterior and interior infills varying from diagonal cracks to out-of-plane failure. However, there were also isolated cases of collapse like the Hotel Duca degli Abruzzi, the student housing observed in the historic center of L'Aquila, and three apartments buildings in Pettino (ERII Special Earthquake Report, 2009).

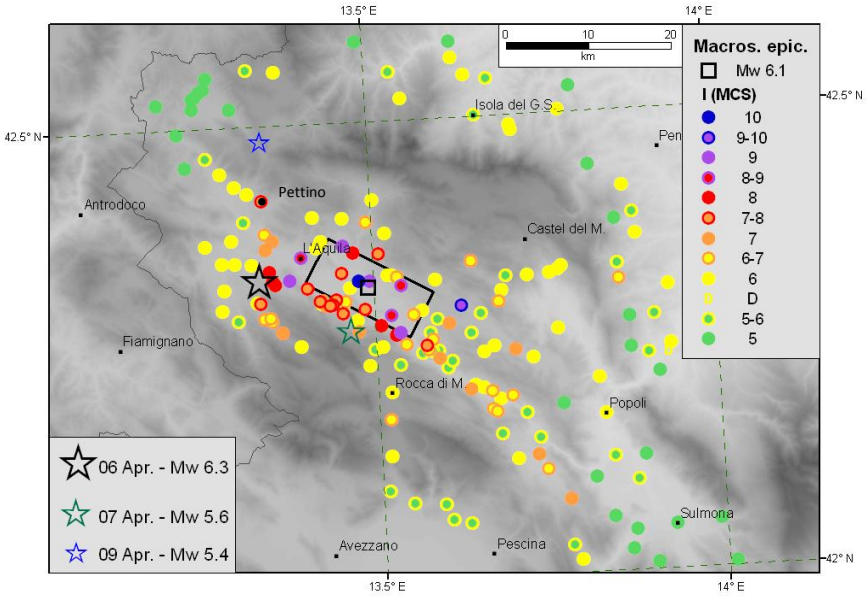

Figure 3.1: Distribution of the macroseismic intensity (MCS scale). Available on http://www.mi.ingv.it/eq/090406/quest.html.

Table 3.1: The highest MCS intensity measure estimated after the 6 April 2009 L'Aquila earthquake in the L' Aquila Province.

Site	City	Lat. [°]	Long. [°]	MCS
Castelnuovo	L'Aquila	42.295	13.628	IX-X
Onna	L'Aquila	42.327	13.460	IX-X
San Gregorio	L'Aquila	42.327	13.496	IX
Sant'Eusanio Forconese	Sant'Eusanio Forconese	42.288	13.525	IX
Villa S. Angelo	Villa S. Angelo	42.269	13.538	IX
L'Aquila centro	L'Aquila	42.356	13.396	XIII-IX
Paganica	L'Aquila	42.358	13.473	XIII
Pettino	L'Aquila	42.325	13.355	XIII

Among these, particular interest has been focused on one collapsed building, part of a residential complex of seven condominiums located in Via Dante Alighieri, Pettino. The seven structures are reinforced concrete with masonry infills buildings of three to four stories constructed in the mid-1980s and consisting of 6 to 9 apartments. The plan is similar for all the buildings including the presence of a porch (pilotis) at the ground level. Despite these similarities, the seven buildings exhibited three different levels of

damage: (A) Collapse; (B) Moderate damage (i.e. Repairable); (C) Minor damage (i.e. Occupable). Specifically, two buildings collapsed with a soft story mechanism at the ground level (level of damage A); two buildings had cracks on the exterior infills and damage to some perimeter columns (level of damage B); three buildings displayed damage concentrated at the lower levels of the exterior infills with cracks near the openings (level of damage C). Figure 3.2 shows selected details of the damaged and collapsed buildings.

(a)

(b)

(c)

Figure 3.2: Global state of damage (left) and particular of damage (right). (a) collapse; (b) repairable; (c) occupable.

3.3. CASE STUDY

3.3.1. Building description

The studied building is one of the two buildings that collapsed in Via Dante Alighieri. It is a four-story condominium built between the late 1970s and 1980s and designed prior to modern day seismic detail requirements. According to the seismic code at the time of construction (D.M. 3/03/1975), a reinforced concrete building located in L'Aquila should be designed for a total lateral force (e.g. base shear) equal to $F_h = C \cdot R \cdot I \cdot W$ (where C=0.07; R=1.0; I=1.0 and W equal to the weight of the building) and corresponding to a design spectral acceleration equal to 0.07 g.

The external dimensions in plan are 25 m x 28 m. The maximum height of the building roof ridge is 12.5 m with the 2nd, 3rd and 4th story, respectively, at 2.8 m, 5.8 m and 8.8 m from the ground level. It is to be noted that: (i) a portion of the first story is built as an open porch; (ii) all the garages are located in the same direction; Figure 3.3 gives the structural plans of the building (the column numbering is given).

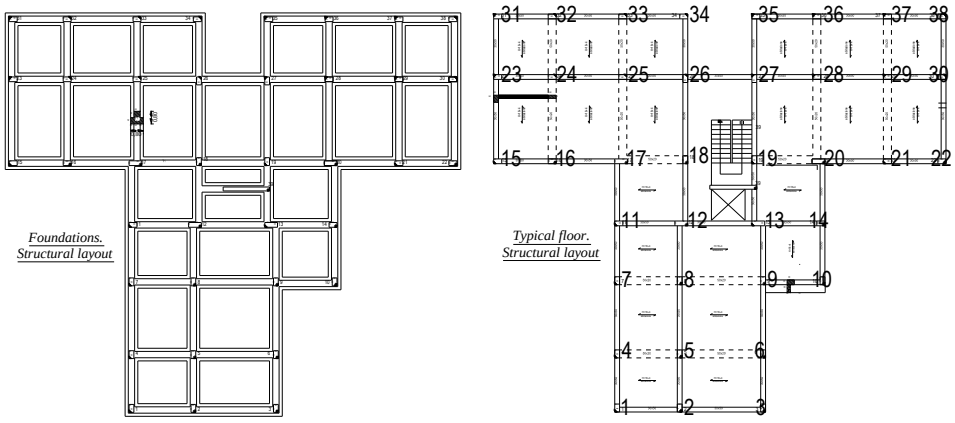

Figure 3.3: structural plan of the building (foundation system on the left, typical floor on the right).

3.3.2. Observed damages

Observation of the collapsed building revealed that: (i) most of the perimeter columns at the ground story failed in shear with some evident buckling of the longitudinal bars (no transverse reinforcement within the joints); (ii) the exterior infills at the ground story exhibited various failure mechanisms (some panels had evident diagonal cracks with corner crushing while others failed due to out-of-plane effects).

The observed damages indicate a soft/weak story mechanism of collapse. Furthermore, it can be observed, from the particular location of the collapsed columns, that the building experienced a significant torsional response. Figure 3.4 gives selected details of the observed damages.

(a)

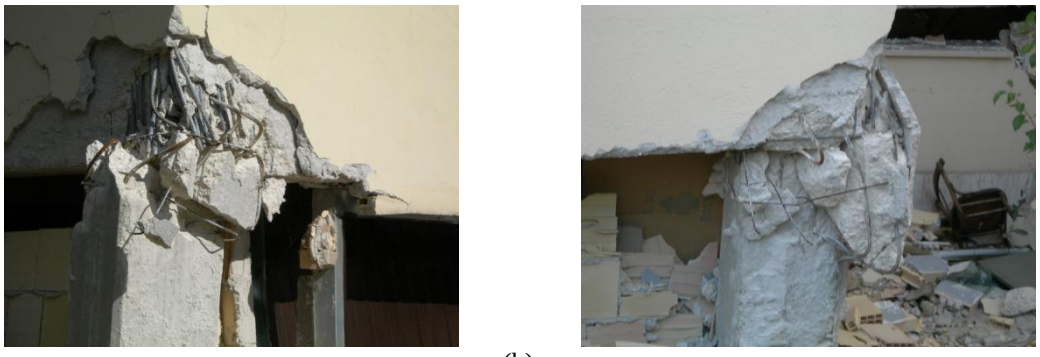

(b)

(c)

Figure 3.4: Damages observed for the studied building. (a) Soft/weak story mechanism; (b) Shear failure in columns; (c) Infills failure.

The geometric and mechanical properties of the structural elements were partially obtained from in-situ measurements and estimated based on the building code at the time of construction (D.M. 26/03/1980, D.M. 3/03/1975). Table 3.2 provides the dimensions and reinforcement of the structural elements as obtained from the in-situ reconnaissance. The nominal shear strength of the typical columns (cross section of 50 cm x 30 cm, see Table 3.2), evaluated according to Eq. 6-4 of ASCE 41-06, is around 150-160 kN, and the most probable expected mode of failure is shear failure (condition iii of Table 6-8 of ASCE 41-06).

Table 3.2: Cross section dimension and reinforcement details for columns and beams.

Structural element	Cross section [cm x cm]	Longitudinal bars [mm]	Ties** [mm]	ρ_L*** [%]	ρ_T*** [%]
Exterior Columns	50 x 30*	deformed -Φ 16	smooth - Φ 8@ 15-20 cm	1.0	0.5-0.7
Interior Columns	50 x 30*	deformed - Φ 16	smooth - Φ 8@ 15-20 cm	1.0	0.5 0.7
Exterior Beams	50 x 30	deformed - Φ 16	smooth - Φ 8@ 15-20 cm	1.0	0.5 0.7
Interior Beams	50 x 30- 20 x 50	deformed - Φ 16	Φ 8@ 15-20 cm	1.0 / 1.6	0.5 / 1.0

*Two columns have a cross section of 80 cm x 30 cm.
** Spacing at column boundaries. Spacing at mid-section is approximately 30 cm.
***ρ_L and ρ_T are the longitudinal and transversal reinforcement ratios, respectively.

The mean compressive strength of the concrete was measured in situ and resulted equal to 20 MPa. Other mechanical properties of the RC elements, which could not be determined experimentally, (i.e. the steel strength/modulus) were evaluated following

the suggestions reported in the work by De Stefano *et al*. 2013 and the specifications and prescriptions of the Italian code at the time of the construction (D.M. 26/03/1980, D.M. 3/03/1975).

The geometric properties of the exterior and interior infills were measured in-situ. The exterior walls consist of a double wythe brick infill, specifically a 10 cm air gap between 12 cm and 8 cm wide brick infill. The interior walls are a single layer of 8 cm wide brick. The bricks are hollow with approximately 60 percent of voids.

The mechanical properties assumed for the masonry are taken from the results of experimental tests performed in L'Aquila on masonry with age and construction similar to the case study (Colangelo 2005) and are summarized in Table 3.3.

Table 3.3: Geometrical and mechanical properties of the exterior and interior infills masonry.

Element	Masonry total thickness* [cm]	Brick dimension [cm x cm x cm]	Number of layers	E_m** [MPa]	f_v*** [MPa]
Exterior Infill	34	24x24x12	2 masonry +1 air	3200	0.35
Interior Infill	8	24x24x8	1 masonry	3200	0.35

*total thickness including the middle air gap
**Masonry elastic modulus
*** Masonry shear strength

3.4. THE INPUT AT THE BASE

The mainshock has been recorded by 57 stations belonging to the "Rete Accelerometrica Nazionale", RAN (national accelerometric network). Among all the available records, the accelerograms recorded by four stations (namely AQA, AQV, AQG, AQK), located at a distance less than 6 km from the epicenter (Mausi and Chiausi 2009, Iervolino and Chioccarelli 2010, Chioccarelli et al. 2009), have been selected to perform the numerical analysis. The case study building is approximately 5 km from the epicenter (Figure 3.5). Details of these four selected records are given in Table 3.4.

Table 3.4: Selected strong motion station with site coordinate, soil type classification (NTC-2008), epicentral distance and PGA recorded.

Code	Name	Lat. [°]	Long. [°]	Soil type	Epicentral Distance [Km]	Recorded PGA [g]
AQV	V. ATERNO-CENTRO VALLE	42.377	13.344	B	4.8	0.66
AQA	V. ATERNO-F. TERNO	42.376	13.339	B	4.6	0.44
AQG	V. ATERNO-COLLE GRILLI	42.373	13.337	B	4.4	0.48
AQK	AQUIL PARKING	42.345	13.401	C	5.6	0.36

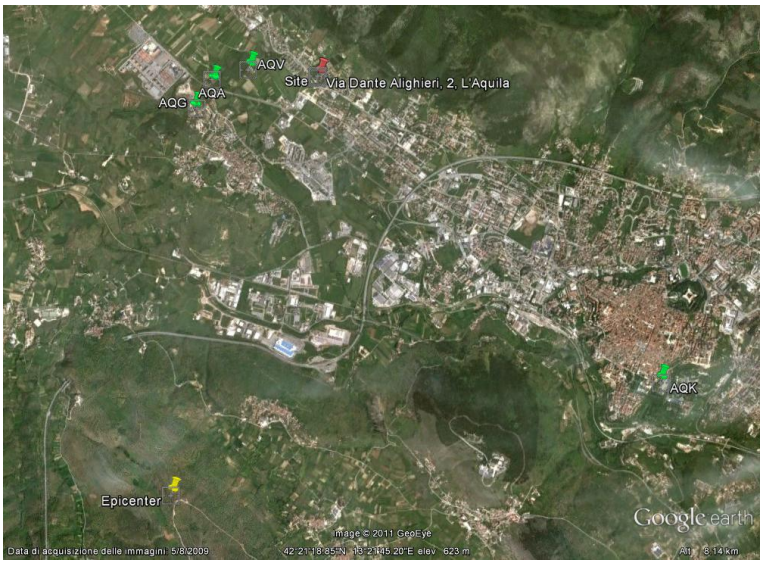

Figure 3.5: Location of the epicenter (marked in yellow), strong motion stations (marked in green) and site of the building (marked in red); from Google Earth.

The four accelerograms were used to obtain an estimate of the base acceleration experienced by the building according to the simple procedure described hereafter.

For each record, as obtained at the k-th station, the corresponding PGA (referred to as PGA_k) was extrapolated. Then, accounting for the soil characteristic trough a soil amplification factor (referred to as AF_k, from L'aquila microzonation map, available on line at http://www.protezionecivile.gov.it/), the PGA at bedrock condition (referred as PGA_k^B) was estimated by dividing the PGA_k by the soil amplification factor AF_k. Each value of d_k (epicentral distance of the k-th station) and PGA_k^B is used to construct an

attenuation curve, assuming the Sabetta- Pugliese (Sabetta and Pugliese 1996) attenuation relationship. Using the Sabetta-Pugliese attenuation relationship, the $PGA_{P,k}^{B}$ (i.e. the PGA at the building epicentral distance) has been estimated.

The mean value of the $PGA_{P,k}^{B}$ over the four stations provides an estimate of the PGA at the site of the building assuming a bedrock condition ($PGA_{P}^{B} = \frac{1}{4}\sum_{k=1}^{4} PGA_{P,k}^{B}$). The resulting mean value of $PGA_{P,k}^{B}$ is equal to 0.408 g. Finally, multiplying $PGA_{P,k}^{B}$ by the soil amplification factor at the building location, AF_P (estimated equal to 1.7 from the seismic microzonation map of the L'Aquila area available on line on http://www.protezionecivile.gov.it), a value of PGA equal to 0.695 g ($PGA_P = \frac{1}{4}\sum_{k=1}^{4} PGA_{P,k}^{B} \cdot FA_P = PGA_P^{B} \cdot FA_P = \frac{1}{4}\sum_{k=1}^{4} PGA_{P,k}$) gives an estimate of the PGA experienced by the building considering the actual soil conditions.

Table 3.5 provides the values of d_k, PGA_k^{B}, $PGA_{P,k}^{B}$, $PGA_{P,k}$ (i.e. $PGA_{P,k}^{B}$ AF_k) and AF_k for each station and the corresponding mean value over the four stations.. It can be noted the mean values of PGA_k^{B} and $PGA_{P,k}^{B}$ are very close (0.412 and 0.408, respectively) due to small differences between stations epicentral distances and the building epicentral distance.

Table 3.5: Values of PGA_k^{B}, $PGA_{P,k}^{B}$, $PGA_{P,k}$, corresponding mean value over the four stations and amplification factor AF_k for each station.

Station	Epicentral Distance, d_k [Km]	PGA_k^{B} [g]	$PGA_{P,k}^{B}$ [g]	$PGA_{P,k}$ [g]	AF_k
AQV	4.8	0.495	0.482	0.819	1.33
AQA	4.6	0.395	0.375	0.637	1.11
AQG	4.4	0.435	0.408	0.694	1.11
AQK	5.6	0.360	0.370	0.629	1.00
Mean	/	**0.412**	**0.408**	**0.695**	/

3.5. THE NUMERICAL MODEL OF THE BUILDING

A number of finite element models were developed using the open source software Opensees, (Mazzoni *et al.* 2006) in order to: (i) understand the factors that contributed to the collapse of the building, (ii) determine if a prediction of failure using current analysis techniques was possible; (iii) evaluate the influence of the column seismic details (i.e. ductility) on the seismic behavior of the building. Despite the possibility to use sophisticated models (available in Opensees), common state-of-the-practice techniques (say for design professionals) have been chosen.

3.5.1. Column shear failure

Columns were modeled using "Beam-Column elements" (Mazzoni *et al.* 2006) and a fiber section to better predict the stiffness of the concrete columns and to include the axial-flexure interaction. "Zero-length elements" (Mazzoni *et al.* 2006) were added at each top and bottom column in order to account for the mechanism of shear failure. A "zero-length element" has two nodes connected by multiple "UniaxialMaterial objects" (Mazzoni *et al.* 2006) placed at the same coordinate, thus leading to an element of null length. A generalized force (i.e. force or moment) vs. displacement (i.e. displacement or rotation) relationship allows to define the behavior of this element. For the specific case, the adopted relation is a shear vs. horizontal displacement (V-d), backbone curve. Two different backbone curves (graphically represented in Figure 3.6) have been adopted for the zero-length elements:

- *Brittle* model;
- *Semi-ductile* model.

The *Brittle* backbone curve is representative of a column expected to experience a shear mechanism (condition iii of Table 6-8 of ASCE 41-06). This behavior is typical of columns designed prior modern seismic requirements, as in the case of the studied buildings. The shear strength, V_n, is estimated as per ASCE 41-06 considering the two

contributions of concrete and transverse reinforcement. The initial stiffness of the curve is equal to the column shear stiffness:

$$K_s = \frac{A_s G_c}{h_{column}} \quad \textbf{(3.1)}$$

where A_s is equal to A_g/χ (where A_g is the gross section area and χ is the shear factor equal to 1.2 for rectangular sections); G_c is the shear modulus of concrete and h_{column} is the length of the columns. A fictitious residual (a numerical artifact) strength V_{res} is assumed to be equal to $0.1V_n$

The *Semi-ductile* backbone curve is representative of a column expected to show a flexure-shear mechanism (condition ii of Table 6-8 of ASCE 41-06). This behavior is typical of columns with light transverse reinforcement (Elwood and Moehle 2005). In this case the backbone curve is characterized by a post inelastic branch that follows the initial elastic behavior, indicating a ductile behavior. The ultimate drift at shear failure has been estimated according to Elwood and Moehle 2005 using the following relationship (semi-empirical):

$$\delta_s = \frac{3}{100} + 4\rho'' - \frac{1}{40}\frac{\nu}{\sqrt{f'_c}} - \frac{1}{40}\frac{P}{A_g f'_c} \quad \textbf{(3.2)}$$

Where ρ'' is the transverse steel ratio, ν is the nominal shear stress, f'_c is the concrete compressive strength, P is the axial load on the column. For a transverse steel ratio between 0.50% and 0.80% (typical at the time of construction of the studied buildings) Equation (3.2) predicts values of ultimate drift between 3.0-5.0% depending on the variation of axial load due to earthquake loading. Note that in Equation (3.2), δ_s represents the displacement of the total column displacement, thus in order to use that equation for the zero-length element it is necessary to subtract the flexural component of the horizontal displacement (δ_{flex}) from δ_s.

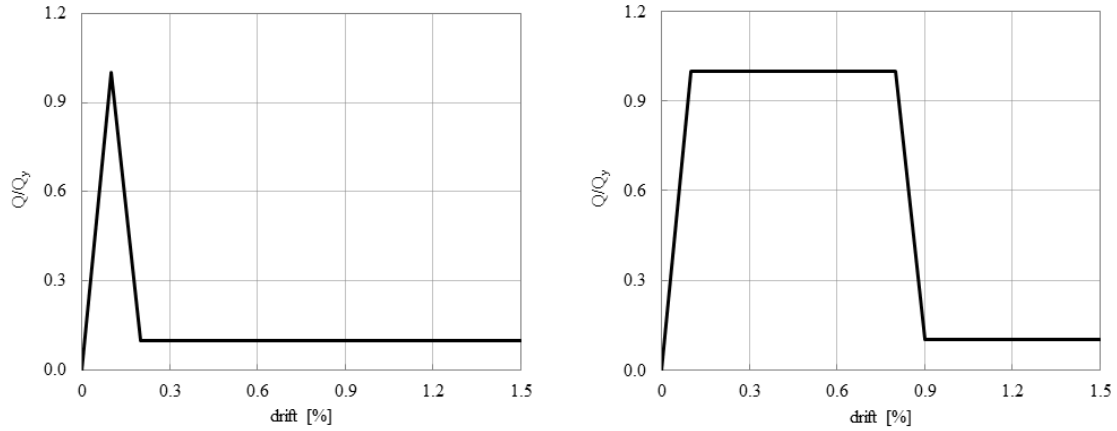

(a) (b)

Figure 3.6: Normalized backbone curves for the zero-length element placed at the top column at the bottom story: (a) brittle model; (b) semi-ductile model.

The infills have been modeled using nonlinear equivalent struts following the general approach proposed by Al-Chaar 2002. It is based on the following steps: (i) evaluation of the equivalent strut width; (ii) evaluation of the strength of the equivalent strut; (iii) evaluation of the inelastic behavior of the strut. The equation used to calculate the equivalent strut width, *a*, of a full panel is based on the conservative approach by Mainstone 1971 which establishes a lower bound of the expected elastic stiffness of the infill (Al-Chaar 2002). For the sake of clearness, Table 3.6 gives the value of the equivalent width, *a*, related to three different amount of opening in the infills. To estimate the effective infill stiffness in a more accurate way, (i.e. less conservatively) an effective masonry modulus $E_{m,eff}$ has been estimated based on experimental data from cyclic tests performed on infill panels built using the same type of brick and technology of those of the studied building (Colangelo 2005). A value of $E_{m,eff}$ equal to $3E_m$ was required to match the experimental data.

Table 3.6: Range of values of the equivalent strut width, *a*.

	Type of opening			
	No opening	Small opening (i.e. window)	Normal opening (i.e. door)	Large opening (i.e. garage)
Equivalent strut width, *a* [cm]	50-60	30-40	20-30	10-20

Where the values calculated are referred to the following properties of the frame/masonry infills:

L_{inf} / h_{inf} = 1.2 -2.2 (ratio between length and height of the infill)
t_{inf} = 18 cm (infill equivalent thickness)
E_m = 3200 MPa

The in-plane strength of the infills (R_{strut}) has been estimated as the minimum between the masonry infill crushing strength (R_{cr}) and the masonry infill shear strength (R_{shear}). The ultimate drift of the infill has been taken from Table 7-9 of ASCE 41-06. The shear failure of the infill occurs when the inter-story drift equals the ultimate drift. As an example, the normalized axial force vs. drift relationship for a particular strut is plotted in Figure 3.7.

Figure 3.8 provides a simple graphical representation of the single infilled frame. It can be noted that two diagonal struts (with no tensile load carrying capacity) are used to model each infill; zero-length elements are placed at the top and bottom end of each column. It is clear that the presence of diagonal struts induces concentrated shear forces at the bottom and top column nodes which may cause brittle shear failures.

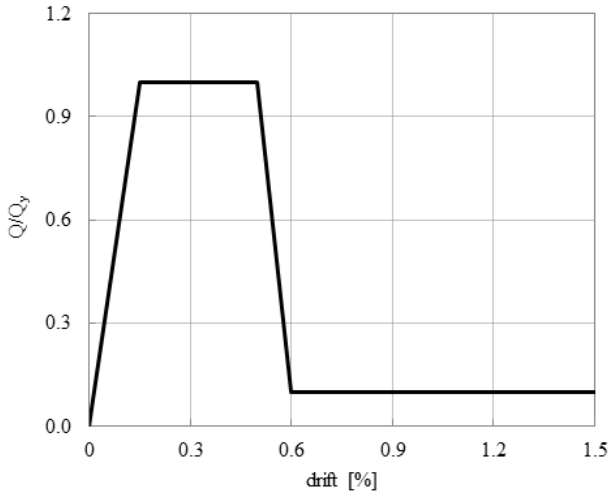

Figure 3.7: Normalized axial force versus drift relationship for a strut modeling a full panel at the bottom story with a length of 5.0, height of 2.8 m and equivalent width equal to 46 cm.

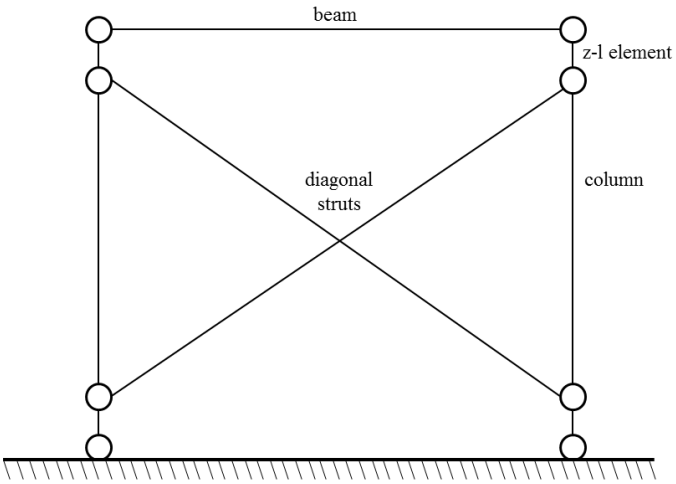

Figure 3.8: Model of the single infilled frame.

3.5.2. The models of the entire building

Three different models of the entire building have been developed with the purpose of investigating the influence of the infills and the influence of the column ductility on the seismic response of the building:

a. *Bare Frame (BF):* Columns, beams and foundations were included in the Opensees (McKenna et al. 2005) model. The infills are not explicitly modeled; clearly, their contribution in terms of mass was included;

b. *Infilled Frame-Brittle (IF-B)*: Infills are explicitly modeled as equivalent struts following the procedure described in the previous section. The backbone curve adopted to represent the column behavior in shear is the *Brittle* model introduced in the previous section;

c. *Infilled Frame-Semi-ductile (IF-D):* Infills are explicitly modeled as equivalent struts following the procedure described in the previous section. The backbone curve adopted to represent the column behavior in shear is the *Semi-ductile* model introduced in the previous section

It has to be noted that all developed models are not able to reproduce a real building collapse, (loss of axial load capacity), since no interaction between shear and axial column strength has been provided. Therefore, the terms "*soft/weak story mechanism*" or "*collapse*", used in the section *Analysis and Results*, will indicate the shear failure of the lateral resisting system (i.e. columns and/or infills).

3.6. ANALYSES CONDUCTED AND MAIN RESULTS

This section presents the main results obtained through the development of: (i) Response History Analysis; (ii) Push-over analysis; and (iii) Incremental Dynamic Analysis. These analyses were developed in order to provide meaningful simulations of what happened in the night of the 6 April 2009. In detail, the two main purposes are:

- The evaluation of the effect due to the presence of the exterior infills on the seismic response of the building.
- The evaluation of the effect of different columns ductility on the seismic response of the building.

3.6.1. Response History Analysis

Response History Analyses (RHA) have been performed on the two infilled models (IF-B and IF-D) using the selected ground motions scaled at a value of PGA equal to 0.7 g which represents an estimate of the PGA experienced by the building during the earthquake. Provided the models exhibited a similar response to the different ground motions, only the response to the AQV record is described.

Figure 3.9 shows the roof displacement response history (i.e. the response of the master node at the roof) observed for the IF-B model and IF-D model, respectively. The peak roof displacements are equal to 7.11 cm (corresponding to a roof drift equal to 0.62%) for IF-D model and 6.16 cm (corresponding to a roof drift of 0.53%) for the IF-B model. The two responses highlight that, while IF-D displacement response comes to zero after the end of the ground shaking, the IF-B response history exhibits a residual

displacement on the x-direction equal approximately to 2 cm, indicating a failure mechanism. A more clear understanding of the different model responses is provided by the comparison of the maximum inter-story drift response history (i.e. the inter-story drift at the master node of each story, Figure 3.10). IF-B interstorey-drift response shows a high concentration of drift at the first story indicating a soft/weak story mechanism, while IF-D inter-story response shows higher drifts at the upper stories (less than the maximum value exhibited by the IF-B response at the bottom story) indicating a more uniform damage distribution along the building stories.

Figure 3.11 (a and c) graphically illustrates the envelope of the maximum first floor displacement for the IF-B model and IF-D model, respectively. It reveals that the IF-B model experiences a significant torsional response due to a progressive "asymmetric" failure of the lateral resisting elements. On the contrary, the envelope of IF-D model does not reveal a significant torsion of the building. Figure 3.11b shows pictures of columns 2 and 15 after the earthquake. Figure 3.12 and Figure 3.13 compares the shear response history of the zero-length elements placed at the top of column 2 and the axial force in a selected strut (the one representing the infill 2) for the two models, respectively. It can be first noted that in the IF-B model the column failed in shear (i.e. the shear in the zero length elements reaches the capacity V_n and then drops to the residual strength, V_{res}), while in the IF-D model the column is able to sustain the loads for all the duration of the ground motion. Moreover it should be highlighted that in the IF-B model column 2 failed just after the failure of the related infill. Table 3.7 provides a qualitative comparison of the damage obtained from the response history analysis and in-situ observation. It can be noted that the IF-B model is able to better simulate the damages experienced by the collapsed building.

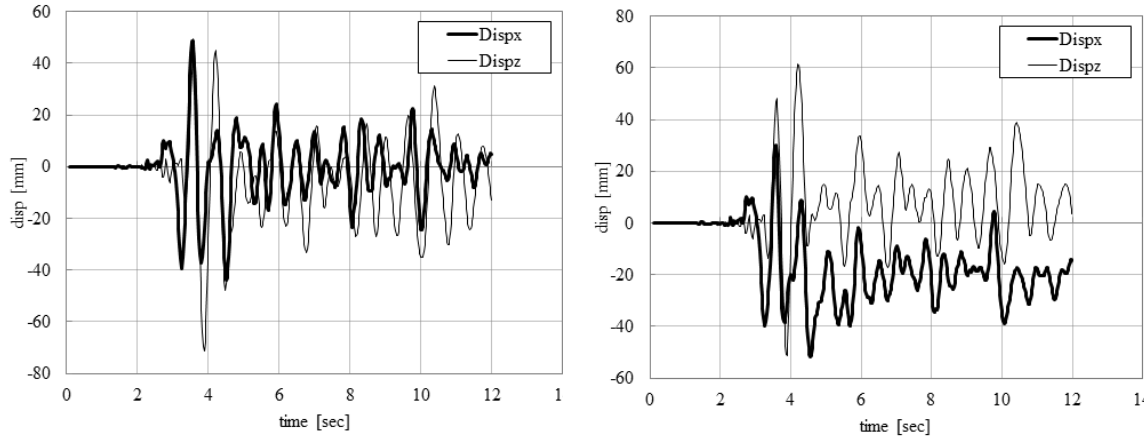

(a) (b)

Figure 3.9: Roof displacement Response History (AQV ground motion): a) IF-B model; b) IF-D model.

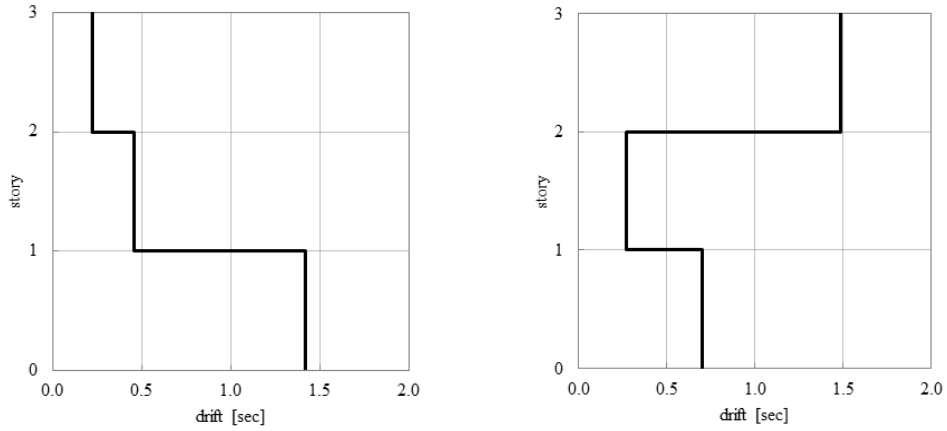

(a) (b)

Figure 3.10: Maximum interstorey-drift (AQV ground motion): (a) IF-B model; (b) IF-D model.

Table 3.7: Comparison of the damages observed from the response history analysis and in situ observations of the collapsed building.

Damage Type	In-situ observation	RHA	
		IF-B	IF-D
Mechanism of collapse (global)	Soft/weak mechanism at 1st story	Soft/weak mechanism at 1st story	Not observed
Column shear failure	At 1st story	At 1st story	Not observed
Infill failure	At 1st story	At 1st story	At 1st and 3rd story

(a) (b) (c)

Figure 3.11: (a) Torsional envelope response of the building from the RHA analysis (AQV ground motion).; (b) photos of the columns marked as 2 and 15 (and circled) after the earthquake; (c) Torsional envelope response of the IF-D model from the RHA analysis (AQV ground motion).

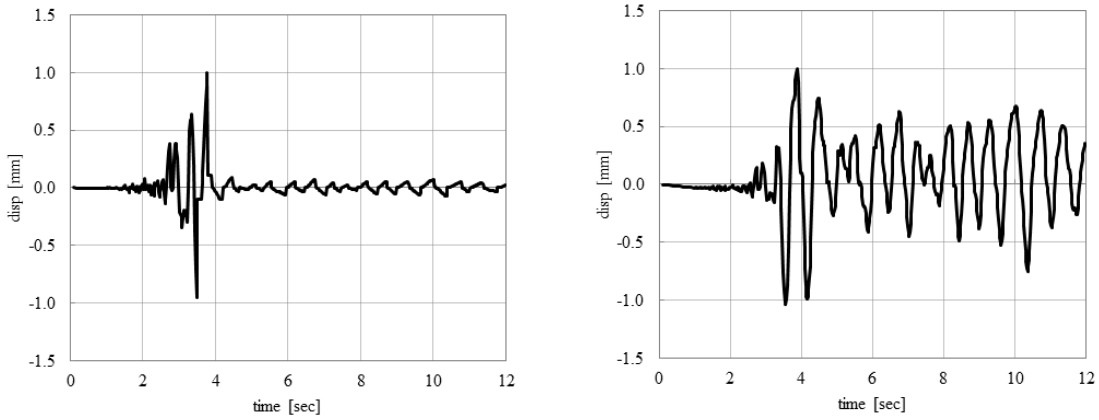

(a) (b)

Figure 3.12: Normalized Shear force Response History for the zero-length element at the bottom story for column 2: (a) IF-B model; (b) IF-D model.

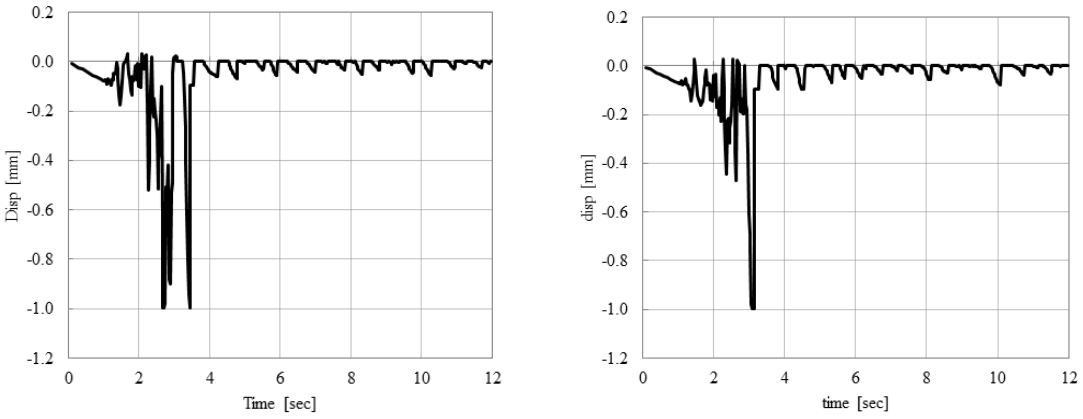

(a) (b)

Figure 3.13: Normalized Axial force Response History for strut 2 (strut 2 represents the infill between the columns indicated as 2 and 3 in Figure 3.3): (a) IF-B model; (b) IF-D model.

3.6.2. Push-over Analysis

Displacement-controlled push-over analyses were performed along both the principal direction of the building (referred to as x and z), with the purpose of evaluating the mechanisms of failure for the different models. For the sake of conciseness, the following discussions focus on the results related to the push-over analyses along the x-direction only. Similar behavior was observed from the analysis along z-direction. The results of the analyses are schematically illustrated by the push-over curves of Figure 3.14, in terms of base shear (V) vs. roof drift, D (i.e. the drift of the master node at the roof level). Critical points (marked with a circle) on the push-over curves are defined as follows:

- Point A (V_A, D_A): indicates the base shear and roof drift at the initial cracking of the infills;
- Point B (V_B, D_B): indicates the base shear and roof drift at the first failure of the infill (where failure occurs when the strut reaches its axial compression strength);
- Point C (V_C, D_C): indicates the base shear and roof drift at the peak strength of the building;
- Point D (V_D, D_D): indicates the base shear and drift corresponding to the shear failure of last lateral resisting elements that failed.

Table 3.8 provides values of the critical points for the three models (k_{in} indicates the initial stiffness of the building measured at a value of base shear equal to 10% of the V_p.).

Table 3.8: Base shear (V) roof drift (D) of the significant point and initial stiffness (kin) from the Push-over curves.

	BF		IF-B		IF-D	
Point	V [kN]	D [%]	V [kN]	D [%]	V [kN]	D [%]
A	/	/	3300	0.04	3300	0.04
B	/	/	5100	0.20	5100	0.20
C	3500	0.73	5470	0.33	5485	0.44
D	2340	0.73	2850	0.50	2760	0.56
K_{in}	70000 kN/m		950000 kN/m		950000 kN/m	

Inspection of the push-over curves for the BF and IFB models highlights that:

- the initial stiffness increases by an order of magnitude;
- the peak strength capacity increases by a factor equal to 55% of bare frame strength (increase);
- displacement capacity at peak strength reduces by 50% of that of the bare frame.

Table 3.9 identifies the progression of significant failure events leading to the failure of the lateral resisting system for the IF-B model. For each event the base shear, the roof drift and the description of the element (or elements) that collapsed, is given. All failures are concentrated at the bottom story indicating a soft/weak story mechanism at the ground floor.

Table 3.9: Numerical values of base shear and roof drift of the main failure events for the IF-B model.

Event number	V_{base} [KN]	D [%]	Failure
B1	5160	0.20	infills @ 1st story
B2	5470	0.33	columns @ 1st story
B3	5080	0.35	columns @ 1st story
B4	4200	0.38	columns @ 1st story
B5	3380	0.43	infills /columns @ 1st story
B6	3090	0.49	infills /columns @ 1st story
B7	2760	0.50	infills @ 1st story

Figure 3.14 compares the response of the two models for the infilled frame (in addition to that of the bare frame). It can be first noted that both models have a similar global mechanism of failure: a progressive failure of infills and columns producing a soft/weak story mechanism at the ground floor. However, although the global strength capacity of the single elements is the same for both the models, the IF-D response exhibits an increase of 7% of strength and 14% of displacement. The higher performance of IF-D model results from a different sequence of failures relative to the IF-B models due to the more ductile shear elements. For the IF-B model, the failure of the infill at the 1st story is observed prior to column shear failure.

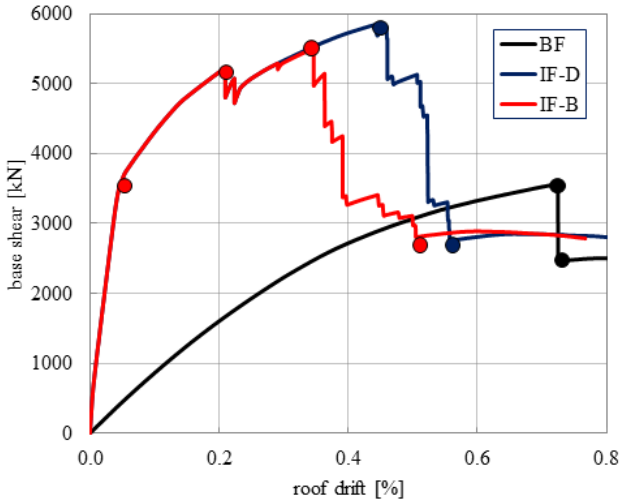

Figure 3.14: Push-over curves for BF, IF-B and IF-D models.

The IF-D model shows infill failure also at the upper stories before the column shear failure at the 1st story. Table 3.10 gives a summary of the sequence of main failure event (vertical drop in the push over curve).

Table 3.10: Numerical values of base shear and roof drift of each failure events for the IF-D model.

Event number	*V* [KN]	*D* [%]	Failure
D1	5160	0.20	Infills @ 1st story
D2	5820	0.43	Infills @ upper stories
D3	5110	0.50	Infills @ upper stories
D4	4530	0.52	Infills /Columns @ 1st story
D5	3290	0.55	Infills /Columns @ 1st story
D6	2760	0.58	Infills /Columns @ 1st story

3.6.3. Incremental dynamic Analysis

Incremental Dynamic Analyses (IDAs) have been developed according to Vamvatisikos and Cornell 2002 aimed at comparing the estimated value of PGA leading to significant building damage relative to the estimated PGA at the site. Each model (i.e. BF, IF-B and IF-D) was subjected to selected ground motions that were

scaled to varying intensity levels (*IM*), thus producing, for each ground motion, a response curve parameterized versus intensity level. The intensity levels, expressed in terms of PGA, vary between 0.10 and 1.10 g. The adopted Damage Measure (*DM*) variable is the peak roof drift. Based on the results of the push-over analysis reported in the previous section, the following four Damage Levels (*DL*), corresponding to the Fully Operational limit state (DL_A), the Operational limit state (DL_B), the Life Safe limit state (DL_C) and the Near Collapse limit state (DL_D), have been adopted:

- DL_A is achieved at a peak roof drift corresponding to point A on the push-over curve;
- DL_B is achieved at a peak roof displacement corresponding to point B on the push-over curve;
- DL_C is achieved at a peak roof displacement corresponding point C on the push-over curve;
- DL_D is achieved at a peak roof displacement corresponding to the point D on the push-over curve;

The values of *DL* adopted for the different models are summarized in Table 3.11. Only the DL_C and DL_D have been considered for the BF model.

Table 3.11: Values of DL adopted for the three models, based on the push-over responses, expressed in terms of roof drift (%).

Model	DL_A	DL_B	DL_C	DL_D
BF	/	/	0.73	0.73
IF-B	0.04	0.20	0.33	0.50
IF-D	0.04	0.20	0.44	0.56

The response of each Single-Record IDA study (Vamvatisikos and Cornell 2002) is a curve (IDA curve) which plots *DM* versus *IM* . For sake of conciseness only the IDA curves related to the AQV records are discussed. Similar results are observed for the other ground motions. Table 3.12 gives a summary of the PGA corresponding to the damage levels DL_C and DL_D that provides an estimation of the PGA that causes the column shear failure of the lateral resisting elements of the three models. IDA curves of the three models are displayed in Figure 3.15.

Table 3.12: Values of PGA corresponding to the damage levels obtained from the IDA analysis.

Model	DL_C	DL_D
BF	0.38g	0.38g
IF-B	0.62g	0.82g
IF-D	0.78g	0.90g

IDA curve of the BF model shows that the BF model reaches the damage levels DL_C and DL_D for a PGA less than 0.40 g. This is an expected behavior for a reinforced concrete building designed prior to modern day seismic requirements.

Inspection of the IDA curve of the IF-B model allows the following observations:

- The first damage level (DL_A), corresponding to the failure of the first infill is reached for a PGA approximately equal to 0.18 g. This indicates that the exterior infills are able to remain in the elastic range up to a level of PGA corresponding to a design PGA which is typical for a low seismic region.
- The second limit state (DL_B) is achieved at a PGA equal approximately to 0.50 g, that is higher than the actual design PGA for common building adopted in Italy (i.e. an earthquake with a return period equal to 476 years)
- The third and fourth damage levels are achieved at a PGA approximately equal to 0.60 g and 0.80 g. In other words according to the IF-F model the building should collapse for a PGA between 0.6 g and 0.8 g. This result is an agreement with the value of PGA that has been estimated at the site of the collapsed building.

Inspection of the IDA curve of the IF-D model allows the following observations:

- The first two damage levels (DL_A and DL_B) are reached at the same PGA of model IF-B. This is an expected behavior because the columns are within the elastic range;
- The third and fourth damage levels are achieved at a PGA equal approximately to 0.80 g and 0.90 g, respectively. This result confirms the significant influence of ductile detailing on the seismic response of the building. Furthermore it can suggest a preliminary possible explanation of the different behavior observed

for the other similar buildings at the site that did not collapse: the presence of possibly more ductile column detailing may have prevented the collapse of the other buildings.

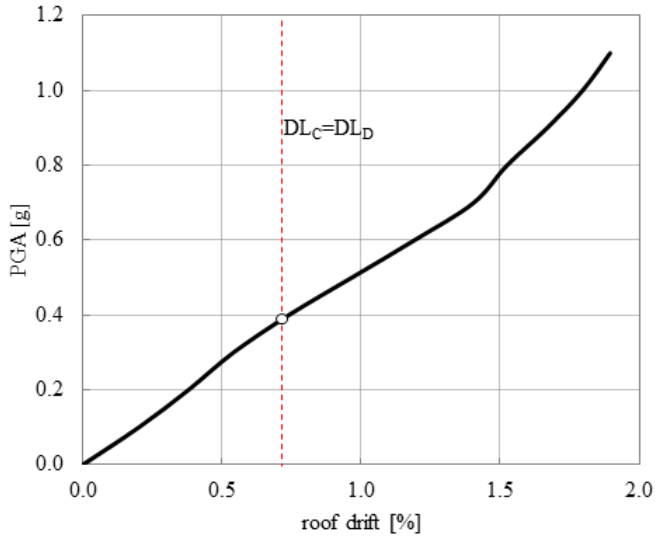

(a)

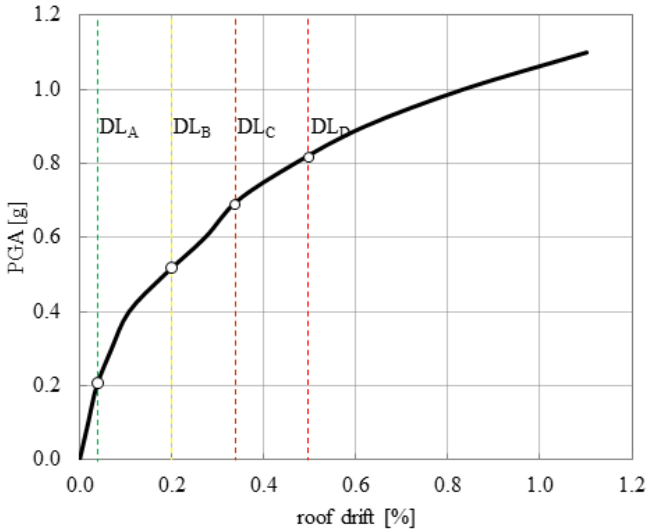

(b)

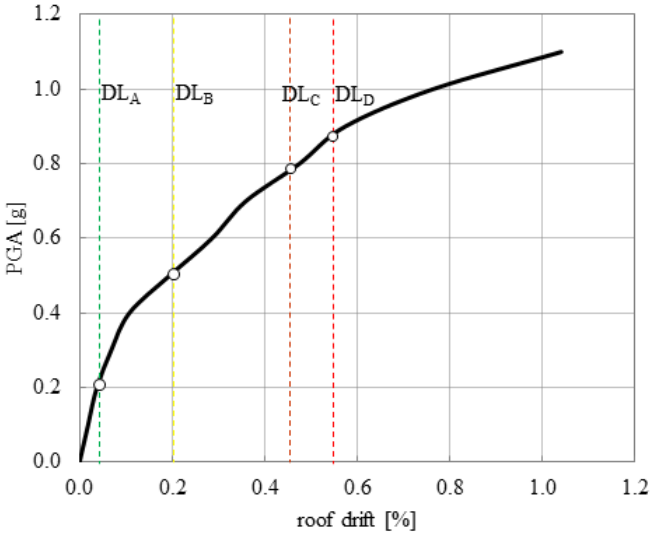

(c)

Figure 3.15: IDA curves for: (a) BF model; (b) IF-B model; (c) IF-D model.

3.7. CONCLUSIONS

This chapter focused on the study of an existing infilled frame with unreinforced masonry building which collapsed after the 2009 L'Aquila earthquake. The building belong to a group of similar seven buildings, two of them collapsed, while the remaining five experienced from low to moderate damage. The main purpose is to investigate the reasons leading to such a different seismic behavior by applying the state of-the-practice techniques related to the analysis of infilled frame buildings. Based on this case study, we can make the following conclusions:

1. The estimated peak ground at the site, based on the application of currently accepted attenuation relationships, along with consideration of the effects soil amplification, was approximately 0.70g (note that this value of ground acceleration is quite larger than the current design acceleration for a reinforced concrete building located in an high seismicity region in Italy, approximately equal to 0.50 g considering the maximum soil amplification factor as per Italian building code). The high value of PGA at the site of the studied building is mainly due to a local soil amplification effect due to the presence of a soft

alluvial layer of soil (as documented from the INGV investigation leading to the microzonation map of the L'Aquila region)

2. Based on the response of the IDAs with a *Brittle* model (representative of a nonductile shear-controlled column with poor confinement detailing), and based on the in-situ measured details on the collapsed building, we could have predicted that the building reached the Near Collapse limit state at a peak ground acceleration of 0.60g. On the contrary performing the IDAs with a *Semi-ductile* model (representative of a less nonductile shear-controlled column with slightly better confinement detailing), we would have predicted that the building reached the Near Collapse limit state at a PGA between 0.80 g and 0.90 g, thus greater than the estimated PGA at the site of the building. Therefore, it is likely that the buildings that collapsed had poorer confinement detailing relative to the buildings that did not collapse.
3. The results of time history analysis performed using the recorded accelerograms scaled at the PGA experienced by the building highlighted that: (i) the *Brittle* model showed a mechanism of failure characterized by a severe torsional response that caused shear failure at select perimeter infill walls followed by column shear failure ending in collapse; (ii) on the contrary, the *Semi-ductile* model showed a mechanism of damage at the exterior infills without the shear failure of the columns.
4. Push-over analyses (as well as IDAs) have been useful in order to confirm two aspects already well known in literature:
    i. Infill panels influence stiffness, strength and global ductility of the building and should not be neglected in the evaluation and retrofit of these types of buildings. As such, an asymmetrical distribution of infill walls will result in a torsional effect that will have an adverse effect on the bare frame response. In detail, for the studied building the overall effect of the infills may be considered as positive provided that it led to a not negligible increase of the strength capacity of the building, if compared to the bare structure which most probably should have

collapsed for a much lower seismic intensity; however, the asymmetric collapse of the perimeter infills most probably contributed to the observed weak/soft story mechanism of collapse.

ii. In the case of light reinforced columns, a slight variation in columns details (e.g. deformed transverse ties versus smooth bars, 90° or 135° hooks, etc.) or also the level of axial load acting during the earthquake will significantly affect the seismic response of the building.

5. Using the most current analysis techniques readily available to the design professional (i.e. a non-linear diagonal strut model for the exterior infills and an appropriate backbone curve for columns shear failure), we were able to predict the building performance that correlated to the observed building damage. In this regard, special care should be taken to use the correct shear failure model (i.e. *Brittle* or *Semi-ductile*) to correctly predict building behavior.

4. The first developments towards a seismic-resistant masonry infill

4.1. INTRODUCTION

Masonry structures and reinforced concrete frame structures with masonry infills represent a large part of the Italian building heritage. The most severe earthquakes which struck the Italian Peninsula during the last decades (Molise 2002, L'Aquila 2009, Emilia Romagna 2012) caused severe damages to infilled RC frame buildings designed prior modern seismic design requirements, thus confirming the brittle nature of the response of unreinforced masonry infills and their adverse influence in the response of the entire building, especially in the case of irregular distributions in plan or height (as previously discussed in Chapter 2).

Nevertheless, although the inherent brittle nature of the masonry response was well known from decades (Hendry *et al. 2003*), the recent tragic failure of RC frame with masonry infills raised awareness among the community, and contributed to the development of national research projects focused on the innovation of the technology of masonry infills, aimed at obtaining superior seismic performances. One of the actual largest national projects (namely "Italici", 2012-105) focused on the innovation of masonry infill is founded by the Ministry of the Economic Development and includes, among several construction firms, the contribution of the Department of civil Engineer at the University of Bologna and in particular of my research group. The research project (still in progress) aims at innovating the entire industrial process, from the product itself (by enhancing selected mechanical properties of the single components, i.e. the clay bricks and the mortar), to the manufacturing plant, to the in-situ installation techniques. The global objectives are ambitious and manifold: (i) reduction of the CO_2 emissions during the industrial process; (ii) superior insulation properties; (iii) superior seismic performances.

Two innovative technologies are to be used in order to accomplish the proposed objectives: (i) the use of nanoparticles mixed in the clay mixture in order to improve the mechanical properties of the clay bricks and to reduce the CO_2 emissions during the industrial process; (ii) the use of a special "additivated" mortar to enhance the seismic behavior of masonry units. The development of each technology is in charge of a specific partner (namely "Nanosurface" for the nanotechnologies and "Litokol" for the additivated mortar).

The expected contributions of the University of Bologna are:

1. identification of the average mechanical properties of traditional masonry infills;
2. identification of the seismic performances of traditional masonry infills;
3. identification of the target seismic performances for the innovative masonry infill;
4. identification of the expected mechanical properties of the single components of the masonry unit (clay bricks and mortar);
5. interpretation of the results of the experimental tests (compression tests, flexure tests, triplets tests) conducted at the single component level on both clay bricks and mortar;
6. interpretation of experimental test results on small masonry wall assemblies (diagonal compression tests) and on full scale masonry infill walls (cyclic shear tests) ;
7. design recommendations for the seismic design of the innovative masonry infill.

Points 1 and 2 have been already discussed in chapter 2 (section 2.2). In the present chapter, first the seismic demand for a typical masonry infill of a typical reinforced concrete frame building is estimated based on a simplified model, by varying the seismic intensity and the number of stories. Then, an overview of the preliminary results of the mechanical characterization of the innovative materials (clay bricks and mortar) is presented. It has to be noted that a detailed description of the material characterization is beyond the scope of present work, provided that the research project is still in progress. Clearly, the final aim of the project is to provide design guidelines

for the innovative infill. On this regard, some design indications will be provided in the next chapter.

4.2. THE EXPECTED PERFORMANCE FOR THE INNOVATIVE MASONRY INFILL

Let us consider an N-story reinforce concrete regular frame structure, as the one schematically displayed in Figure 4.1. It is assumed that the structure is regular in plan and in elevation. It is also assumed that the building present full strong masonry infills along the perimeter (the presence of opening is neglected). It is assumed, conservatively, that the horizontal actions due to earthquake excitations are primarily absorbed by the external masonry. Under those conservative assumptions, the total shear forces at the base of each masonry wall along one side (namely side A and B along the x and y direction. respectively) of the building, $V_{base,A}$ (or equivalently $V_{base,B}$) is simply equal to half of the whole base shear, V_{base}:

$$V_{base,A} = V_{base,\mathrm{B}} = 0.5 \cdot V_{base} = 0.5 \cdot W_E \cdot S_a(\mathrm{T}) \le 0.5 \cdot W_E \cdot F_0 \cdot S \cdot a_g \qquad \textbf{(4.1)}$$

Where:

$W_E = N \cdot W_{story}$ building seismic weigth;

$W_{story} = w \cdot L_x \cdot L_y$ seismic story weight (w is the seismic weight per unit area, L_x and L_y are the building dimensions);

$S_a(T)$ spectral acceleration at period T;

F_0 dynamic amplification factor;

S soil amplification coefficient;

a_g peak ground acceleration on bedrock;

After simple manipulations of Eq.(4.1), the shear per unit length at the base of each external masonry infill can be estimated as follows:

$$v_{base,A} = 0.5 \cdot N \cdot L_y \cdot q \cdot a_g \cdot S \cdot F_0$$
$$v_{base,\mathrm{B}} = 0.5 \cdot N \cdot L_y \cdot q \cdot a_g \cdot S \cdot F_0 \qquad \textbf{(4.2)}$$

By assuming a constant masonry infill thickness t_{inf}, the shear stress at the base of the external masonry infill can be estimated as follows:

$$\tau_{base,A} = 0.5 \cdot N \cdot L_y \cdot q \cdot a_g \cdot S \cdot F_0 / t_{\mathrm{inf}}$$
$$\tau_{base,\mathrm{B}} = 0.5 \cdot N \cdot L_x \cdot q \cdot a_g \cdot S \cdot F_0 / t_{\mathrm{inf}} \qquad \textbf{(4.3)}$$

For the sake of clearness, in order to provide reasonable values for the shear stress at the base of the masonry infills, the following values of the quantities of Eq. (4.3) are assumed:

- L_x=L_y=20m;
- i_x=i_y=5m;
- q=1200 kg/m^2
- F_0=2.5
- S=1.3
- t_{inf}=45 cm

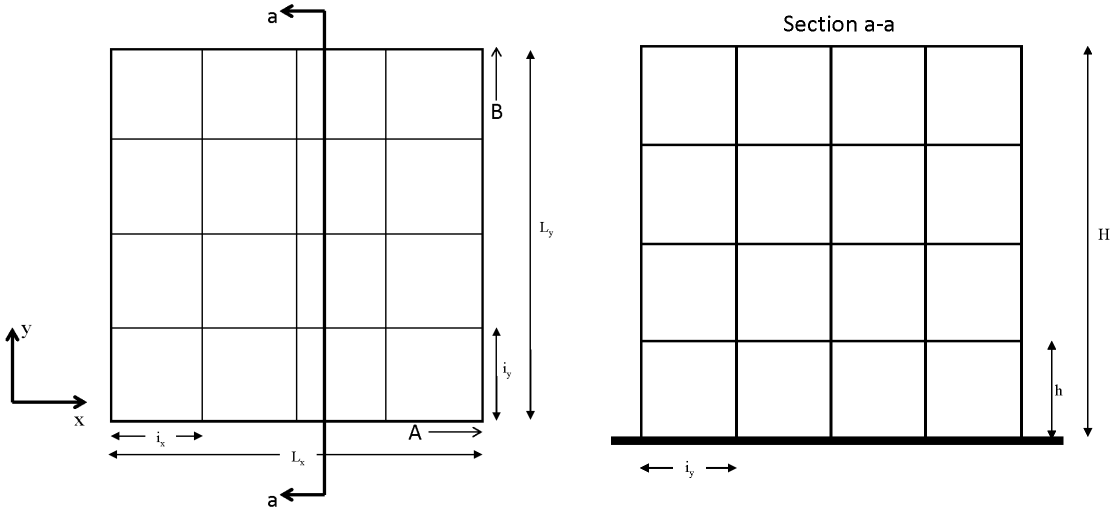

(a) (b)

Figure 4.1: plan view (a) and elevation (b) of atypical regular RC frame building.

Table 4.1 and Figure 4.2 gives the values of the shear stresses (Eq. (4.3)) related to four selected values of a_g (0.05g, 0.15g, 0.25g and 0.35g) corresponding to low, moderate, high and very high seismicity for the Italian regions, respectively, and number of storey *N* varying from 2 to 8.

Table 4.1: Shear stress for selected values of a_g and N from 2 to 10

N	2	3	4	5	6	7	8	9	10
a_g=0.05g	0.09	0.13	0.17	0.22	0.26	0.30	0.35	0.39	0.43
a_g=0.15g	0.26	0.39	0.52	0.65	0.78	0.91	1.04	1.17	1.30
a_g=0.25g	0.43	0.65	0.87	1.08	1.30	1.52	1.73	1.95	2.17
a_g=0.35g	0.61	0.91	1.21	1.52	1.82	2.12	2.43	2.73	3.03

Inspections of Table 4.1 and Figure 4.2 allows the following observations:

- In low seismic regions (a_g=0.05g), the shear stress remains below the average shear strength of traditional infills (which can be estimated around 0.35 MPa, see section 2.2) up to 8-story buildings;
- In moderate seismic regions (a_g=0.15g), the shear stress remains below the average shear strength of traditional infills only up to 2-story buildings;
- In high and very high seismic regions (a_g=0.25-0.35g) the shear stress always exceeds the average shear strength of traditional infills.

Based on the results here discussed, two objectives may be identified for the innovative masonry:

- Increase the shear strength of the masonry assembly. An optimum result could be a shear strength of 1.0 MPa;
- Provide a certain ductility for the masonry assembly. A good result could be a ductility around 2.0

Figure 4.3 schematically compares the elastic (seismic) demand in term of shear stresses with the ductility demand of two equivalents elastic-perfectly plastic systems, with a shear strength of 0.35MPa (representative of a traditional infill) and a shear strength of 1.0 MPa (representative of the innovative infill). Points A, B, D, E represent the following situations:

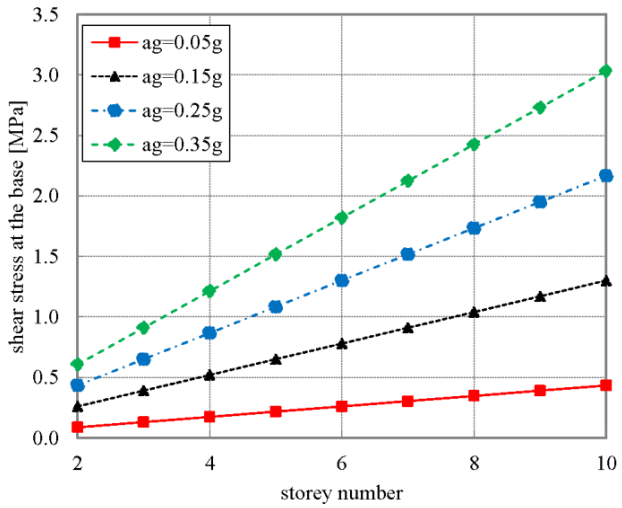

Figure 4.2: Shear stress vs. story number for the different a_g.

- Point A: 8-story building in a low-seismicity region;
- Point B: 7-story building in a moderate-seismicity region;
- Point C: 5-story building in a very high-seismicity region;
- Point D: 8-story building in a very high-seismicity region;

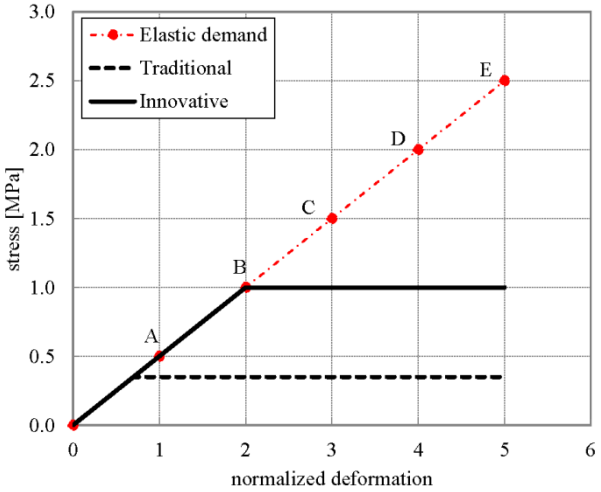

Figure 4.3: Comparison between the elastic demand and the inelastic response for two different shear strength

It should be noted that, also for the innovative infill, a quite ductile capacities (larger than 2) are necessary in order to satisfy the largest seismic demands (say points D and E of Figure 4.3).

4.3. THE FIRST MATERIALS CHARACTERIZATION

During the first two years of the research project experimental material tests has been performed in order to obtain the expected mechanical properties of the single materials (clay bricks and mortar).

Experimental tests on clay bricks include compression tests on small cubes and three point bending tests on small beams. Three different basic formulations (whose chemical mixture has been developed by the research centre "Centro Ceramico") were tested to quantify the effect of: (i) sawdust which is added to increase the material thermal performances (to the detriment of mechanical properties), (ii) alumina-based nanoparticles.

A more complex experimental campaign has been conducted by the partner producing the mortar (Litokol) in order to characterize the innovative mortar mixture. The main purpose is to obtain a ductile mortar. The first candidate for the optimum mixture has been obtained using Design of Experiments (DoE) techniques.

After the characterization of the individual materials, tests on small masonry assemblies (diagonal shear tests) and on full scale infill walls (cyclic shear tests) are to be conducted at the laboratory of Structural and Geotechnical Engineering (LISG) at the University of Bologna.

4.3.1. Experimental characterization of the clay bricks

A first mechanical characterization of the clay bricks has been conducted in the laboratory of the research centre Centro Ceramico. In detail three point bending tests has been performed on small full clay bricks (with dimension of 14x14x60 mm, see Figure 4.4) to measure the material tensile strength and Young's modulus. In addition,

the material densities were measured. A total of 15 different formulations have been analysed. They can be classified into three main groups:

- Type A: Standard
- Type B: Standard + sawdust
- Type C: Standard + nanoparticles

A detailed description of each formulation is beyond the scope of the present thesis. Results of the experimental tests are summarized in Table 4.2. As an illustrative example the stress-deformation response of selected specimens is represented in Figure 4.5. The following observations can be made:

- As expected, the addition of the sawdust (formulation type B) to the standard mixture determines a strength reduction of around 20% and a reduction of the Young's modulus around 30%.
- The inclusion of the nanoparticles (formulation type C) to the standard mixture tends to increase both the strength and the Young's modulus.
- As expected, the strength appears quite correlated to the density (see the graph of Figure 4.6)

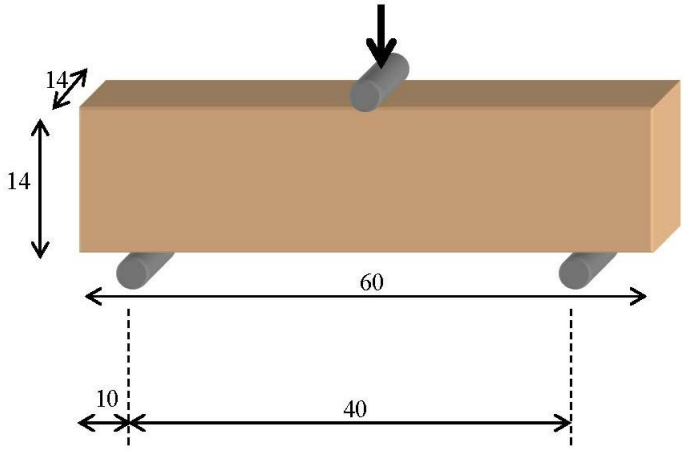

Figure 4.4: Test set up of the bending tests.

Table 4.2: main results of the first experimental tests conducted in the laboratory of the "Centro Ceramico".

Code	Description	Mean f_t [MPa]	f_t (std) [MPa]	Mean E [GPa]	E (std) [MPa].	ρ [g/cm^3]
12/042/C10	A (old lime – essic)	n.d.				
12/042/C10	A (old lime – cook)	11.62	0.68	2.75	0.19	1.60
12/042/C13	B (old lime + 3% sawdust – dry)	6.35	-	1.37	-	
12/042/C13	B (old lime + 3% sawdust – cook)	10.49	0.40	2.50	0.21	1.45
12/042/C12	B (old lime + 0.75% nano1 – dry)	6.95	0.40	1.80	0.21	
12/042/C12	B (old lime + 0.75% nano1 – cook)	12.19	0.66	3.05	0.22	1.59
12/071/C10	A (new lime – dry)	6.95	0.52	1.62	0.30	
12/071/C10	A (new lime – cook)	13.91	0.75	3.25	0.35	1.59
12/071/C11	A (new lime +5% sawdust – dry)	6.65	0.74	1.35	0.15	
12/071/C11	A (new lime +5% sawdust – cook)	11.49	0.99	2.44	0.29	1.40
12/071/C12	B (new lime +3% nanoA – dry)	5.18	0.45	1.56	0.46	
12/071/C12	B (new lime +3% nanoA – cook)	13.09	1.17	4.00	0.21	1.57
12/071/C13	C (new lime +3% nanoB – dry)	4.49	0.47	1.25	0.41	
12/071/C13	C (new lime +3% nanoB – cook)	12.67	1.46	3.59	0.54	1.59
12/071/C14	C (new lime +3% nanoC – dry)	5.92	0.80	1.63	0.30	
12/071/C14	C (new lime +3% nanoC – cook)	15.73	1.28	4.08	0.57	1.61
12/071/C15	C (new lime +3% nanoC – dry)	6.06	0.75	1.57	0.30	
12/071/C15	C (new lime +3% nanoC – cook)	15.75	0.90	4.44	0.60	1.62

After the preliminary tests conducted by the Centro Ceramico further experimental tests were carried out in the laboratory of Structural and Geotechnical Engineering (LISG) at the University of Bologna. Experimental tests include compression tests on small cubes (nominal dimensions of 3x3x3 cm) and three point bending tests on small beams (nominal dimensions of 3x3x10 cm). The tests were performed on three selected formulations:

- Standard (with new lime)
- Standard (with new lime) + 5% sawdust

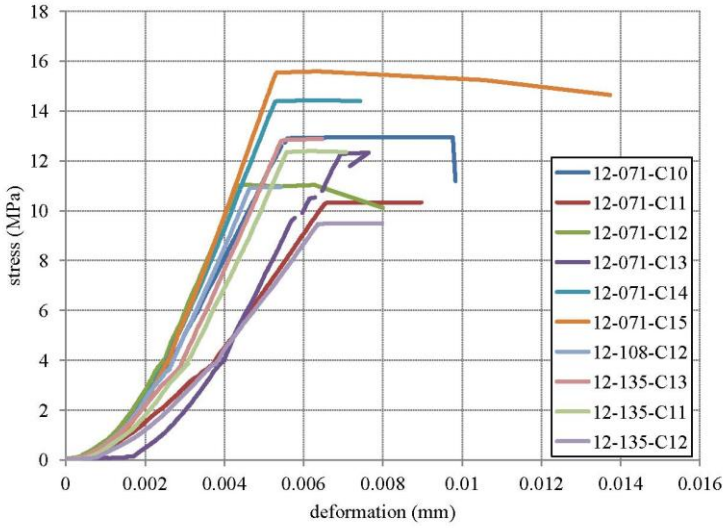

Figure 4.5: stress-deformation response of selected specimens.

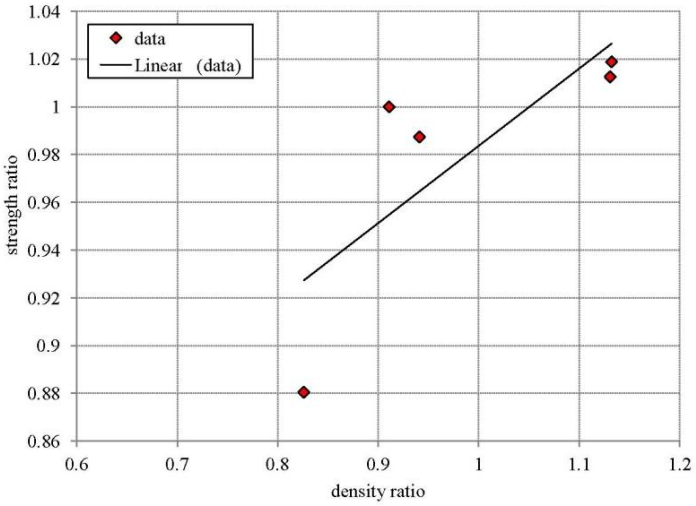

Figure 4.6: the correlation between strength and density.

- Standard (with new lime) + 5% sawdust+ 6% nanoparticles

A total of 10 specimens of each formulation have been tested. Further details are given in Appendix 2. The mean values and coefficient of variations (COV) of the compression and tensile strength as obtained from the tests are collected in Table 4.3. It can be noted that the presence of the sawdust determine a substantial reduction of both the compression strength (around 30%) and the tensile strength (around 45%). The

addition of the nanoparticles (together with the sawdust) does not seem to provide significant benefit to the main mechanical properties.

Table 4.3: Main properties as obtained from the experimental tests performed at the LISG lab.

Mixture	Mean f_c [MPa]	COV f_c [MPa	Mean f_t [MPa]	COV f_t [MPa	ρ
1	58.6	0.20	26.8	0.11	0.26
2	38.1	0.13	14.2	0.12	0.78
3	34.4	0.11	15.2	0.11	1.30

4.3.2. Experimental characterization of the innovative mortar

A large experimental campaign has been conducted in the laboratory of "Litokol" in order to provide the optimum mixture of the innovative mortar.

The optimal mixture of the innovative mortar has been designed by using the Design of Experiments (DoE) techniques, which enables the designers to determine simultaneously the individual and interactive effects of many factors that could affect the output results in any design. DOE also provides a full insight of interaction between design elements; therefore, it helps turn any standard design into a robust one. The factors considered in the present study (and the related variability ranges) are:

- Cement (variability 25 – 35%).
- Sand (variability depending on the other factors).
- Limestone. (constant at 5%).
- Other additives (details of the individual mixtures will be divulgated at the end of the research project).

A total of 25 different mixtures have been analysed. Experimental tests includes compression tests (6 specimens for each mixtures) on small cubes (4x4x4 cm), three point bending tests (3 specimens for each mixture) on small beams (4x4x16 cm), bending tests on thin (3mm thickness) specimens and sliding-shear tests on small brick-mortar assemblies. Photos of the different test set up are displayed in Figure 4.7. The

following quantities have been considered to obtain the "best candidate" of the optimum mixture:

- Compression strength
- Tensile strength
- Sliding shear strength
- Ductility ratio (calculated by evaluating the equivalent bi-linear response from the experimental tests on the thin specimens)

A detailed description of the results of the experimental tests is beyond the scope of the present thesis and will be presented at the end of the research program.

The most promising prototype formulations exhibit the following (average) properties:

- Compression strength around 7-8 MPa
- Tensile strength around 3-4 MPa
- Shear strength around 1.2-1.7 Mpa
- Ductility ratios around 1.5-2.5

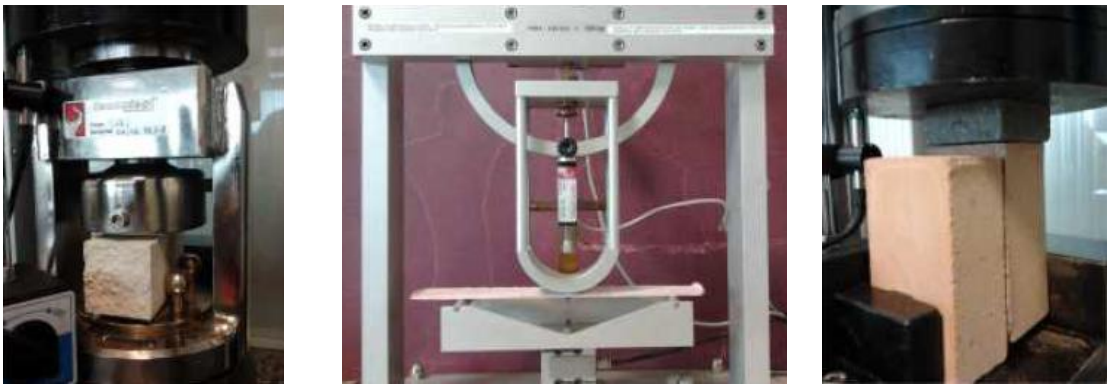

(a) (b) (c)

Figure 4.7: tests set up: (a) compression test (b) bending test on thin specimens; (c) sliding shear test.

Figure 4.8 displays the force-deformation response of selected specimens as obtained from the bending tests on the thin specimens. In general an increase of ductility is coincident with a decrease in strength, as showed by the graph of Figure 4.8.

The results obtained from the first experimental tests seems to be promising and in line with the objectives of the project. Actually a second experimental campaign is under development in order to further refine the preliminary formulation.

4.4. CONCLUSIONS

In this chapter the first results of the research project "Italici" focused on the development of innovative (seismic resistant) infills have been presented . The research project involves the practical contributions of various partners from the industry world and the scientific contribution of the Department of Civil Engineer of the University of Bologna. In this context the main contribution of the Department of Civil Engineer of the University of Bologna is to provide the necessary scientific knowledge to direct and coordinate the development of the innovative materials (clay bricks with alumina-based nanoparticles and additivated mortar) as well as to carry out part of the experimental tests.

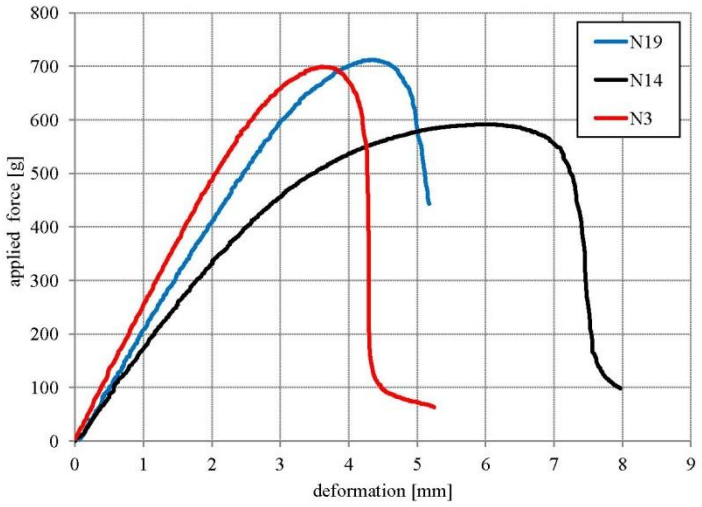

Figure 4.8: force-displacement response of selected specimens as obtained from the bending tests on the thin specimens.

The first step was related to the identification of seismic performances for the innovative infills. A good target for the infill shear strength has been identified around 1.0 MPa, while a good ductility could be around 2.0. Then a large experimental campaign has been scheduled. At the present moment, only the first part of the experimental campaign has been completed. The main results can be summarized as follows:

- The presence of the sawdust in the mixture of the clay bricks (necessary to satisfy the thermal requirements) provides a consistent reduction of the mechanical properties (-30% compressive strength, -40% tensile strength). However, due to the high intrinsic mechanical properties of the base mixture (around 60MPa compressive strength and 20 MPa tensile strength), those detrimental effect could not affect (in a significant amount) the seismic response of the masonry assemblies provided that the overall response could be mainly governed by the mortar properties.

- The inclusion of the alumina-based nanoparticles in the mixture of the clay bricks has a limited influence on the main mechanical properties (it seems to slightly increase the tensile strength). Additional tests are necessary to further understand if the addition of alumina-based nanoparticles should be considered in the final mixture of the clay bricks.

- A first attempt for the development of the optimum mixture for the innovative mortar has been conducted using DoE techniques. The results of first tests allowed to identify some promising prototype formulations able to accomplish with the proposed objectives. The obtained shear strength is around 1.2-1.7 Mpa, while the ductility ratios are around 1.5-2.5. Those values could be an indication of the masonry shear strength.

- The results of the next experimental tests which will be carried out on small masonry assemblies and on full scale masonry walls will provide more precise values of the strength and indications of the ultimate drifts to be adopted for the seismic design.

5. The seismic design of the seismic-resistant masonry infill

5.1. INTRODUCTION

The actual Italian building code (NTC 08) does not allow to consider unreinforced masonry infills as primary structural elements, i.e. structural elements designed in order to sustain lateral loads. However their contribution in term of mass has to be considered. They are treated as secondary structural elements, i.e. their stiffness and strength is ignored in the seismic analysis of the structure, whilst they have to be designed in order to have deformation capacities compatible with the seismic demand. In order to accomplish this requirement the primary structural elements (typically columns, beams and RC walls) are designed in order to satisfy precise interstorey drift limits (in the case of RC frame with unreinforced masonry infill the prescribed drift limit is equal to 0.5% of the story height). In light of above, no specific analytical models are recommended for unreinforced masonry infills and strength and deformation capacity are not provided. The effects of the seismic loads on the infills can be evaluated by applying a lateral force equal to the weight times the spectral acceleration which accounts, in a simplified way, for the dynamic amplification along the building height. A limited ductility can be accounted through a behavior factor q_a which is set equal to 2.0. The horizontal action applied at the top of the wall is used to check the out-of-plane capacity.

Nonetheless, the detrimental effects due to the presence of the infills have to be considered. In the case of an in-plan asymmetric distribution of infill the accidental eccentricity has to be doubled. In the case of irregular distribution infills in elevation, the design actions for the vertical structural elements (typically columns and walls) in a weak story have to be amplified by a factor equal to 1.4.

In this chapter, which concludes the part A of the thesis, considerations for the seismic design of the innovative unreinforced masonry infills are provided, based on the first results presented in the previous chapter.

5.2. ON THE SEISMIC DESIGN OF THE INNOVATIVE MASONRY INFILL

In this section simple design consideration for the seismic design of the innovative unreinforced masonry infill presented in the previous are provided. Clearly, as stated in chapter 4, the study of the innovative infill (and specifically its mechanical characterization) is still in progress. Nonetheless, it seems important to conclude the first part of the thesis with some (although preliminary) design recommendations.

5.2.1. On the modelling of the innovative masonry infills

In chapter 3 a detailed review of the modelling approaches which are actually available for the seismic analyses of frame structures with masonry infills has been provided. It has been noted that the two fundamental approaches (i.e. macromodels based on equivalent struts approaches, or micromodels based on the continuum mechanics approach) are characterized by a substantially different level of sophistication and therefore appears suitable for different uses. Micromodels may allow for a detailed representation of the stress-strain response of the infills, and can represent the complex damage mechanisms and interactions between walls and surrounding frames. On the other hand, their correct use requires notable expertise of the user and computational effort. Moreover only few commercial software actually includes modulus which are specifically dedicated to masonry infills, and therefore the use of micromodels appears restricted mainly to research purposes. The use of simple equivalent nonlinear strut models may allow to reasonably represent the stiffness, strength and ultimate deformation of unreinforced masonry infills and therefore its use may appear actually more appropriate for professional engineers.

In chapter 3 the use of the equivalent nolinear strut model together with an appropriate model to account for the shear failure of reinforced concrete columns, has been

satisfactory applied to reproduce the observed mechanisms of collapse of a real RC frame building which collapsed after the 2009 l'Aquila Earthquake. The analyses showed that the capacity models suggested by ASCE41-06 for the evaluation of the strength and ultimate deformation of existing unreinforced masonry infills seems to provide reasonable results.

From all the above considerations it appears that, at the moment, the nonlinear equivalent strut model could be suggested for design purposes. The equivalent strut is characterized by the same thickness of the infill, t_{inf}, and by a width a equal to (Maistone 1971):

$$\begin{aligned} a &= 0.175\left(\lambda_h h_{col}\right)^{-0.4} D_{\inf} \qquad \text{for} \quad 4 \le \lambda_h \le 5 \\ a &= 0.16\left(\lambda_h h_{col}\right)^{-0.3} D_{\inf} \qquad \text{for} \quad \lambda_h > 5 \\ \lambda_h &= \left[\frac{E_m t_{\inf} \sin 2\theta}{4 E_c I_{col} h_{\inf}}\right]^{0.25} \end{aligned} \qquad \textbf{(5.1)}$$

The elastic modulus of the equivalent strut E_{strut} can be assumed equal to $3E_m$ with E_m the masonry elastic modulus.

5.1.1. The strength of the innovative infill

Based on the results of the first experimental tests the expected masonry shear strength f_v can be reasonably estimated around 1.0 MPa. By assuming a sliding shear mechanism of failure the infill shear strength can be eastimated with the following formula:

$$V_{\inf} = A_n f_v \qquad \textbf{(5.2)}$$

Where A_n is the net area of the infill cross section.

5.3. CONCLUSIONS

In the present chapter code-like design recommendations for the seismic design of the innovative infills studied in the previous chapter are provided. They can be summarized as follows:

- The use of the equivalent nonlinear strut model appears suitable for the design of the innovative infills.
- The strut width can be evaluated according to the well-known Mainstone approach. A strut elastic modulus around 3 times the masonry elastic modulus is suggested.
- The expected infill strength can be evaluated assuming a sliding shear mechanism of failure and a shear stress of 1 MPa (as the result of the first experimental tests).
- Estimations of the ultimate drifts could be obtained from the next experimental tests on the full-scale infill walls.

PART B: Reinforced Concrete Sandwich Panels

Part B is focused on a specific reinforced concrete sandwich panel system and is composed of four chapters (from chapter 6 to chapter 9). Its main objective is to assess the seismic performances of a specific reinforced concrete sandwich squat panel system with the purpose of introducing design procedure for building structures composed of reinforced concrete sandwich squat walls.

6. The behavior of squat reinforced concrete sandwich wall structures: experimental tests

6.1. INTRODUCTION

The seismic behavior of slender RC shear walls has been the objective of extensive researches since the 1960s. Early studies by Beck 1962 and Rosman 1968 identified the fundamental features of the behavior of RC shear walls and coupled walls and provided simplified analysis methods. Their works prepared the ground for all the further studies. Paulay and Priestely in their book (Paulay and Priestely 1992) dedicated a chapter to the design of RC slender walls. The chapter collects the fundamental results of previous studies and provides detailed design specifications for the design of ductile slender shear walls and coupled walls.

Less research effort has been devoted to the study of the seismic behavior of squat wall, whose response under lateral loads is characterised by larger uncertainty due to the complex interaction between shear and flexural behavior as the result of their geometrical configuration (small aspect ratios). Experimental tests of squat shear walls conducted by Hidalgo *et al.* 2002 indicated that the aspect ratio significantly affects the deformation capacity and the strength deterioration due to loading reversal after the peak strength is reached. Comparison of wall response to code-based predictive equations showed that these equations overpredict the peak shear strength of these squat rectangular walls by factors as large as 2 (Whyte and Stojadinovic 2013), thus indicating the need of improved code provisions for the design of squat RC walls.

Indications on the fundamental mechanisms of shear resistance in squat wall are given by Paulay and Priestely 1992. First of all, because of relative dimensions, the mechanisms of shear resistance appropriate to RC beams and columns (and often extended to slender shear walls) are not generally applicable to squat RC walls. In the

cases of insufficient horizontal reinforcement a corner-to-corner tension failure plane may develop. A tie beam at the top of the wall may prevent from this mechanism of failure. If adequate horizontal reinforcement has been provided, average shear stress may become large and lead to concrete crushing under diagonal compression, before the wall reach its flexural strength. This mechanism is quite common in walls with flanged sections which may have large flexural strength. Diagonal compression failure is characterized by a significant loss of strength and should be avoided, by limiting the values of the maximum shear stress at the flexural strength. In the case of maximum shear stress are limited and an adequate horizontal reinforcement is provided, a mechanism of sliding shear at the base due to progressive yielding of the vertical reinforcement at the base, may develop. Such sliding displacements are responsible of a significant stiffness reduction. Tests of squat walls showed that excessive sliding shear has severe detrimental effects (strength and stiffness deterioration) and the use of diagonal reinforcement crossing the sliding plane may consistently reduce the phenomenon. Also the use of boundary elements may significantly increase the performance of RC squat walls as demonstrated by the experimental investigation conducted by Lowes *et al.* 2011.

Precast sandwich panels (PSPs) are composed of two concrete wythes separated by a layer of insulation. Once in place, the sandwich wall panels provide the dual function of load carrying capacity and insulation. PSPs may be used solely for cladding (i.e. non-structural components), or they may act as bearing walls, or shear walls. PSPs are commonly used as exterior and interior walls for many types of structures, from low rise residential buildings (see http://www.nidyon.net) to high rise complex buildings (see http://www.highconcrete.com). These panels may be connected to any type of structural frame, e.g., structural steel, reinforced concrete, pre-engineered metal and precast/prestressed concrete (PCI, 1997).

The panels are typically precast at a manufacturing plant, trucked to the construction site and erected by cranes. Sometimes only the formworks are precast at manufacturing plants, and the structural concrete is cast in situ after that formworks and additional reinforcements are positioned. Panels generally span vertically between foundations

and floors or roofs to provide the permanent wall system, but may also span horizontally between columns. Regarding to design, detailing, manufacturing, handling, shipping and erection the sandwich panels are similar to other precast concrete members; nonetheless, because of the presence of an intermediate layer of insulation, they do exhibit some features and distinctive behaviors (PCI, 1997).

The interest in sandwich panels has increased in the past few years because they are characterized by desirable characteristics of durability, economical convenience, fire resistance, vertical and horizontal load bearing capacity as well as excellent insulation properties providing superior energy performance as compared to many other walls (Losch 2005). However, a limited number of research works are available in the scientific literature partially due to the need of full scale testing (characterized by high costs) and partially due to the hesitancy of the construction firms to shear their know-how with the competitors. Holmberg and Pelm 1986 investigated the load bearing capacity of sandwich panel structure under static loadings. Einea *et al.* 1994 proposed the use of plastic materials as shear connector to increasing the insulation of properties of the panels. The out-of-plane response (out of plane shear and flexure) of sandwich panels has been investigated by Kabir 2005 through of static tests and numerical investigations. Results of an experimental investigation on the ultimate strength behavior of precast concrete sandwich panels with steel truss shear connectors are reported in Benayoune *et al*. 2006, 2007, 2008. Recently, Rezaifar *et al*. 2008 investigated the dynamic response of a full-scale single storey building composed of precast sandwich panels through shaking-table tests.

A large research program aimed at studying the structural behavior of building structures composed of precast sandwich panels produced by an Italian firm (Nydion Costruzioni) has been developed at the University of Bologna through a number of experimental tests including:

- Materials tests.
- Uniaxial compression tests (with and without eccentricity).
- Diagonal compression tests.
- Slip tests (in order to evaluate the capacity of the transversal connections).

- Out of plane tests.
- Connections tests (orthogonal walls and foundations).
- In plane reversed cyclic tests on single panels (with and without opening).
- In plane reversed cyclic test on a full scale H shaped structure.
- Dynamic tests with vibrodina.
- Shacking table tests on a full scale three stories building.

The large amount of acquired data allowed to appropriately characterize the in-plane and out-of plane behavior of the structural system aimed at providing engineering design procedures consistent with the current code provisions (EC2 and EC8). A detailed description of all the experimental results may be found in a Ph.D thesis (Ricci 2012), while a summary of the results of the in plane reversed cyclic tests on single panels (with and without opening) is available in Ricci *et al.* 2013.

A full description of the experimental tests is beyond the scope of the present work. Therefore, only the information necessary for a better understanding of the interpretation of the test results (representing the object of the next two chapters) are recalled.

6.2. SUMMARY OF THE EXPERIMENTAL TESTS

Intending to assess the seismic performance of PSPs wall assemblies, the University of Bologna and the EUCENTRE laboratory of Pavia (Italy) jointly carried out an experimental campaign. A total of six full-scale tests were performed: the first five on planar wall specimens (namely PW1, PW2, PW3, PW4 and PW5); the last one on a two-story H-shaped structure (namely HSW). Each specimen underwent cyclic horizontal displacements with load reversals and a constant vertical load. In order to investigate their influence, different vertical loads were applied to different specimens. This paragraph contains a brief summary of the experimental results. Additional details are available in Ricci *et al.* 2013.

6.2.1. Geometrical and mechanical properties of the specimens

The following specimens were tested: three planar walls with no openings (PW1, PW2 and PW3, also referred to as type A), two planar walls with a central square opening (PW4 and PW5, also referred to as type B), a two story H-shaped wall (HSW). The first five specimens are composed by a single square PSP each while the H-shaped wall is composed by six square PSPs and two 0.2 m thick reinforced concrete slabs. All the PSP have side length 3.0 m and the openings have side length 1.0 m.

The basic PSP panel is 18 cm thick with a central 10 cm expanded polystyrene corrugated layer and two external 4 cm RC layers. The representative drawings of each wall assembly are given in Figure 6.1 and Figure 6.2. The basic reinforcement is a ϕ 2.5 mm smooth mesh grid spaced 50 mm resulting in a reinforcement ratio equal to 0.245%. Additional horizontal and vertical bars (ϕ 12 mm) were located at the edges and around the openings of the planar walls in order to prevent local failures. The connection between the two RC layers is realized through ϕ 3 mm transversal connectors spaced 30 cm. The connections between the orthogonal walls of the HSW specimen were realized with 2 ϕ 12 mm vertical bars and ϕ 6mm horizontal bars spaced 30 cm. The connections between the walls and the foundations are realized through ϕ 8 mm anchor rods. A summary of the main characteristics of each specimen is presented in

.

Table 6.1: Summary of the specimen properties

ID	Wall type	Dimensions [m] x [m]	Opening dimensions [m] x [m]	Self-weight [kN]	Vertical load [kN]	Vertical load ratio
PW1	plane	3.0 x 3.0	-	19.9	50	0.87%
PW2	plane	3.0 x 3.0	-	19.9	100	1.73%
PW3	plane	3.0 x 3.0	-	19.9	250	4.35%
PW4	plane	3.0 x 3.0	1.0 x 1.0	17.9	50	0.87%
PW5	plane	3.0 x 3.0	1.0 x 1.0	17.9	100	1.73%
HSW	H-shaped	3.0 x 6.0	-	93.5	200	1.60%

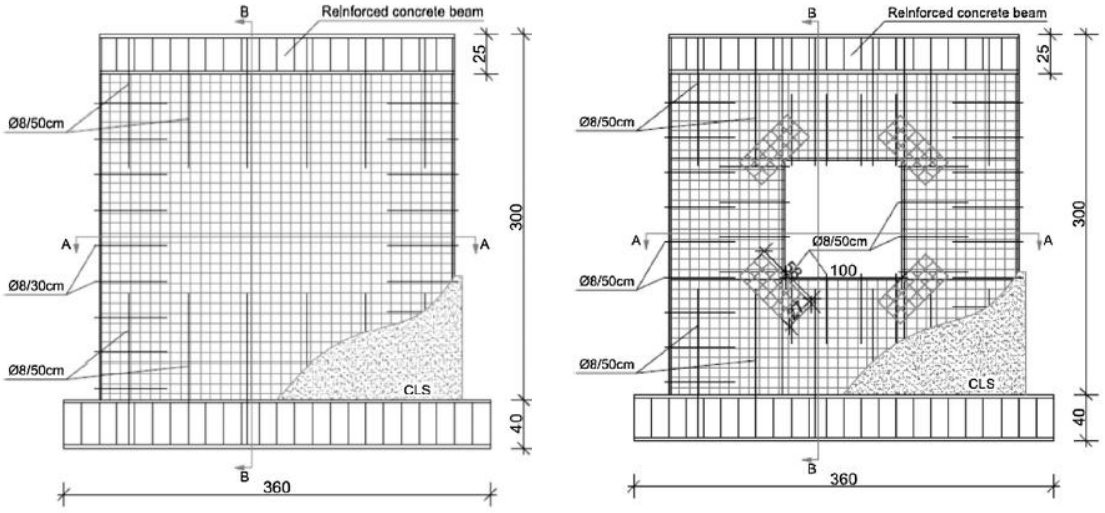

(a) (b)

Figure 6.1: (a) Reinforcement layout for the full planar wall; (b) Reinforcement layout for the planar wall with the central opening

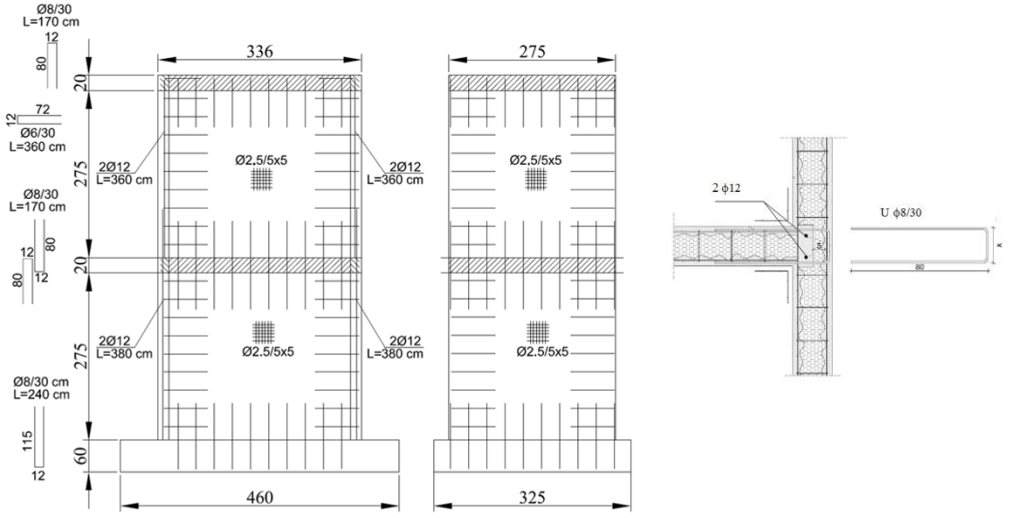

Figure 6.2: Reinforcement layout for the HSW specimen.

Nominal concrete strength was 30 MPa, while the steel yield strength was 450 MPa. The vertical load ratio is defined as $N/(A_c f_c)$, where N is the applied vertical load, A_c is the concrete gross section, f_c is the concrete compressive strength.

6.2.2. Test set-up and instrumentation

The specimens were fixed at the base in a cantilever configuration with imposed horizontal displacements and constant vertical loads. For the PW specimens, the lateral displacement was imposed to the top loading beam and the drift ratio varied from 0.1% to 1.5% during the loading cycles. For the HSW specimens, the horizontal action was applied to both slabs by two actuators that kept a constant ratio between upper and lower applied force of 2/1 while the displacement was controlled at the top slab. The drift targets of the displacement cycles were 0.1%, 0.2%, 0.4% and 0.8%. After the last one two further low cycles at 0.1% drift were applied followed by a final cycle up to 1.0% drift to evaluate residual stiffness and strength. For all the specimens the vertical forces and the corresponding vertical load ratios are reported in

. Figure 6.3 schematically shows the typical instrumentation for specimen type A and B, while Figure 6.4 shows the instrumentation for specimen HSW. The instrumentations allowed to obtain measurements of (a) in-plane and out-of-plane absolute displacements; (b) deformations along horizontal, vertical and diagonal direction; (c) slip between the walls and the foundations.

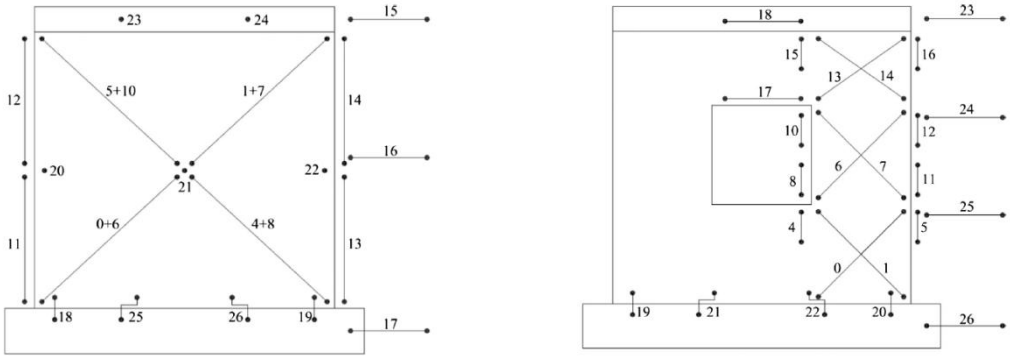

(a) (b)

Figure 6.3: (a) Typical instrumentation for Wall type A; (b) Typical instrumentation for Wall type B.

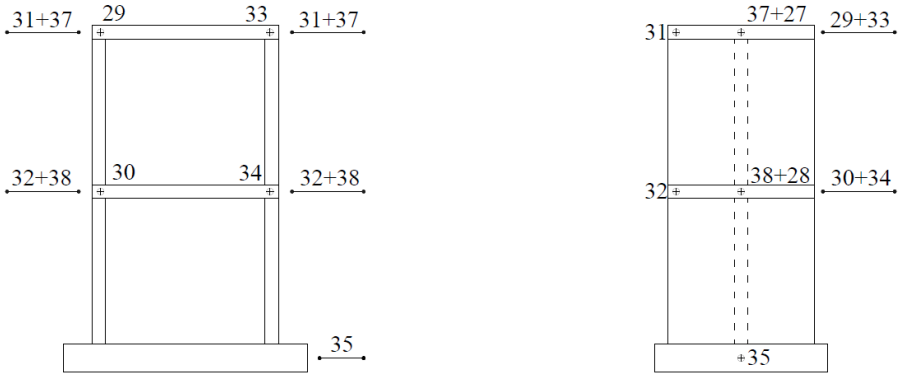

(a) (b)

Figure 6.4: Instrumentation for HSW specimen: (a) web plane; (b) flange plane.

6.2.3. Summary of the experimental results

The global experimental response in terms of base shear vs. story drift (roof drift in the case of HSW specimen) of all specimens is represented in Figure 6.5.

The following observations refer to the planar walls and are extracted from the work of Ricci *et al.* 2013:

- the initial stiffness is about 40 kN/mm for all the specimens (corresponding to roughly 10% of the gross section lateral stiffness);
- the lateral strength per unitary wall length is over 100 kN/m and it is attained for drift ratios in the range 0.4-0.5%. The strength depends on the vertical load ratio;
- increasing the ductility demand, the strength does not significantly decay until a drift ratio of 1.0%. After such value the strength degradation of the specimens PW2 and PW3 is more important than that of the specimens PW1, PW4 and PW5;
- the hysteretic cycles are quite pinched due to the sliding between the wall and foundation;
- the global load-displacement responses of the planar walls with and without opening are similar thanks to the additional reinforcements around the openings. Nonetheless the specimens suffered different structural damage.

The state of damage observed for the planar walls can be summarized as follows:

- flexural horizontal cracks appear at the base of the specimens for a drift ratio of about 0.1%;
- shear diagonal cracks progress on the web for drift ratios around 0.4%;
- vertical cracks, long 10 cm and spaced about 50 cm, start from the base of the wall for drift ratios in the range 0.6%-0.7%. They indicate the deterioration of bond between the anchor bars at the base and the concrete;
- concrete cover flacks from the surface and crushes at the bottom corners starting at about 0.8% drift;
- after the debonding of the anchor bars a significant base sliding takes place while the crack pattern of the rest of the wall do not significantly change;
- as expected, in wall type B the shear cracks are concentred around the central opening. Nonetheless, due to the presence of adequate additional reinforcement around the openings, the progression of cracks for wall type A and B is quite similar.

The following observations come from the HSW specimen:

- the peak lateral strength is approximately equal to 500 kN;
- a strength drop happens at about 0.5% drift;
- a residual strength of about 80% of the peak strength is maintained up to 1.0% drift;
- the global load-displacement response of the HSW specimen is less pinched than that of the planar walls.

The damage state of the HSW can be summarized as follows:

- diagonal shear cracks on the web and horizontal flexural cracks at the bottom of the flanges appear at about 0.1% drift and progressively widen;
- the spalling of the concrete cover happens at about 0.8 % on the corner between web and flanges;
- no significant slip between the wall and the foundation takes place. The reasons are the less spacing of the anchor rods (30 cm for HSW versus 50 cm for the PW) and the additional strength offered by the flanges.

Figure 6.6 and Figure 6.7 provide the crack patterns of some PW specimen and of the HSW specimen, respectively.

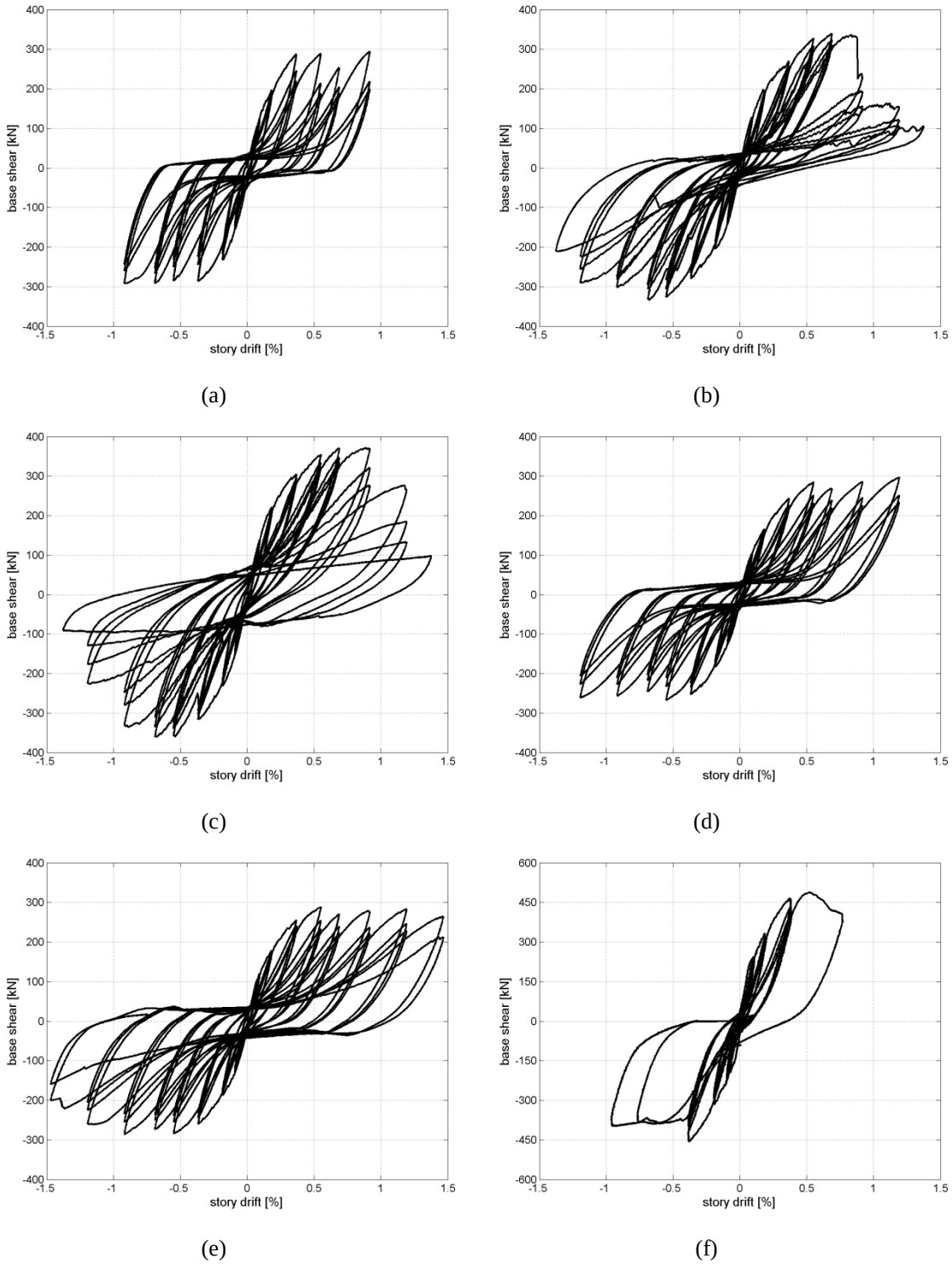

Figure 6.5: Base shear vs. story drift experimental response: (a) specimen PW1; (b) specimen PW2; (c) specimen PW3; (d) specimen PW4; (e) specimen PW5; (f) specimen HSW.

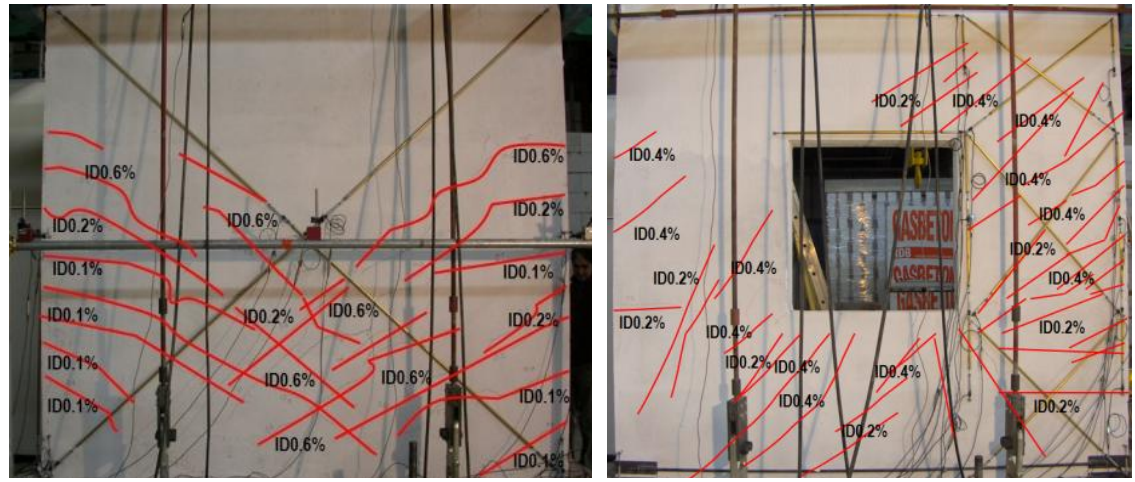

(a) (b)

(c) (d)

Figure 6.6: Cracking patterns at the end of the test: (a) specimen PW1; (b) specimen PW4; (c) concrete spalling at the base, for specimen PW3; (d) concrete corner crushing for specimen PW2.

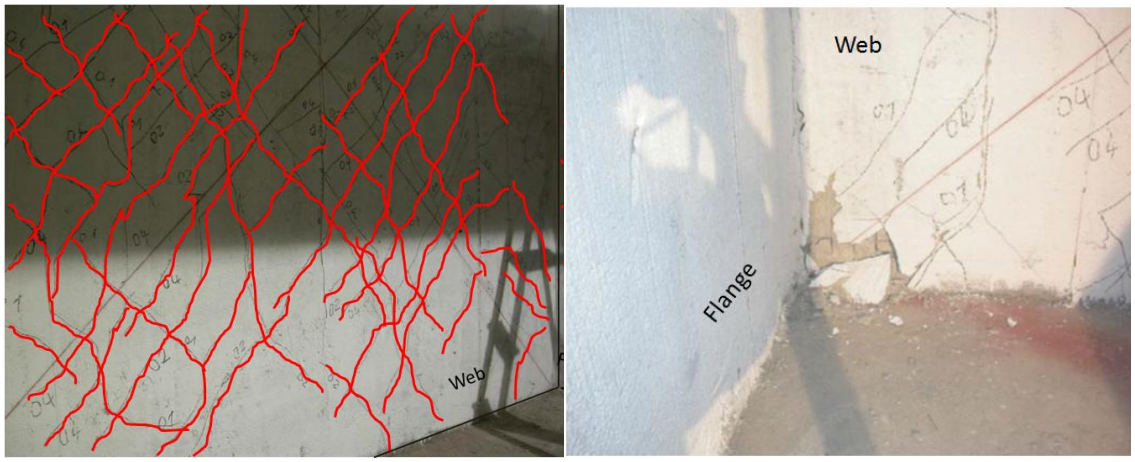

(a) (b)

Figure 6.7: (a) Cracking pattern at the end of the test for HSW specimen; (b) detail of concrete spalling at the corner of the web panel for HSW specimen.

6.3. CONCLUSIONS

In this chapter the results of experimental cyclic tests conducted on RC sandwich planar walls and on an H-shaped wall have been briefly summarized with the purpose of provide information for their interpretation. It has been showed that the tested walls are characterized by a ductile seismic behavior which can be compared to that of conventional RC shear wall with similar geometry and reinforcements, and designed according to current seismic design specifications (Hidalgo et al. 2002). The interested reader may find details in Ricci *et al.* 2013.

7. Modelling reinforced concrete sandwich walls according to compression field theories

7.1. INTRODUCTION

The two current most noteworthy theories for conventional reinforced concrete members subjected to shear and torsion (i.e. the Modified Compression field Theory, MCFT, proposed by Vecchio and Collins at the University of Toronto (Vecchio and Collins 1986) and the rotating-Angle Softened-Truss Model, RA-STM, developed by Hsu and his co-workers at the University of Huston, (Belarbi and Hsu 1994)) are both grounded on the continuum mechanics approach. The external forces are in equilibrium with the internal forces; average strains are in geometric compatibility with the displacements and average (or "smeared") stresses are related to average (or "smeared") strains via appropriate constitutive equations. Refinements to the MCFT have been recently proposed by Gil-Martin *et al.* 2009 leading to the so-called Refined Compression Field Theory, RCFT. These refinements deals with an introduction of a smeared constitutive model for the reinforcement embedded in the concrete, which account for the tension stiffening in the concrete. Those refinements allows to overcame the local checks of the shear stresses at cracks locations which are required by the MCFT and at the same time allows to more accurately reproduce the experimental response of conventional RC panels, especially in the regions close to the peak strength (Gil-Martin *et al.* 2009). Nonetheless, the calibration of additional parameters is necessary.

In this chapter, the fundamentals of the conventional shear theories for RC members (MCFT and RA-STM) are briefly recalled. The theories are applied in order to predict the force-deformation response of the RC sandwich panels described in the previous chapter. The predictions of the theories are compared with the envelope response as obtained from the pseudo-static tests. Then, the RCFT is used to obtain the force-deformation response of the panel. Appropriate constitutive equations based on the

experimental results are introduced within the RCFT approach. The results here presented are largely extracted from the work of Palermo *et al.* 2012.

7.2. SHEAR THEORIES FOR REINFORCED CONCRETE ELEMENTS: THE CONTINUUM MECHANIC APPROACH

The actual fundamental shear theories for RC members are based on a continuum mechanic approach which, despite the first shear theories based on equilibrium considerations only (i.e. truss models first introduced by Ritter 1989 and Morsch 1922), make use of compatibility, equilibrium and materials constitutive relationships, in order to obtain the complete force-displacement response. The fundamental assumptions of the continuum mechanic approach are (Vecchio and Collins 1986):

- Stresses and strains can be considered in terms of average values estimated over a length large enough to include several cracks;
- The angle of inclination of the principal stresses coincides with the angle of inclination of the principal strains;
- Perfect bond between concrete and steel reinforcement is assumed.

Under these assumptions the following set of equations can be formulated:

- Compatibility equations, obtained from Mohr's circle of strain (see Figure 7.1):

$$\begin{aligned} \varepsilon_x &= -\varepsilon_2 \cos^2\theta + \varepsilon_1 \sin^2\theta \\ \varepsilon_v &= -\varepsilon_2 \sin^2\theta + \varepsilon_1 \cos^2\theta \\ \gamma_{xv} &= 2(\varepsilon_x - \varepsilon_2)/\tan\theta \end{aligned} \qquad \textbf{(7.1 a,b,c)}$$

x and *v* indicate the vertical and horizontal directions, respectively. The criterion coincides with the typically adopted sign criteria (Collins and Mitchell 1991); subscripts 1 and 2 indicate the directions of the principal tensile and compressive stresses and strains in the concrete, respectively; θ indicates the inclination of the compressive concrete strut with respect to the *x* direction. ε_x, ε_v, ε_1, ε_2, are the axial strains in the *x*, *v*, 1 and 2 direction, respectively, while γ_{xv} is the shear strain.

From Eq. (7.1 a,b,c) the "crack" angle θ can be derived as:

$$\tan^2\theta = \frac{\varepsilon_x - \varepsilon_2}{\varepsilon_v - \varepsilon_2} \qquad \textbf{(7.2)}$$

- Equilibrium equations, obtained from equilibrium conditions in Figure 7.2, are:

$$\begin{aligned} V &= (f_1 + f_2)\,Sin\theta\;Cos\theta\;t\,L \\ n_v\,A_{sv}\,f_{sv} &= (f_2\,Sin^2\theta - f_1\,Cos^2\theta)\,t\,H \\ N &= (f_2 Cos^2\theta - f_1 Sin^2\theta)\,t\,L - n_x\,A_{sx}\,f_{sx} \end{aligned} \qquad \textbf{(7.3)}$$

V and N are the external applied shear and axial load as shown in Figure 7.2; f_1 and f_2 are the internal tensile and compressive stresses on concrete, respectively; f_{sx} and f_{sv} are the tensile stresses in the reinforcement; L, H, t are the length, height and thickness of the tested panels, respectively; A_{sx} and A_{sv} are the area of the steel bars while n_x and n_v indicate the total number of steel bars along the x and v direction, respectively.

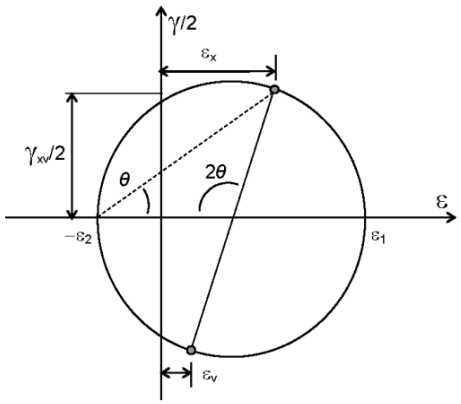

Figure 7.1: Mohr's circle of strains.

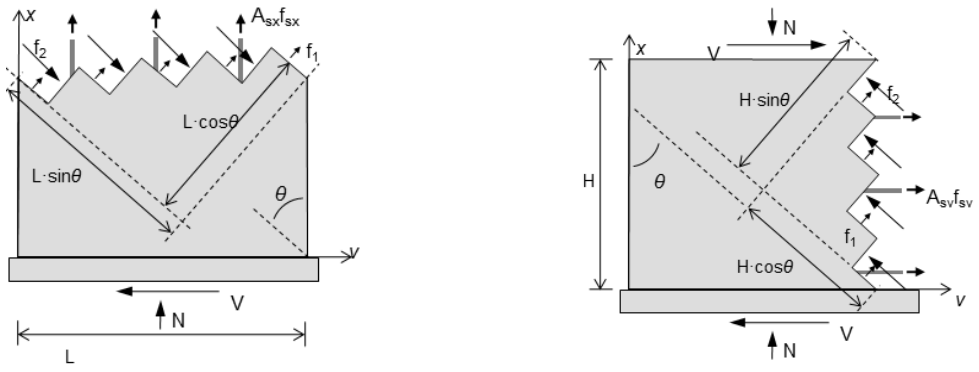

(a) (b)

Figure 7.2: Equilibrium for a section of panel: (a) Free body diagram 1; (b) Free body diagram 2.

The fundamental assumptions adopted by the MCFT and RA-STM theories are the same. The discrepancies observed in the predictions to the test responses are due to the different constitutive laws used to characterize the stress-strain materials behavior. The constitutive laws for softened concrete in compression and concrete in tension (i.e. tension stiffening) for MCFT and RA-STM can be found in (ASCE-ACI 1998). In both theories, laws were obtained from experimental tests on reinforced concrete panels subjected to in-plane shear. The main difference between the two aforementioned approaches, that yields different responses, lies on the constitutive law adopted for the reinforcement bars: while MCFT assumes the constitutive law of a bare bar, RA-STM theory introduces an average stress-strain curve for the mild steel bars embedded in concrete.

7.3. MCFT AND RA-STM PREDICTIONS OF THE PANELS' RESPONSE.

Figures 13a, b and c show the prediction of shear-deformation response of panels PW1, PW2 and PW3 as given by the MCFT and the RA-STM. MCFT predictions were obtained using the software Membrane 2000, RA-STM predictions were obtained by direct implementation of the original formulation (Belarbi and Hsu 1994). It is to be noted that during the tests panels behaves as deep cantilever. Therefore, in order to compute the experimental shear strain, the imposed horizontal displacement has been depurated from the flexural component assuming a cantilever schematization with the inertial properties of the cracked section. From these schematizations, the flexural deformation results to be from 10 to 15% of the total deformation.

Inspection of the graphs clearly shows that, while both theories are able to accurately predict the shear response at high level of drift (i.e. for shear corresponding to an ultimate state), the predictions at lower drifts are much higher than the experimental ones. The reason for this large overestimation lies in the post-cracking concrete contribution due to the tension stiffening, that from test evidence appear to be considerably less than that predicted by tension stiffening models (Bentz 2005).

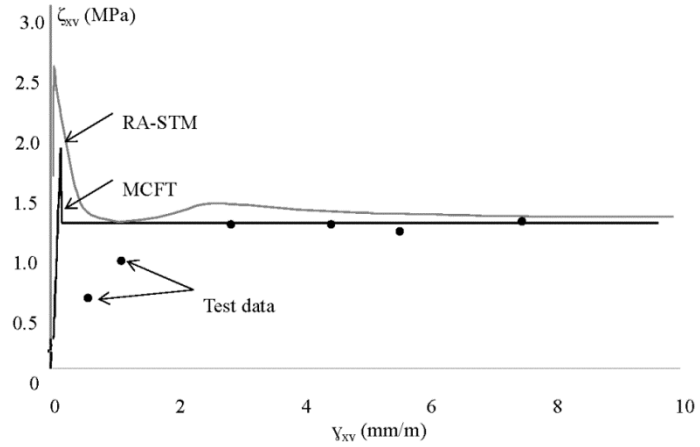

(a)

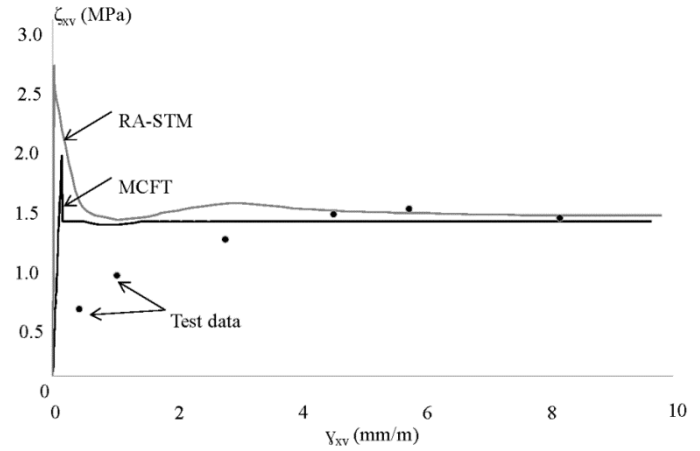

(b)

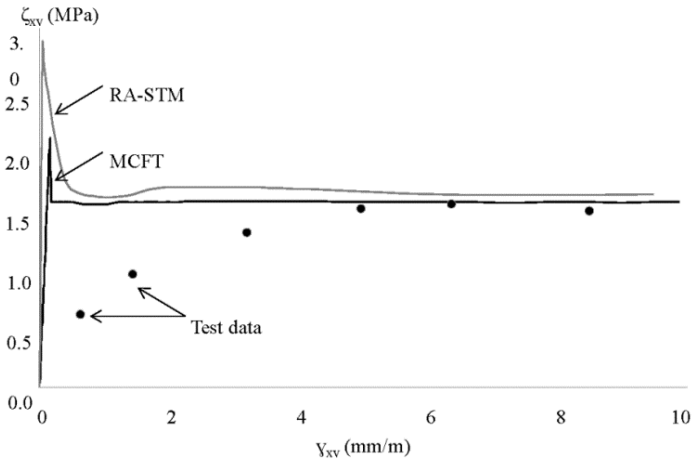

(c)

Figure 7.3: Comparison between the MCFT, RA-STM and test data. (a) test on PW1 (N=50 kN); (b) test on PW2 (N=100 kN); (c) test on PW3 (N=250 kN).

7.4. ADAPTING THE REFINED COMPRESSION FIELD THEORY FOR THIN RC SANDWICH PANELS

The previous section showed that both MCFT and RA-STM are not able to accurately predict the experimental observed shear-deformation response of the tested thin shotcrete panels due to an overestimation of the so-called "concrete contribution" (depending on the tension stiffening model) at low drifts. Over the years many different concrete tension stiffening curves have been proposed (Bentz 2005) in order to account for the average post-cracking concrete tensile strength, physically related to the bond–slip actions that occur along the anchored reinforcement.

Because of the current adopted models for tension stiffening, they are not explicitly formulated in terms of bond characteristics (Martin-Perez and Pantazopoulou 2001) and their predictions are strongly dependent on the specific experimental data used to calibrate the model, that, in turn is strongly affected by the specific characteristics of the specimens (e.g. bar typology -i.e. smooth or deformed, and size-, reinforcement ratio and concrete aggregate size). Figure 7.4 compares some available models for tension stiffening showing relevant post-cracking tensile strength differences. In light of the geometrical and mechanical characteristics of the tested panels, it clearly appears that the values of the parameters influencing the post-cracking concrete stress behavior of the tested panels are quite far from the panels tested so far. More specifically, the main differences showed by the investigated panel are: (i) higher ratio between the panel dimension (3x3 m) and little panel thickness (two layers of 4 cm of concrete), (ii) smaller bar diameter (i.e. 2.5 mm), (iii) smaller reinforcement ratio (i.e. 0.245 %); (iv) use of sprayed concrete with small aggregate size. Moreover, it has been observed from the tests that the applied axial load contributed to a sudden degradation of the concrete strength in tension, in such a way that reminds us of the bursting effect in concrete under punctual loading.

For all these reasons, the adoption of a proper calibrated relationship for concrete in tension appears necessary. Clearly, based on the influence that tension stiffening provides to the reinforced steel model (Gil-Martin *et al.* 2009), a new constitutive equation for the steel bars embedded in concrete is also required.

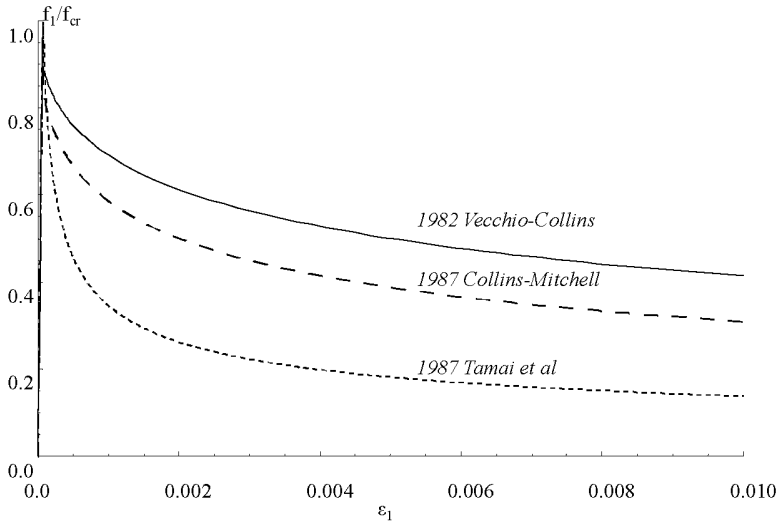

Figure 7.4: Examples of tension-stiffening equations available in the scientific literature.

7.4.1. Proposed tension stiffening model for shotcrete and wire mesh embedded in the shotcrete

The assumed stress-strain relationship of concrete in compression is the one proposed by Collins and Mitchell 1991:

$$f_2(\varepsilon_2) = f_{2\max}\left[2\left(\frac{\varepsilon_2}{\varepsilon_{c1}}\right)-\left(\frac{\varepsilon_2}{\varepsilon_{c1}}\right)^2\right] \qquad \textbf{(7.4)}$$

$$where\ f_{2\max} = \frac{f_{cm}}{0.8+170\varepsilon_1} \le f_{cm}$$

ε_{c1} is the strain at the maximum value of stress, given by EC2 and f_{cm} is the mean value of the concrete strength.

An average tension stiffening model, based on the conceptual approach by Bentz 2005 and calibrated in order to fit the experimental data, is here proposed:

$$f_1(\varepsilon_1) = \begin{cases} E_c\varepsilon_1 & for \quad \varepsilon_1 \le \varepsilon_{cr} \\ \dfrac{\alpha\, f_{cr}}{1+\sqrt{\dfrac{M\,\varepsilon_1}{20}}} & for \quad \varepsilon_1 > \varepsilon_{cr} \end{cases} \qquad \textbf{(7.5)}$$

Where $M = \dfrac{A_{c,ef}}{\sum \phi\pi}$ is a parameter depending on the bar diameter ϕ.

f_{cr} is the mean concrete tensile strength estimated according to Eurocode 2 ($f_{cr} = 0.3 f_{ck}^{2/3}$, where f_{ck} is the characteristic strength of concrete); ε_{cr} is the concrete strain at f_{cr}; M is the bond parameter in mm, introduced by Bentz 2005, which accounts for the area of concrete effectively contributing to tension stiffening. $A_{c,ef}$ is area of concrete effectively bonded to the bar (i.e. the rectangular area of concrete tributary to the bar extending over a distance of 7.5 bar diameters transversely to the bar), and ϕ is the diameter of the bar in concrete stiffened area. The α coefficient is responsible for the sudden drop of the tension stiffening after cracking. The α coefficient has been obtained through a numerical procedure adjusting (squared least) the tension stiffening model (Eq. (7.5)) in order to fit the envelope response of the experimental data (i.e. the force-deformation shear response, see test data in Figure 6.5). The obtained values of α coefficient as function of the applied axial load N are summarized in Table 7.1. Inspection of Table 7.1 clearly shows that α decreases almost linearly as N increases. For intermediate values of N, linear interpolation can be used.

Table 7.1: Values of α coefficient for the three different applied axial loads.

	N= 50 kN	N= 100 kN	N= 250 kN
α	0.30	0.175	0.00

The constitutive model of the reinforcement proposed by RCFT (Gil-Martin et al. 2009) has been adapted to the new tension stiffening model proposed in this chapter (Eq. (7.5)), leading to the following formulation:

$$f_s(\varepsilon_s) = \begin{cases} E_s \varepsilon_s & for \quad \varepsilon_s \le \varepsilon_{y,av} \\ f_y - \dfrac{\kappa A_{c,ef}}{A_s} \dfrac{\alpha f_{cr}}{1+\sqrt{\dfrac{M \varepsilon_s}{20}}} & for \quad \varepsilon_s > \varepsilon_{y,av} \end{cases} \qquad \textbf{(7.6)}$$

f_s and ε_s indicates the average stress and strain in the reinforcement with s equal to x for longitudinal (i.e. vertical) bars and equal to v for transversal (i.e. horizontal) bars. $\varepsilon_{y,av}$ is the apparent yield strain, i.e. the average strain when yielding occurs at a crack location; $\varepsilon_{y,av}$ is calculated imposing the equilibrium between a cracked section and the average section between two consecutive cracked sections and the requirement that the

strain of the reinforcement at the crack location is equal to the steel strain at yielding ($\varepsilon_y = f_y / E_s$):

$$f_y A_s = E_s \varepsilon_{y,av} A_s + \kappa A_{c,ef} f_1(\varepsilon_{y,av}) \rightarrow \quad \varepsilon_{y,av} = \varepsilon_y - \frac{k A_{c,ef}}{A_s E_s} f_1(\varepsilon_{y,av}) \qquad \textbf{(7.7)}$$

where *k* was originally introduced in Gil-Martin et al. 2009 to account for the change of the area of concrete participating in tension stiffening, $A_{c,ef}$ (Bentz et al. 2005). In previous studies, the area $A_{c,ef}$ of concrete contributing to tension stiffening has been assumed to be constant (Bentz 2005), being $A_{c,ef}$ the rectangular area of concrete tributary to the bar extending over a distance of 7.5 bar diameters transversely to the bar –value that is insufficient for the studied panels-; however, this area decreases as long as crack spacing decreases or the tensile strain increases. Further investigations are needed to clarify the relevance of this and other possible explanations. In this paper, *k* has been estimated through a numerical procedure (squared least) in order to fit the "monotonic" curve corresponding to the envelope of the cyclic behavior of the specimens. The obtained values of *k* associated with the maximum shear strength as a function of the applied axial loads *N* has been summarized in Table 7.2. It clearly appears that *k* strongly decreases as *N* increases.

Table 7.2: Values of k coefficient for the three different applied axial loads.

	N= 50 kN	N= 100 kN	N= 250 kN
k	1.40	0.70	0.00

Figure 7.5 displays the tension stiffening model for concrete and the model of the embedded steel bars proposed for thin low reinforced concrete panels, for the values of α and *k* given in Table 7.1 and Table 7.2, respectively.

As mentioned before, the fitting problem is performed by adjusting α and *k*, computing the shear-deformation response, from Eqs. (7.1 a,b,c) to (7.7), obtaining the curves shown in Figure 7.5. These curves are the solution to the fitting problem (square least) to the test data, once α and κ are adjusted.

7.4.2. The Refined Compression-Field Theory (RCFT) predictions for the tested panel.

As shown earlier, the previous equations were calibrated on the tests results. Figure 7.6 shows the shear stress versus shear strain deformation response of the tested panels obtained from the adjusted RCFT using the above proposed constitutive equations for concrete in tension and for steel bars embedded in concrete (Eqs (7.5) to (7.7)). Only the post-cracking behavior is displayed. Figure 7.6 clearly shows that the proposed RCFT leads to a very accurate fitting of the experimental data and thus it is able to predict the full load-deformation response of the specimens. On the contrary, as shown above, MCFT and RA-STM are only able to predict the ultimate shear strength.

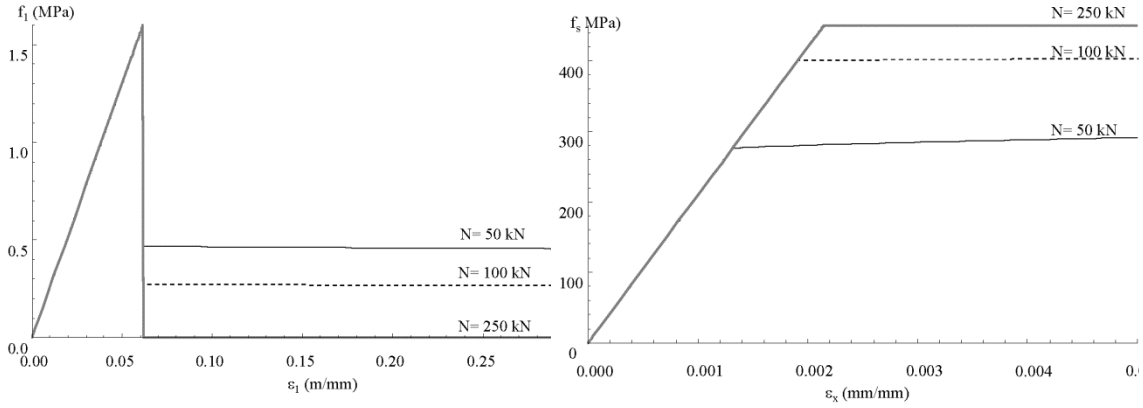

(a) (b)

Figure 7.5: Constitutive equations for the concrete in tension (a) and for the embedded bars (b) for the three different applied axial loads.

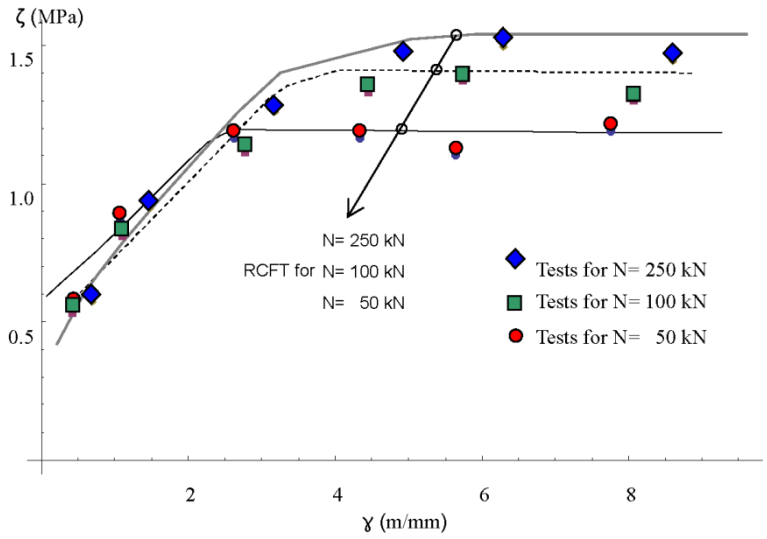

Figure 7.6: The RCFT response compared to the test data.

7.5. DESIGN EQUATION ACCORDING TO THE RCFT

This section provides an application of the RCFT for designing of "Nydion" panels. Let us consider a square full panel having dimensions of 3.00 m x 3.00 m with two layers of 4 cm shotcrete (f_{ck}=26 MPa), reinforced with an electro-welded wire mesh. Continuous lines in Figure 7.7a provide the shear-displacement curves after concrete cracks, obtained via RCFT for an axial load of 100 kN of three panels reinforced with a wire mesh of a different diameter. Figure 7.7b shows the same panels for an axial load of 150kN (values of α and k have been obtained by linear interpolation from Table 7.1 and Table 7.2). Table 7.3 gives the details of the reinforcement layout.

Table 7.3: Reinforcement layout for the examples considered.

ρ_x [%] (*)	ρ_v [%] (*)	Diameter [mm]	mesh size [cm x cm]	f_{yk} [MPa]
0.245	0.245	2.5	5 cm x 5cm	450
0.353	0.353	3	5 cm x 5cm	450
0.628	0.628	4	5 cm x 5cm	450

*ρ_x and ρ_v are the geometrical reinforcement ratio of the vertical and horizontal reinforcement, respectively (ρ_x=A_{sx}/t s; ρ_v=A_{sv}/t s).

These shear displacement curves shown in Figure 7.7 can be used as design tools for a simple strength design or for a more complex seismic design.

As far as the strength design approach is concerned, the panel shear strength, V_d, can be evaluated with the following simplified formula:

$$V_d = \frac{L}{s} A_s f_{yd} \sqrt{1+\upsilon/\rho_m} \qquad \textbf{(7.8)}$$

where L is the length of the panel, s is the size of the mesh grid, f_{yd} is the steel design stress ($f_{yd} = f_{yk}/1.15$), v is the non-dimensional parameter defined as ($\upsilon = N/Ltf_{cd}$), N is the axial load applied to the panel, t is the thickness of the panel, f_{cd} is the concrete design strength ($f_{cd} = f_{ck}/1.5$) and ρ_m is the mechanical reinforcement ratio ($\rho_m = A_s \cdot f_{yd} / (t \cdot s \cdot f_{cd})$). It should be noted that in this case $A_s = A_{sx} = A_{sv}$, f_{ck}*=26 MPa* and f_{yk}*=450 MPa*.

Eq. (7.8) has been derived combining the three equilibrium equations (i.e. Eqs. (7.3)) and neglecting the contribution of the concrete tensile stress (the assumption is based on the experiment observations commented on above), thus leading to a slightly conservative estimation of the panel strength. Values obtained from Eq. (7.8) for the three analyzed panels are represented by three horizontal dashed lines in Figure 7.7.

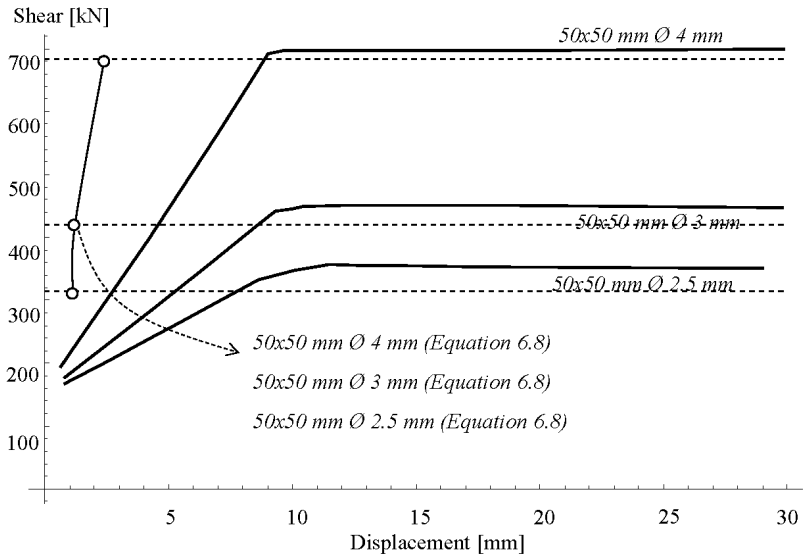

(a)

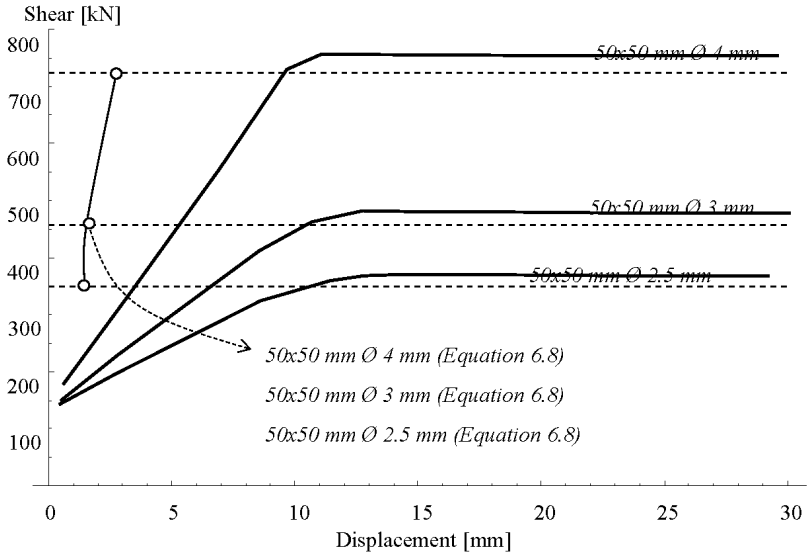

(b)

Figure 7.7: The force-displacement response of a full 3m x 3m panel for different reinforcement rations: (a) applied axial load equal to 100 KN; (b) applied axial load equal to 150 KN.

7.6. CONCLUSIONS

In the present chapters, refinements to the MCFT have been proposed in order to accurately predict the response of thin low reinforced RC sandwich panels subjected to in-plane shear and axial load. Experiments showed that the panel response cannot be fully described by the actual and most relevant shear theories, i.e. MCFT and RA-STM. The proposed refinements deal with the average concrete tensile stress-strain relationship which, from test results, appears to suddenly degrade after reaching cracking condition. This degradation depends on the applied axial load. Also a refinement for the model of the embedded bar has been introduced on the base of the proposed tension stiffening model for concrete. The introduced refinements, calibrated on the tests results, allow the RCFT to accurately fit the experimental data after concrete cracks and thus to predict the load-deformation behavior of the tested thin low-reinforced concrete panels. The preliminary numerical validations seem promising. However, additional experimental test data are required in order to fully calibrate the model parameters and further validate the obtained results.

8. Modelling of reinforced concrete sandwich walls according to a continuum damage theory

8.1. INTRODUCTION

The modeling of crack initiation and propagation is one of the most important aspects in the failure analysis of concrete structures. The cracking process in concrete is different from cracking of other materials, such as metal or glass, in that it is not a sudden onset of new free surfaces but a continuous forming and connecting of microcracks (Mehta and Monteiro 1993). From a macroscopic point of view, the formation of microcracks is represented as a softening effect on the behavior of the material, which causes the localization and redistribution of strain in a structure. This phenomenological behavior may be modelled using several different approaches. They can be subdivided into two main categories: (i) sophisticated models based on the continuum mechanics framework, which are aimed at describing the concrete behavior under a general state of stresses and strains, and (ii) simplified models typically calibrated on experimental data, such as those reducing the uniaxial compressive strength as a function of: the transverse tensile strain (Vecchio and Collins 1986, Belarbi and Hsu 1998), the anisotropic reinforcement producing a crack rotation (Mansour and Hsu 2005b), the maximum occurred compression (Mansour and Hsu 2005b).

As far as the first category of model is concerned, the following main contributions can be mentioned. First, the phenomenological behavior of cracking at the macroscopic level has been modeled using the framework of classical plasticity (Chen and Saleeb 1982). Nevertheless, this approach hardly reproduces the stiffness degradation due to cyclic loading also caused by the microcracking process (Gopalaratnam and Shah

1985). In continuum damage mechanics, the degradation can be modeled by defining the relationship between the Cauchy stress tensor and the effective stress tensor. Comprehensive reviews on continuum damage mechanics are given by Kachanov 1986 and Lemaitre and Chaboche 1990. In this regard, several models for concrete have been proposed in the past (Mazars 1986; Mazars and Pijaudier-Cabot 1989; Cervera *et al.* 1995). However, without the introduction of inelastic (or plastic) strains the continuum damage mechanics theory cannot provide an appropriate dilatancy control, which may become important for simulating plain and reinforced concrete structures under multiaxial loading. In the plastic-damage approach, stiffness degradation is embedded in a plasticity model (Simo and Ju 1987; Ju 1989; Lubliner *et al.* 1989; Yazdani and Schreyer 1990). In the coupled elastoplastic-damage model (Simo and Ju 1987; Ju 1989), the effective-stress concept in continuum damage mechanics is introduced to represent stiffness degradation.

A two scalar damage variables model has been proposed by Faria and his co-workers (Faria *et al.* 1998, Wu *et al.* 2006). The two damage variables (called positive and negative) are related to the degradation mechanisms occurring under tensile or compressive stress conditions (assumed as independent), respectively. Appropriate evolution laws are introduced for the damage variables and for the plastic strain tensor. Taking into consideration relevant thermodynamic principles, dissipation is checked and an intuitive constitutive law is proposed. Refinements to the model developed by Faria and others (Faria *et al.* 1998, Wu *et al.* 2006) has been recently proposed by Tesser and others (University of Padua) leading to a computationally efficient material model suitable for the seismic analyses of large RC structures.

In this chapter the fundamentals of the material model proposed by Tesser *et al.* 2011 are summarized and its main capabilities and limitations are briefly discussed. The model is first applied for the simulation of recent experimental tests of conventional RC shear walls (Lowes *et al.* 2011) designed according to modern seismic requirements. Then, the model is used to simulate the response of the RC sandwich panels analysed in the two previous chapters. Finally, an insight into specific aspects of the material model relevant for practical applications is conducted with the purpose of

providing advices for a proficient use of the model. The numerical analyses are carried out by means of the software OpenSees, an open source platform for the earthquake engineering simulations developed at the University of California Berkeley. In particular the software was enhanced by Tesser and his co-workers with the development of some modules for cyclic nonlinear analysis of reinforced concrete structures which are not yet included in the official release of OpenSees. The modules includes: a three dimensional concrete material model, a reinforced concrete membrane for plane stress finite elements and a reinforced concrete plate for plate/shell finite elements (Tesser *et al.* 2011).

8.2. THE CONCRETE DAMAGE MODEL FUNDAMENTALS: CAPABILITIES AND LIMITATIONS

The damage concrete model which is here adopted belongs to the class of energy-based isotropic continuum damage models and will be referred to as 3D Concrete Material (Tesser *et al.* 2011). The model is able to represent both tensile and compressive concrete failure modes, by means of two damage parameters, and also the microcracks opening and closing, by considering the spectral decomposition of the stress tensor. The complete theoretical formulation of the model and several validation examples are available in the works of Tesser *et al.* 2011. In this section, for the sake of clearness, the fundamentals of the model are briefly recalled.

The damage and plastic unloading processes are assumed to be elastic (Ju 1989). The split of the total strain tensor into "elastic-damage" and "plastic-damage" parts is assumed:

$$\varepsilon = \varepsilon_e + \varepsilon_p \qquad \textbf{(8.1)}$$

The free energy potential Ψ has been postulated according to the work of Faria *et al.* 1998. By imposing the Clausius-Duhem inequality that holds for any admissible process the damage and the plastic dissipation inequalities may be obtained (Faria *et al.* 1998):

$$-\left(\frac{\partial \psi}{\partial d^+}:d^+ + \frac{\partial \psi}{\partial d^-}:d^-\right) = -\frac{\partial \psi}{\partial d}:d \geq 0$$
$$-\frac{\partial \psi}{\partial \varepsilon_p}:\varepsilon_p \geq 0 \qquad \textbf{(8.2 a,b)}$$

Where d^+ and d^- are the positive and negative damage parameter respectively; $\boldsymbol{\varepsilon}^p$ is the plastic strain vector. The fourth-order damage tensor **D** can be defined by the following expression:

$$\mathbf{D} = d^+\mathbf{P}^+ + d^-\mathbf{P}^- \qquad \textbf{(8.3)}$$

with $\mathbf{P}^+$ and $\mathbf{P}^-$ standing for the fourth-order projection tensors (Wu *et al.* 2006): In order to be able to characterize the damage evolution, damage energy release rate functions need to be introduced. The thermodynamic force *Y*, also called damage energy released rate, is expressed as:

$$Y = -\frac{\partial \psi}{\partial d} \qquad \textbf{(8.4)}$$

With:

$$Y^+ = \sqrt{E_0\left(\bar{\sigma}^+ : C_0 : \bar{\sigma}^+\right)}$$
$$Y^- = \sqrt{3}\left(KI_1 + \sqrt{J_2}\right) \qquad \textbf{(8.5 a,b)}$$

the two components of *Y*. I_1 and J_2 are the first invariant of the effective stress tensor and the second invariant of the deviatoric effective stress tensor), E_0 is the concrete initial Young modulus, while *K* is a material property that accounts for the increase of compressive strength due to biaxial compression (Wu *et al.* 2006).

The following unique expression of the damage criterion can adequately account for the interaction between tensile and compressive damage evolutions:

$$g = \left(\frac{Y^+}{r^+} \right)^2 + \left(\frac{Y^-}{r^-} \right)^2 - 1 \leq 0 \qquad \textbf{(8.6)}$$

$$r_0^+ = f_0^+ = f_{ct}$$
$$r_0^- = \frac{\sqrt{3}}{3}\left(K - \sqrt{2} \right) f_0^- \qquad \textbf{(8.7 a, b)}$$

variables r^+ and r^- monitor the size of the expanding damage surface, while r_0^- and r_0^+ are the initial elastic damage thresholds for uniaxial tension and compression loadings respectively .

In addition to the damage criterion the evolution of the damage threshold is determined by the following flow rule:

$$\dot{r} = \dot{\gamma} \frac{\partial g(Y,r)}{\partial Y} \qquad \textbf{(8.8)}$$

Where $\dot{\gamma}$ is the damage consistency parameter. The related Khun-Tucker conditions give:

$$g(Y,r) < 0 \qquad \dot{\gamma} \geq 0 \qquad \dot{\gamma} g(Y,r) = 0 \qquad \textbf{(8.9)}$$

while the consistency condition is:

$$\dot{\gamma} \dot{g}(Y,r) = 0 \qquad \textbf{(8.10)}$$

The new damage threshold variables r can be computed with the Newton-Raphson method assuring the quadratic convergence of the material state determination.

Four parameters are necessary to determine the initial damage surface: r_0^+ and r_0^-, K and the Poisson ratio ν. Three common lab tests are sufficient to compute the value of those parameters: an uniaxial tension experiment allows to determine the tensile strength f_{ct}, an uniaxial compression test allows to obtain the uniaxial elastic limit f_0^- and the Young modulus E_0 , while a biaxial compression test allows to obtain the biaxial elastic limit $f_{0,2d}^-$.

The damage criterion of Eq. (8.6), that constitutes the damage surface, is displayed in Figure 8.1, which provides a 2-D representation for this surface, when $\bar{\sigma}_2$=0.

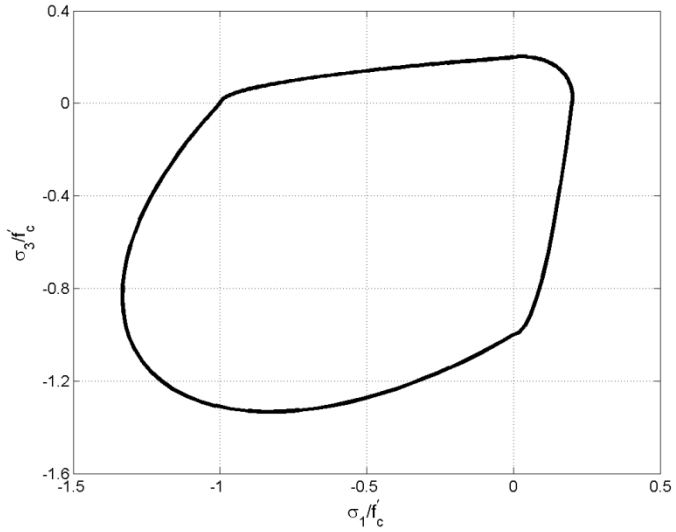

Figure 8.1: Initial elastic domain for plane stress state.

It can be easily verified that, in the compression field (Y^{+}=0), the damage criterion is equivalent to the modified Drucker-Pruger criterion. The elliptical shape of the damage criteria assures independent evolution of the positive and negative damage threshold for uniaxial tensile and compressive tests respectively. The damage parameter evolution laws are those proposed by Wu *et al.* 2006. The present constitutive model assumes that the damage criterion describes also the plastic surface so that the development of material damaging is simultaneous to the accumulation of irreversible strains for all the stress states. Recalling the work by Faria *et al.* 1998 the following plastic evolution law is adopted:

$$\dot{\varepsilon}_p = \beta E_0 \frac{<\bar{\sigma}:\dot{\varepsilon}>}{\bar{\sigma}:\bar{\sigma}} C_0^{-1}:\bar{\sigma} \qquad \textbf{(8.11)}$$

having introduced β for the plastic strain coefficient.

The parameters of the material model are summarized in Table 8.1.

Table 8.1: Parameters of the 3D Concrete Material model.

f_0^-	$f_{0,2d}^-$	f_{ct}	E_0	ν	β	A_n	B_n	A_p
elastic limit (1d)	elastic limit (2d)	tensile strength	Elastic modulus	Poisson's ratio	Plastic strain ratio	Damage parameter in compression	Damage parameter in compression	Damage parameter in tension

The above described concrete damage model can be efficiently used for the analysis of reinforced concrete structures. For in-plane analysis of 2-D planar walls a simple four-node lagrangian membrane element is suitable. The reinforcement can be modelled by using a smeared approach (Tesser *et al.* 2011) which implies that perfect bond between the concrete and the rebars. For 3-D analyse the four-node MITC shell element proposed by Dvorkin and Bathe 1984 is preferred.

The concrete damage model here presented has been mainly introduced for large-scale earthquake simulations of RC structures and therefore its computational efficiency is a fundamental issue. With this in mind, the authors of the model proposed a plastic strain evolution which introduces several simplifications with respect to the "effective stress space plasticity" (Ju 1989) used to couple the damage evolution and the plastic flows. The proposed law boosts the efficiency of the model, provided that the plastic strain rate remains parallel to the total strain rate and no additional iterations are required at the level of material state determinations. On the other hand, the assumption leads to a lower accuracy in predicting the concrete dilatancy.

Another important limitation of the proposed model for RC members is related to the assumed perfect bond between concrete and reinforcement, which may lead to less accurate local responses, such as stresses and strains at particular locations (e.g. where concrete spalling is more extended).

Moreover, at the present stage, no steel failure (such as steel fracture, buckling or low cycle fatigue failure) has been included; nonetheless the issue could be overcome by assuming a more complex constitutive models for the steel at the price of less computational efficiency.

8.3. THE SIMULATION OF THE EXPERIMENTAL TESTS OF CONVENTIONAL REINFORCED CONCRETE SHEAR WALLS

8.3.1. Experimental program

The assessment of the seismic behavior of conventional RC planar shear walls and coupled walls has been the objective of a recent research program at the NEES MUST-SIM (Multi-Axial Full-Scale Sub-Structured Testing and Simulation) facility at the University of Illinois in Champaign-Urbana.

Four test specimens are designed in order to be representative of a ten-story prototype wall of 36.6 m height, 9.1 m length and 46 cm thick. Due to limitation of the facility the specimens are one-third scale of the first three stories of the prototype. The following parameters vary among the specimens: (i) the lateral load distribution; (ii) the reinforcement layout; (iii) the presence of splice at the base.

Two reinforcement layouts are adopted, one with longitudinal reinforcement concentrated in the confined boundary region (referred to as Boundary Element (BE) layout) and the other with a uniform distribution of longitudinal reinforcement (referred to as Uniform layout). Figure 8.2 shows the two reinforcement layouts. The longitudinal reinforcement ratio in the boundary elements is equal to 0.0341, while it is equal to 0.0157 for the uniform layout.

The horizontal reinforcement ratio is equal to 0.0027 for both layouts. Three specimens present spliced longitudinal reinforcement at the base, while one specimen present continuous bars from the base to the top of the wall. Table 8.2 provides the design test matrix parameters for every specimen. Additional details related to the design of the specimens can be found in the report of the project (Lowes *et al.* 2011).

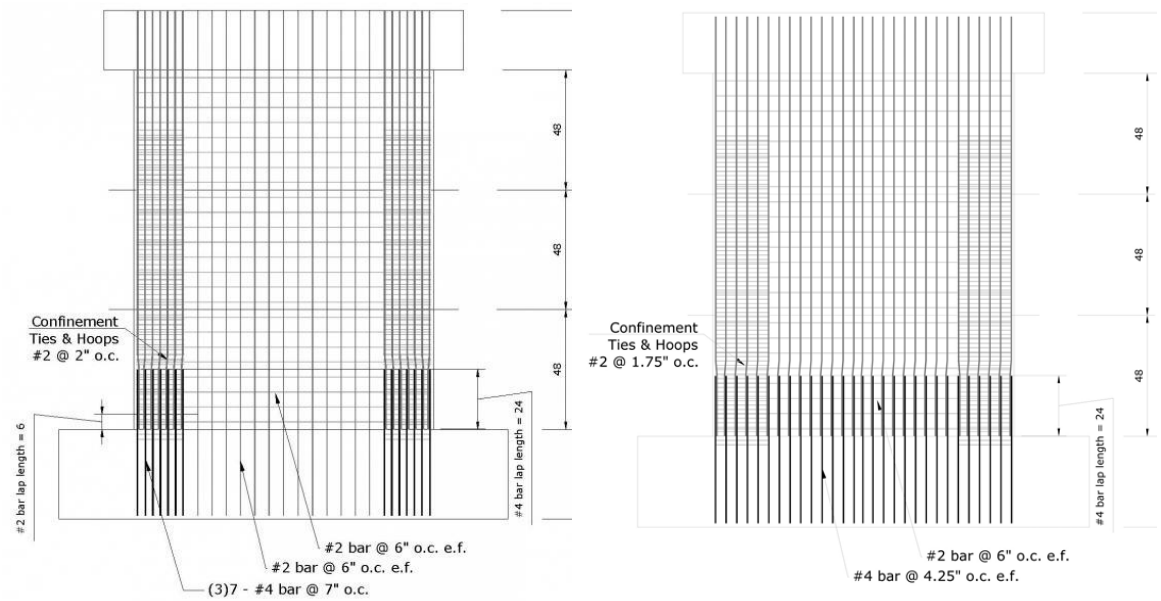

(a) (b)

Figure 8.2: (a) Boundary element layout; (b) Uniform layout (dimensions in inches)

Table 8.2: Design test matrix.

Specimen	Lateral Load distribution	Reinforcement layout	Presence of splice
PW1	ASCE 7	BE	Yes
PW2	Uniform	BE	Yes
PW3	ASCE 7	Uniform	Yes
PW4	ASCE 7	BE	No

The wall specimens were designed using a nominal concrete strength of 34.5 MPa and a nominal yield stress of 414 MPa. Table 8.3 summarizes the main properties of the concrete as obtained from cylinder tests. f'_c indicates the measured compressive strength, ε_{c0} is the strain at the peak compressive strength, E_c is the elastic modulus (estimated as $57{,}000\, f'^{\,0.5}_c$ psi and then converted in MPa), f_t is the tensile strength as determined from MOR tests.

The primary longitudinal reinforcement was standard #4 Grade 60 deformed bars. Specimens PW1 and PW2 were built using the same batch of steel. The # 2 rebars were subjected to a special thermal treatment in order to augment the deformation properties

of the not treated bars, which exhibited quite low ultimate strains (of the order of 0.05). The main experimental properties of the steel bars are summarized in Table 8.4.

Table 8.3: Concrete material properties.

Specimen	f'_c [MPa]	ε_{c0} [$\cdot 10^{-3}$]	E_c [MPa]	f_t [MPa]
PW1	36	2.27	28380	7.1
PW2	40	2.51	30000	7.3
PW3	34	2.85	27680	7.0
PW4	29	2.07	25640	6.0

Table 8.4: Steel material properties.

Specimen	f_y [MPa]	ε_y [*10-3]	f_{max} [MPa]	ε_u [*10-3]
PW1 & PW2 #4	578	2.9	694	12
PW3 #4	353	1.8	483	20
PW4 #4	462	2.3	753	13
All #2	520	2.6	582	5.8*

*the value is referred to the not-treated bars

8.3.2. Test setup

Loads are applied using the Load and Boundary Condition Boxes (LBCBs) allowing the control of all the six degrees of freedom. In order to reach the peak strengths, the use of two LBCBs was required. Applied loads consist of a constant axial load equal to 10% of the nominal axial capacity of the wall (1601 kN) and reversed cyclic lateral forces and overturning moments. The ratio between the applied overturning moment and lateral force (which is kept constant during each test) varies from specimen to specimen according to the lateral load distribution. The tests were displacement controlled with the control point located at the mid span of the top of the wall. The load history is composed of complete cycles of increasing amplitude up to a story drift of 1.5% of the height. A total of nine increasing drifts, each one composed of three complete cycles, were intended to be applied.

The instrumentation used to collect data from the experimental tests is composed of traditional measurement systems (strain gauges and LVDTs) and advanced measurement systems including an optical measuring machine (CMM), able to record

the motion of the specimen during the test (data are acquired at approximately 1 Hz) and high-resolution cameras. Additional details on the test set up and measurement instrumentation are available in the in the report of the project (Lowes *et al.* 2011).

8.3.3. The numerical models

The numerical models and the simulations of the experimental tests have been developed using the software OpenSees (Mazzoni *et al.* 2006). Because of the planar geometry of the wall specimens and the in-plain loading, 2D membrane elements are used (i.e. the out of plane stresses are condensed out). The smeared approach is adopted to model the vertical and longitudinal reinforcement, thus allowing a significant reduction in the computational effort. In the present work the Giuffrè-Menegotto-Pinto law with the isotropic hardening introduced by Filippou *et al.* 1983 is used.

The effect of the concrete confinement (which cannot be directly captured by the model) has been computed according to the model of Kent and Park 1971. In more details, the following procedure is applied: (i) the constitutive laws for the unconfined material are obtained according to the results of the experimental tests; (ii) the stress-strain relation for the confined concrete is estimated using the Kent and Park model; (iii) the model parameters f_0^-, $f_{0,2d}^-$ and A_n are adjusted (with a fitting procedure) in order to match the Kent and Park 1971 stress-strain relationship. Table 8.5 and Table 8.6 give the values of the parameters adopted for the concrete and steel model. Figure 8.3 displays the stress-strain relations for the unconfined and confined concrete adopted for the specimens PW1. Similar curves are obtained for the other specimens. Zero concrete tensile strength is assumed as a result of the comparison between numerical simulations and experimental results at low drift values.

The mesh of the reinforced concrete wall is composed of 12x14 square elements having 25 cm side length.

Table 8.5: Material parameter adopted for each specimen

Specimen	$f_c^{'}$ [Mpa]	E_c [Mpa]	f_0^{-} [Mpa]	β	A_n	B_n
PW1	36	28380	21.6	0.5	1.5	0.75
PW2	40	30000	24	0.5	1.5	0.75
PW3	34	27680	20.4	0.5	1.5	0.75
PW4	29	25640	17.4	0.5	1.5	0.75

Table 8.6: Parameters for the #4 steel bar for each specimen.

Specimen	f_y [Mpa]	E_s [Gpa]	R_0[Mpa]	B	C_{R1}	C_{R2}	a_1	a_2
PW1	578	198	21.6	0.5	1.5	0.75	0.04	1.0
PW2	578	198	24	0.5	1.5	0.75	0.04	1.0
PW3	353	198	20.4	0.5	1.5	0.75	0.04	1.0
PW4	462	198	17.4	0.5	1.5	0.75	0.04	1.0

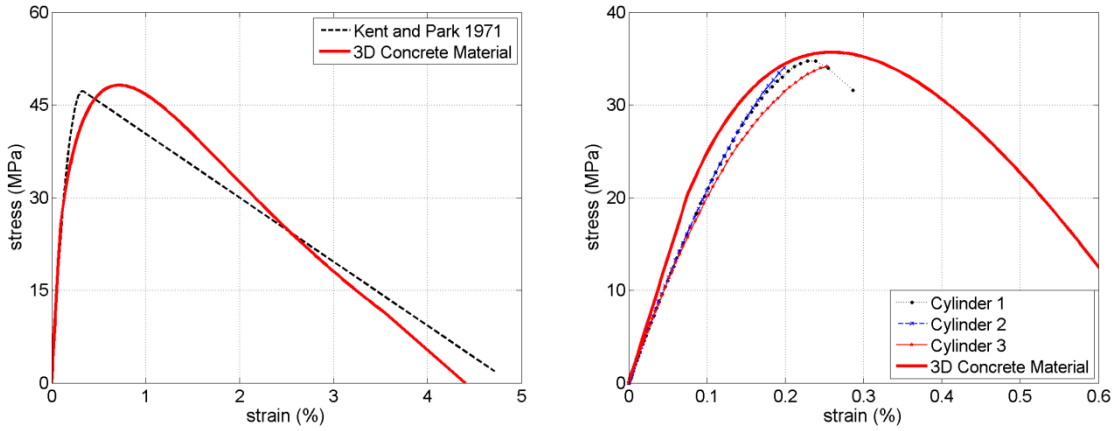

(a) (b)

Figure 8.3: (a) Stress-strain relation for the confined concrete; (b) Stress-strain relation for the unconfined concrete.

The foundation and the wall cap are included in the model as linear elastic elements with the same elastic modulus of the non-linear concrete model. Figure 8.4 shows the mesh of the model. Loads are applied at the mid height of the wall cap. The vertical load is applied under force control, while the horizontal in-plane load is applied under displacement control according to the prescribed protocol.

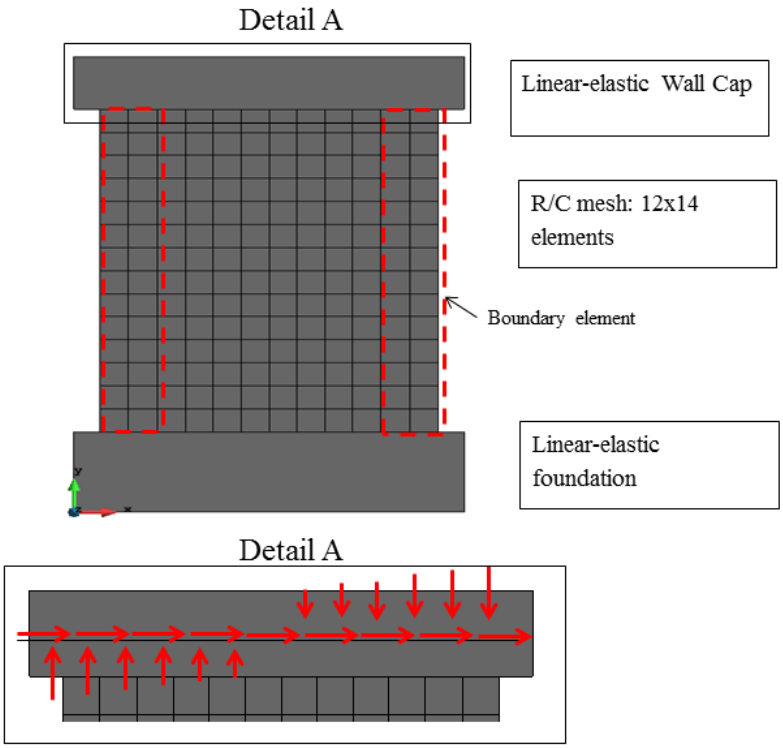

Figure 8.4: Model geometry and schematic representation of the applied load.

In order to reproduce the actual loading protocol and the boundary conditions at the top wall, the effect of the applied top moment M_y is simulated by imposing a double triangle distribution of vertical displacement at the nodes located at the mid-depth of the wall cap (see Figure 8.4).

8.3.4. Results of the numerical simulations

This section provides a summary of the main results obtained from the numerical simulations as well as comparisons between numerical and experimental results. In the test report (Lowes *et al.* 2011) it is highlighted that the specimen PW4 experienced a non-negligible out-of-plane displacement which reduced the in-plane theoretical capacity. For this reason, the following discussions are limited to the specimen PW1, PW2 and PW3.

First, monotonic pushover analyses are carried out to obtain the capacity curve of each specimen. Using the contour plots of the damage variable d_n Damage State Limits

(DSLs) are defined (details are available in section 7.5). These values should be useful for design purposes. Then, cyclic analyses are performed and the results are compared with the experimental ones: both global responses, in terms of load-displacement behavior and damage evolutions, and local responses are analysed.

8.3.4.1. Monotonic Pushover Analyses

The lateral capacity curves of the studied specimens are displayed in Figure 8.5 in terms of base shear vs. story drift. The models of PW2 and PW3 exhibit the same initial linear response up to a drift around 0.1%, while the initial response of the model of PW1 is slightly less stiff. The more flexible initial response of the model of PW1 is due to the different boundary conditions imposed at the top beam resulting from the different applied lateral loads distribution (triangular vs. uniform). The peak strength exhibited by the model of PW1 is approximately equal to 760 kN and is reached around 0.5% drift. The peak strength is maintained quite constant between 0.75% and 1.50% drift, thus providing a good ductile response. The peak strength of the model of PW2 is approximately equal to 1000 kN and is reached at approximately 0.7% drift. After the peak strength, strength decay is observed (10% decay from 0.7% to 2% drift). The model of PW3 shows a peak strength of 810 kN. After the peak, a similar strength decay of PW2 model is observed. The significant increases in strength showed by PW2 model has to be attributed to the presence of the boundary elements and partially to the higher concrete strength. It has to be noted that the pushover curves are obtained neglecting the tensile strength of the concrete, thus providing a conservative estimation of the specimen shear strength (i.e. peak base shear).

The contour plots of the damage variable d_n is used to identify the achievement of specific Damage State Limits (DSLs). In this study, the DSLs are defined as follows:

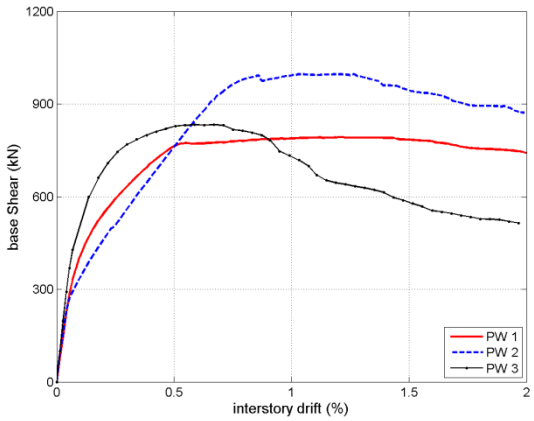

Figure 8.5: Pushover curves for specimen PW1, PW2 and PW3 as obtained from numerical simulations.

- DSL_1 is reached when d_n approaches 0.6. At this damage level the longitudinal rebars start yielding and therefore it can be considered as the "yielding point";
- DSL_2 is reached when d_n approaches 0.7. At this level the concrete locally approaches its peak strength;
- DSL_3 is reached when d_n approaches 0.8. At this level of damage concrete strength starts to degrade and initial spallling could be observed;
- DSL_4 is reached when d_n approaches 0.9. The concrete residual strength is approximately equal to 0.8 of the peak strength; spalling could be observed.
- DSL_5 is reached when d_n approaches 0.95. At this level of damage concrete residual strength is approximately equal to 0.1 of the peak strength; concrete approaches crushing;
- DSL_6 is reached when d_n approaches 1.0. At this level of damage concrete has no residual strength and stiffness and crushing could be observed. Typically at this state of damage also the rebars may fail due to buckling (or due to low-cycle fatigue in the case of cyclic loads) ;

Further details are provided in section 7.5. The values of the base shear and leading to each DSLs are collected in Table 8.7 and

Table 8.8. It can be noted that PW1 model is characterized by a higher ductility with respect to PW3 (the drift at DSL_6 for the model of PW1 is 60% higher than that for specimen PW3), despite a small increase in the peak strength (7%). This

behavior can be again explained by the presence of the boundary elements. Contour maps of the damage variable d_n are displayed in Figure 8.6.

Table 8.7: Base shear and drift at each DLS for the specimen PW1.

	DSL_1	DSL_2	DSL_3	DSL_4	DSL_5	DSL_6
V_{base} [kN]	468	549	694	743	754	745
Drift [%]	0.38	0.51	0.75	1.00	1.40	1.62

Table 8.8: Base shear and drift at each DLS for the specimen PW3.

	DSL_1	DSL_2	DSL_3	DSL_4	DSL_5	DSL_6
V_{base} [kN]	420	463	614	702	710	700
Drift [%]	0.25	0.30	0.50	0.75	0.90	1.00

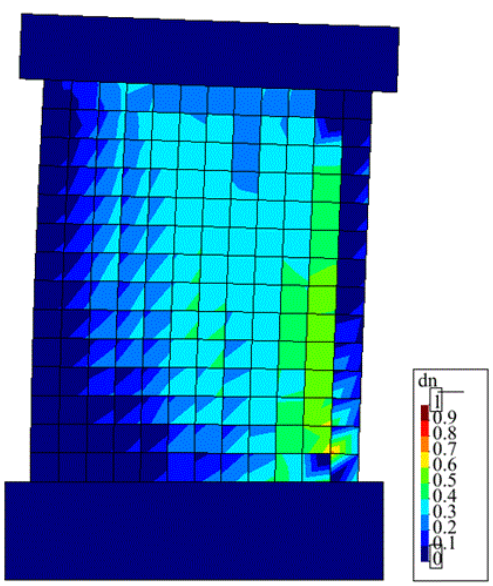

(a) SDL_1

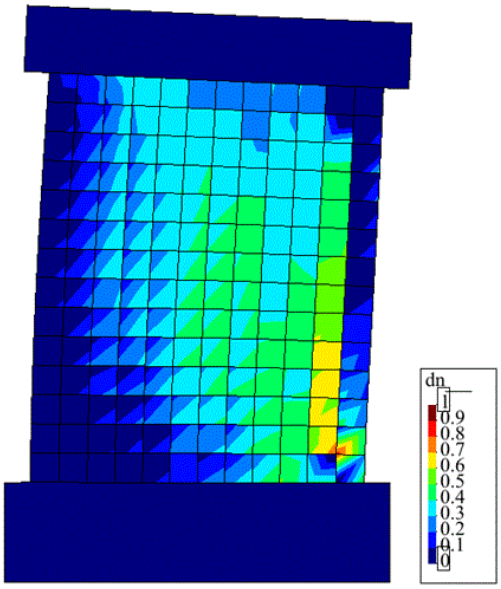

(a) SDL_2

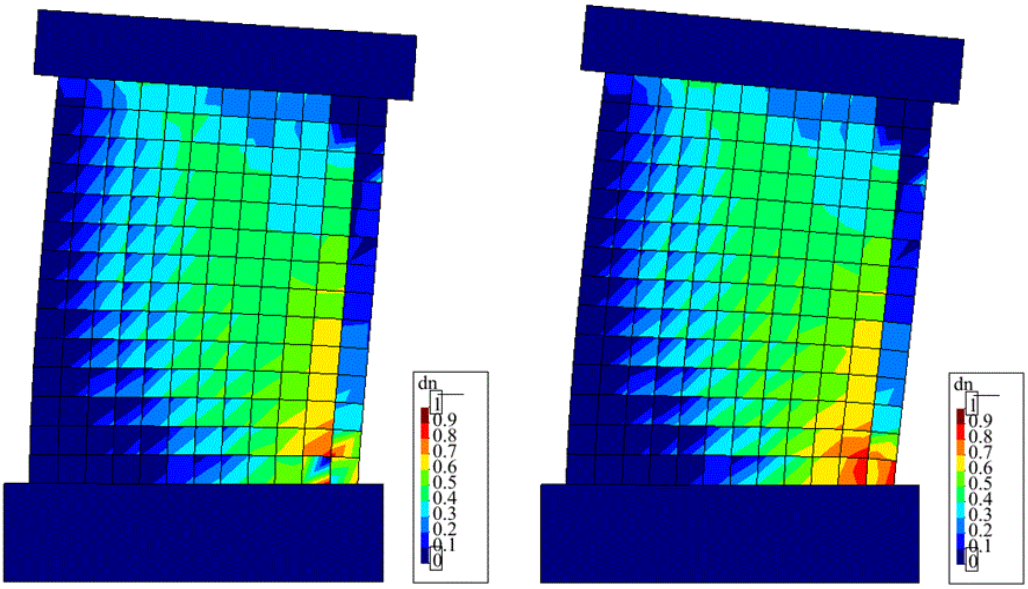

(c) SDL_3 (d) SDL_4

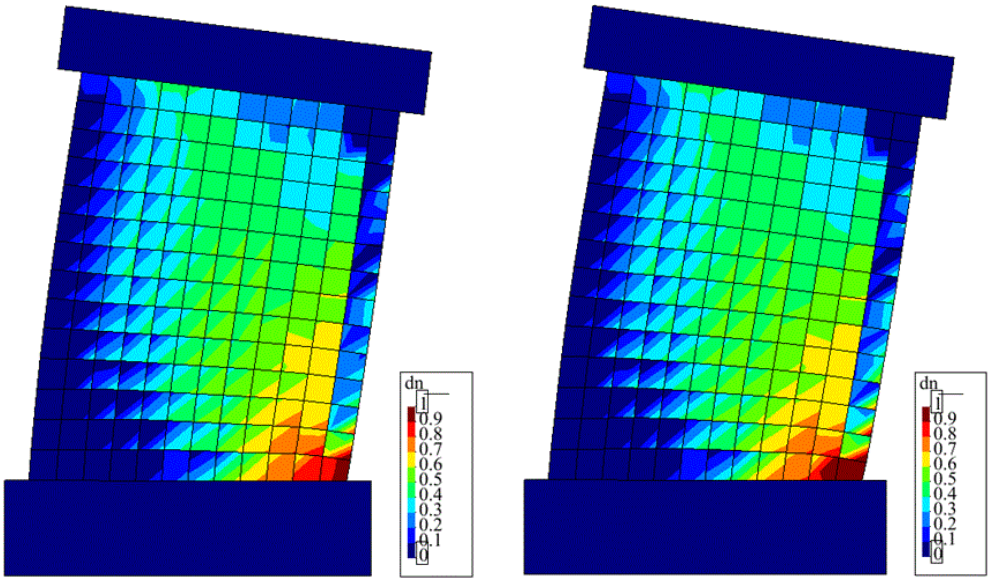

(e) SDL_5 (f) SDL_6

Figure 8.6: Color contour maps of the damage variable d_n for specimen PW1.

8.3.4.2. Cyclic Analyses

This section compares the experimental cyclic response of the specimens with the results of the numerical simulations. First, the global force-displacement responses are

analysed. Then, the damage evolution is discussed. Finally, local responses (stress-strain response histories) are investigated.

The experimental and numerical hysteretic responses in term of base shear vs. story drift are represented in Figure 8.7. The numerical model is able to well simulate the main features of the global experimental cyclic behavior in terms of peak strength, envelope response and hysteretic behavior. Contour maps of the damage variable d_n at selected drifts are displayed in Figure 8.8 and Figure 8.9.

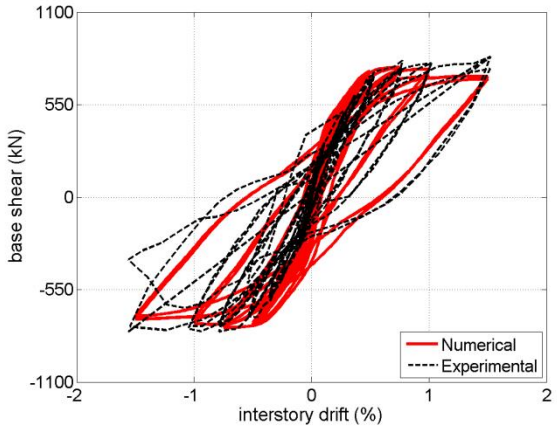

(a)

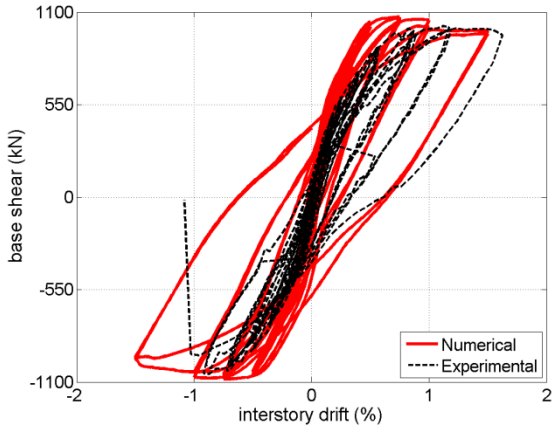

(b)

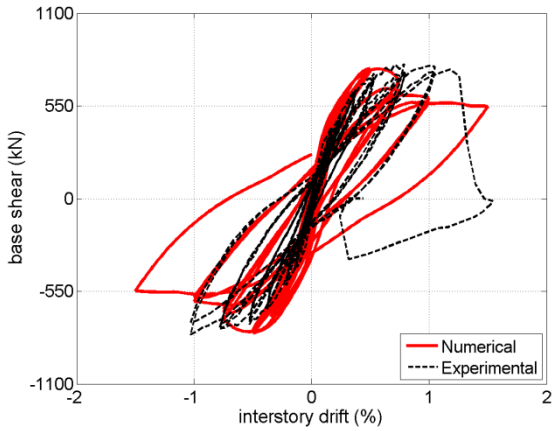

(c)

Figure 8.7: Comparison between the experimental and numerical cyclic response. (a) Specimen PW1; (b) Specimen PW2; (c) Specimen PW3.

Table 8.9 provides the peak values of d_n at each imposed drift. The evolution of the damage obtained from the numerical analysis appears consistent with the damages observed during the test which can be summarized as follows (extracted from Lowes *et al.* 2011):

- *Horizontal cracking initiated at 0.10% drift.*
- *Diagonal cracking initiated at 0.10% drift.*
- *Vertical cracks initiated at 0.35% drift.*
- *Compressive yield of the extreme vertical reinforcing bars was indicated by strain gauges at 0.20% drift.*
- *Tensile yield of extreme vertical reinforcing bars was indicated by strain gauges at 0.42% drift.*
- *Cover spalling initiated above the splice during the first cycle at 0.75%.*
- *Longitudinal reinforcement was exposed above the splice during the third cycle to 0.75% drift.*
- *Damage (crushing) of the confined core of the boundary element was observed above the splice during the first half cycle (ER+) to 1.5% drift.*
- *Failure occurred due to extensive bar buckling and core crushing in the west (left) boundary element above the splice at 1.05% drift in the first WL- cycle to 1.05% drift.*

The overall damage evolution of PW2 model obtained from the numerical simulations is similar to that of PW1 model: DSL_1 is reached approximately at 0.5% drift, while the last DSL (i.e. DSL_6) is reached between 1.0% and 1.5% drift. Nonetheless, the DSLs are reached at slightly less drift, meaning a less ductile behavior of the numerical model.

The damage evolution for PW3 as obtained from the numerical simulation is quite different than that of PW1 and PW2: the DSL_1 is approached at 0.347% drift; the DSL_2 is reached around 0.5% drift, DSL_3 and DSL_4 are reached between 0.5% and 0.75%, DSL_5 is reached at 0.75%, DSL_6 is reached at 1.0% drift. The progression of damage obtained for PW3 appears consistent with the experimental observation, which can be summarized as follows (extracted from Lowes *et al.* 2011):

- *Tensile yield of extreme vertical reinforcing bars was indicated by strain gauges at 0.17% drift.*
- *Compressive yield of extreme vertical reinforcing bars was indicated by strain gauges at 0.32% drift.*
- *Cover spalling initiated above the splice at 0.52% drift.*
- *Web crushing was observed at 0.75% drift.*
- *Bar buckling was observed above the splice during the first cycle to 1.0% drift.*
- *Damage (crushing) of the confined core of the boundary element was observed above the splice during the second (and final) cycle to 1.0% drift.*
- *Failure occurred due to extensive bar buckling and core crushing in the east (right) boundary element above the splice at 1.28% drift during the first ER+ half cycle to 1.5% drift.*

For the sake of clearness, color contour maps of the damage variable d_n for the models of PW1 and PW3 are provided in Figure 8.8 and Figure 8.9, respectively. For PW1 model the damage remains more concentrated in the boundary elements, while for specimen PW3 the damage is spread also in the web. The results are consistent with the experimental observations.

Table 8.9: Peak Negative Damage Variable dn at each peak drift (first of the three cycle).

Specimen	d=0.1%	d=0.347%	d=0.5%	d=0.75%	d=1.0%	d=1.5%
PW1	0.33	0.44	0.57	0.79	0.96	1.00
PW2	0.39	0.54	0.65	0.85	0.98	1.00
PW3	0.45	0.57	0.75	0.95	1.0	1.00

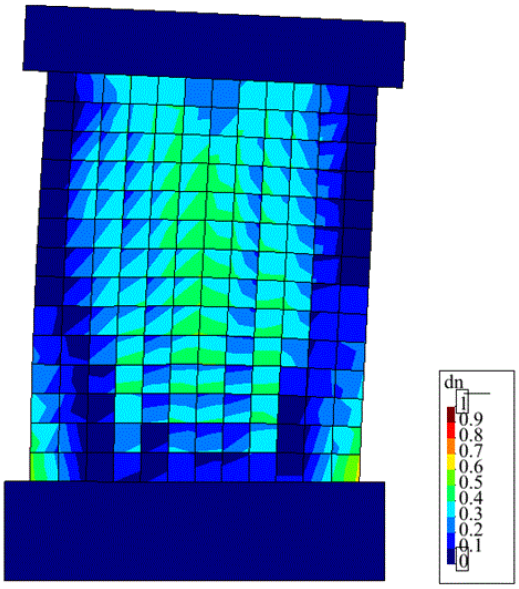

(a)

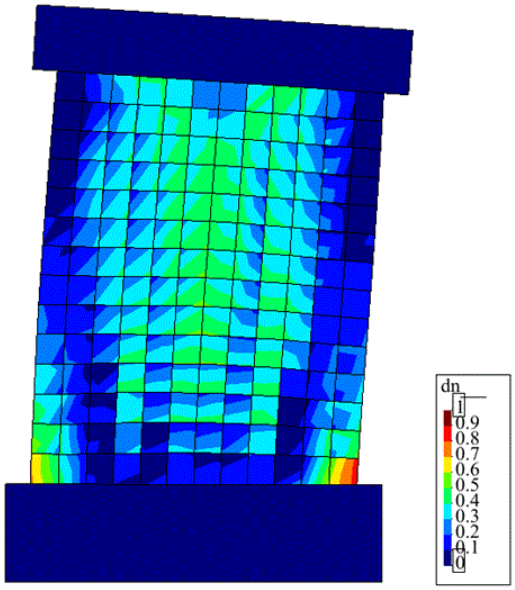

(b)

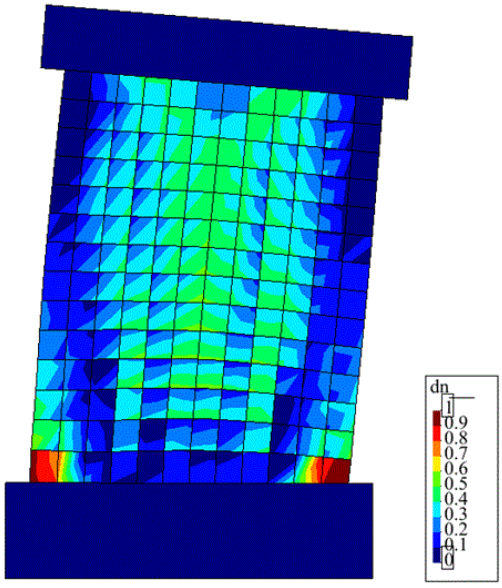

(c)

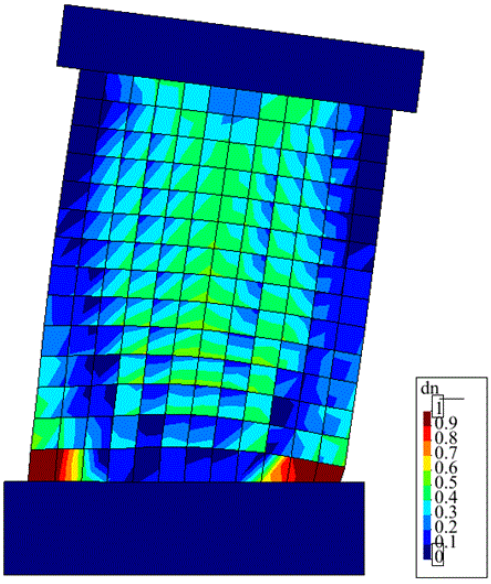

(d)

Figure 8.8: Color contour maps of the damage variable d_n for specimen PW1: (a) d=0.5%; (b) d=0.75%;(c) d=1.0%;(d) d=1.50%.

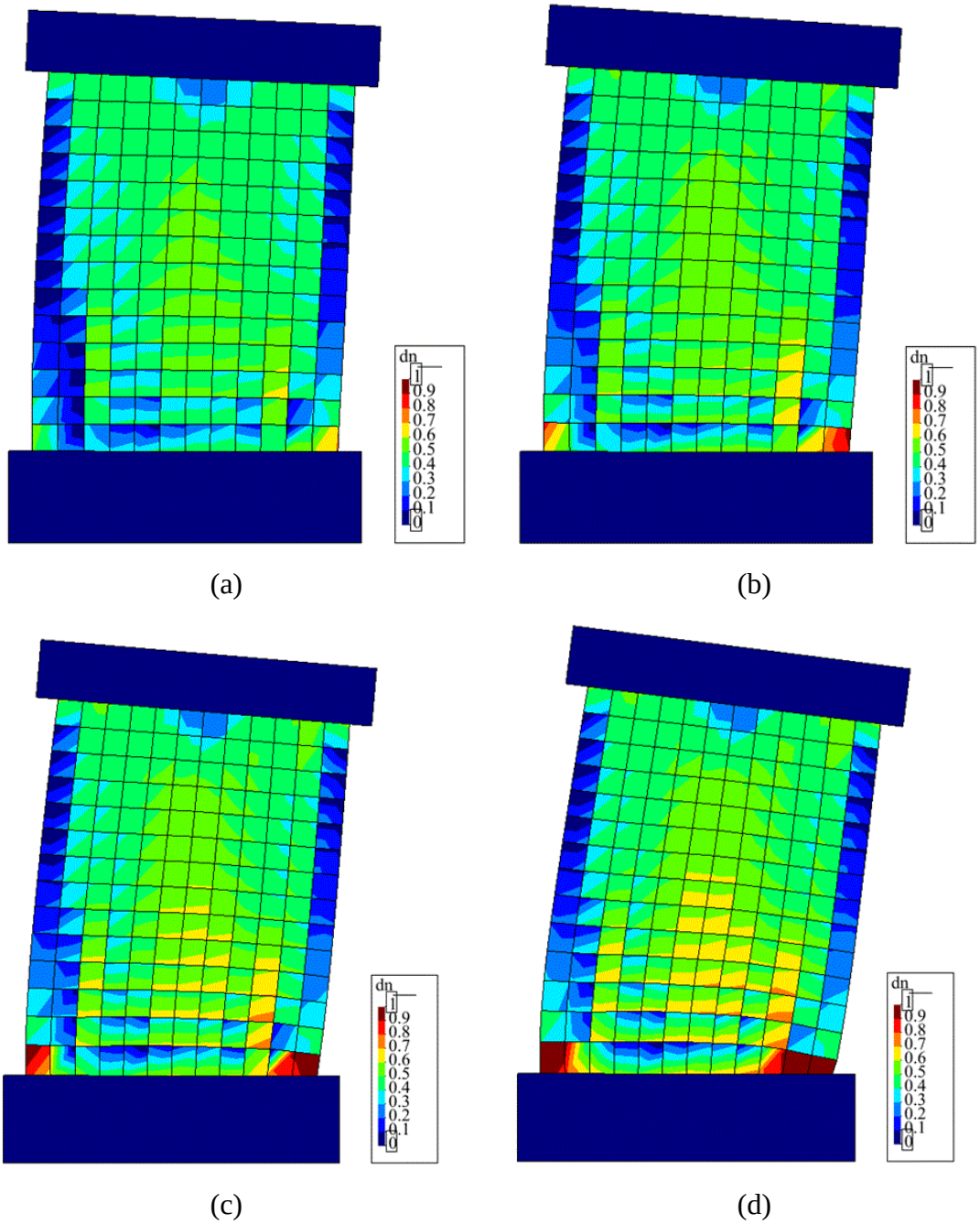

Figure 8.9: Color contour maps of the damage variable d_n for specimen PW3: (a) d=0.5%; (b) d=0.75%;(c) d=1.0%;(d) d=1.50%.

In Figure 8.10 the experimental and numerical strain history of the longitudinal reinforcement at some locations at the base of specimen PW1 are compared.

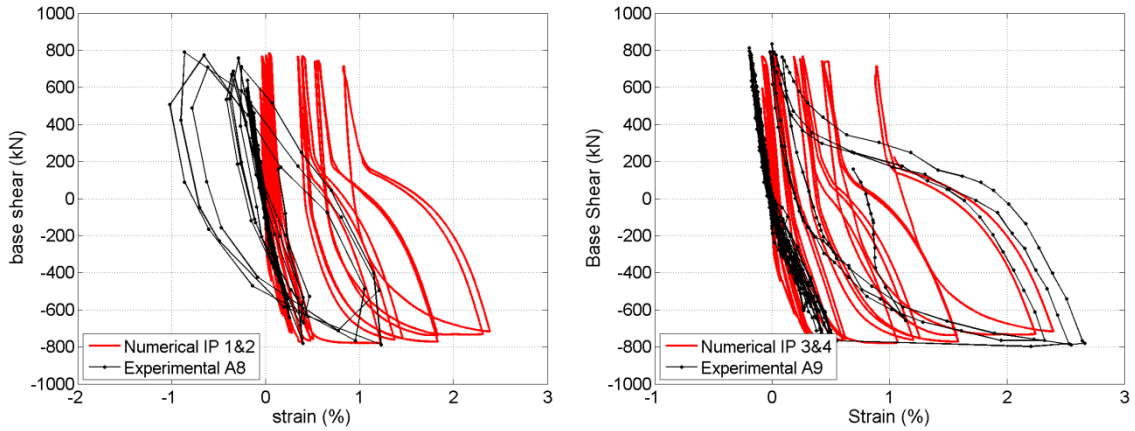

(a) (b)

Figure 8.10: Comparison between the experimental and numerical strain history of the longitudinal reinforcement at specific locations of the base of the wall for the specimen PW1. (a) East Boundary element; (b) West Boundary element

The strain response provided by the numerical simulations seems to be quite accurate. It should be recalled that perfect bound between concrete and reinforcement is assumed. Clearly, this assumption may affect the accuracy of the local stress-strain results.

8.4. THE SIMULATIONS OF THE RC SANDWICH WALL TESTS

8.4.1. Planar walls

The mesh geometry of each PW is made of four-node membrane elements with side length of 25 cm. The foundation and the loading beam are modelled as linear-elastic elements. The parameter of the 3D Concrete Material are partially obtained from results of material tests (i.e. f_0^-, E_0, A_n) and partially assumed (all the rest). The concrete tensile strength of the model has been reduced to account for pre-cracking due to constrained shrinkage. The numerical values of the parameters are summarized in Table 8.10. The Giuffrè-Menegotto-Pinto model with isotropic hardening introduced by Filippou et al. 1984 has been used for the reinforcement. Steel yield strength of 450 MPa has been adopted, based on the results of material tests.

Table 8.10: Parameter values for the 3D Concrete Material (PW specimens).

f_0^- [MPa]	$f_{0,2d}^-$ [MPa]	f_{ct} [MPa]	E_0 [MPa]	ν	β	A_n	B_n	A_p
15	18	0.1	28000	0.0	0.5	2.0	0.75	0.1

For each planar wall, two different models are developed:

- Type A models: perfect bound between the wall and the foundation is assumed. This model is used to evaluate the capacity of the wall assuming no slip at the base;
- Type B models: slips between the wall and foundation are included through the insertion of zero-length elements (Mazzoni et al. 2006) between the wall and foundation. The zero-length elements are active along the horizontal direction and their hysteretic response is modelled using the Scott and Filippou pinching model available in the OpenSees library (see Mazzoni et al. 2006).

Both monotonic pushover and reversed cyclic pushover analyses have been carried out. The former are performed only on the type A models with the purpose of estimating the capacity curve of the model and the evolution of damage under monotonic loadings (i.e. Damage State Limits, DSLs) assuming no slip between the wall and the foundation; the latter are performed on both type A and type B models in order to evaluate the effect of the relative slips between wall and foundation on the seismic response of the wall.

8.4.1.1. Monotonic pushover analyses

Figure 8.11 displays the monotonic pushover curves for all planar specimens together with the corresponding envelopes as obtained from the experimental data. Contour maps of the damage variable d_n for a full panel (specimen PW1) and a perforated panel (specimen PW4) are given in Figure 8.12 and Figure 8.13, respectively. Each map corresponds to a specific DSL (i.e. peak damage variable d_n equal to 0.6, 0.7, 0.8, 0.9, 0.95, 1.0, respectively). Values of inter-story drift leading to each DSL are collected in

Table 8.11. Damage varies from reinforcement yielding (DSL_1) to concrete spalling (DSL_4) and crushing (DSL_6).

The inspection of the pushover curves of Figure 8.11 clearly shows that the numerical simulations allow to reasonably approximate the experimental envelope response in terms of stiffness and peak strength. Nonetheless, the contour maps of Figure 8.11 and Figure 8.12 show that all the panels (and especially the ones with the central opening) reach the ultimate conditions (DSL_6) at values of lateral drifts between 0.7% and 1% which are generally below the experimental ones.

In other words, the results of the pushover analyses indicate that: (a) the model type A seems adequate to simulate the experimental stiffness and strength but not the ultimate drifts; (b) walls with base connections preventing relative slips should experience significant damages at story drifts around 0.7% -1.0% story drift. However, experimental tests with special attention devoted to prevent the slip at the base are necessary to validate these results.

Table 8.11: Values of drifts at each DLS.

d_n	DSL_1	DSL_2	DSL_3	DSL_4	DSL_5	DSL_6
PW1	0.25%	0.35%	0.50%	0.70%	0.84%	0.95%
PW4	0.12%	0.20%	0.30%	0.40%	0.55%	0.70%

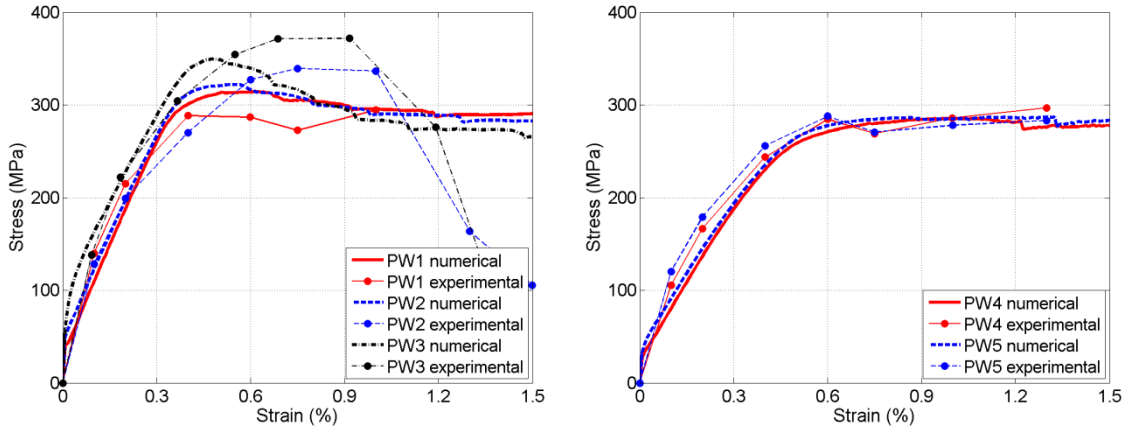

(a) (b)

Figure 8.11: Comparison between the envelope of the experimental response and the numerical simulations: (a) PW1, PW2 and PW3; (b) PW4 and PW5.

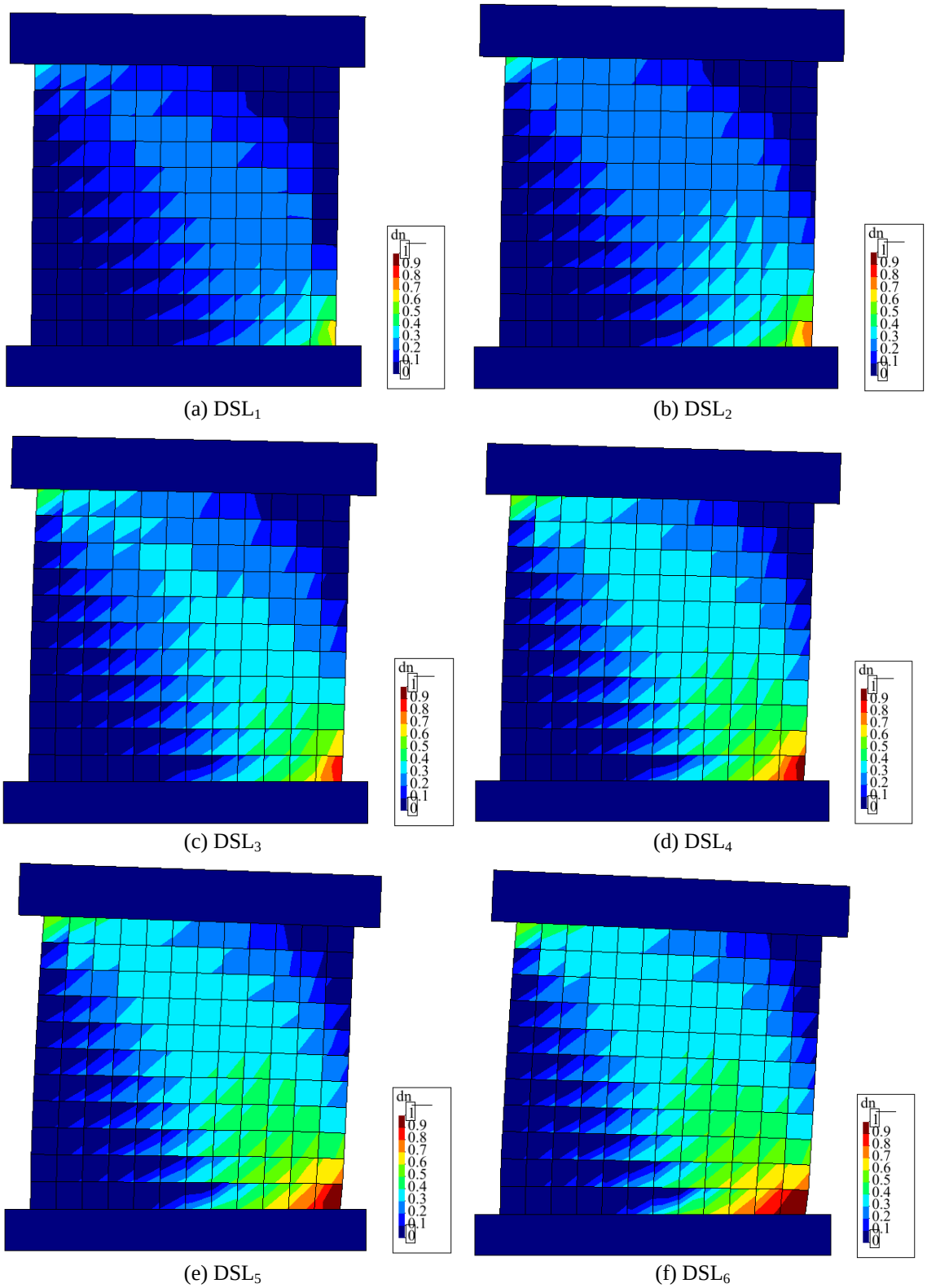

(a) DSL_1 (b) DSL_2

(c) DSL_3 (d) DSL_4

(e) DSL_5 (f) DSL_6

Figure 8.12: Color contour maps of the damage variable d_n for the specimen PW1 at each DSL.

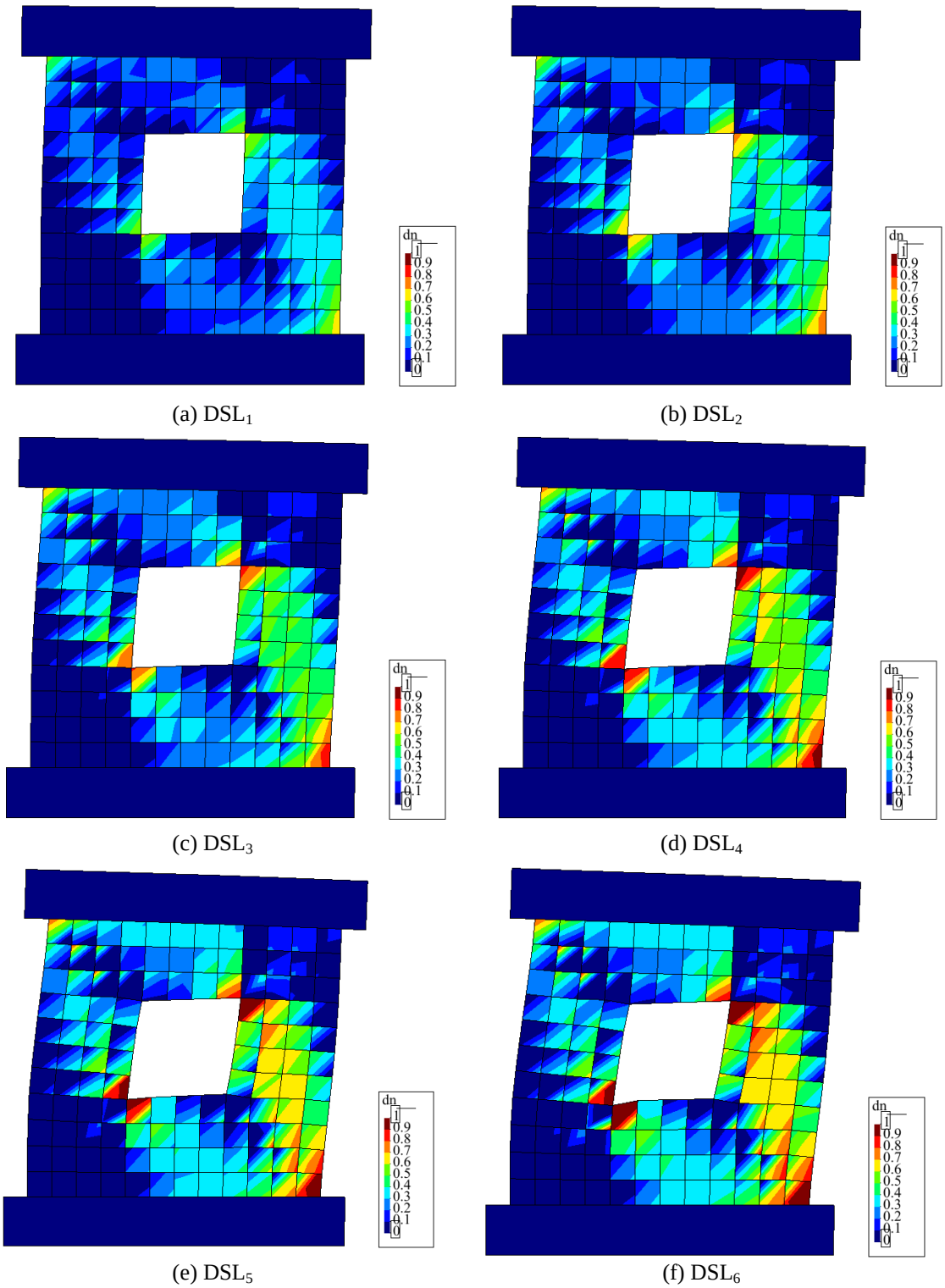

(a) DSL_1 (b) DSL_2

(c) DSL_3 (d) DSL_4

(e) DSL_5 (f) DSL_6

Figure 8.13: Color contour maps of the damage variable d_n for the specimen PW4 at each DSL.

8.4.1.2. Cyclic analyses

The cyclic response as obtained from the numerical simulations on type A models is represented in Figure 8.14 together with the experimental response in terms of base shear vs. story drift. First, it can be observed that all numerical responses overestimate the experimental peak strength. The pinching is poorly captured by the model. Moreover, the significant strength deterioration experienced by specimens PW2 and PW3 after a story drift of approximately 0.75% is not captured by the models. On the contrary, the numerical response of the models PW4 and PW5 (the ones with the central opening) is characterized by a fast strength degradation at large drift which is not shown by the experimental responses. The numerical response of model PW5 at the last imposed inter-story drift is characterized by practically null strength. The fast strength decay observed by the numerical simulation (PW4 and PW5) is explained by a damage localization at base of the opening leading to a sort of sliding shear failure as shown by the contour maps of the damage variable d_n for PW4 (Figure 8.14). During the experimental tests no signs of such a mechanism of damage were observed. On the contrary, as already mentioned, significant sliding at the base of the walls characterized the experimental behavior.

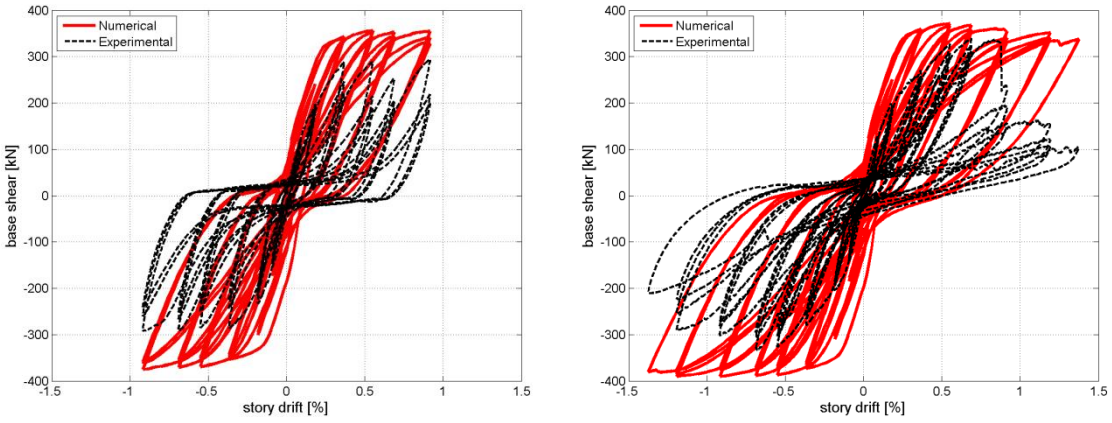

(a) (b)

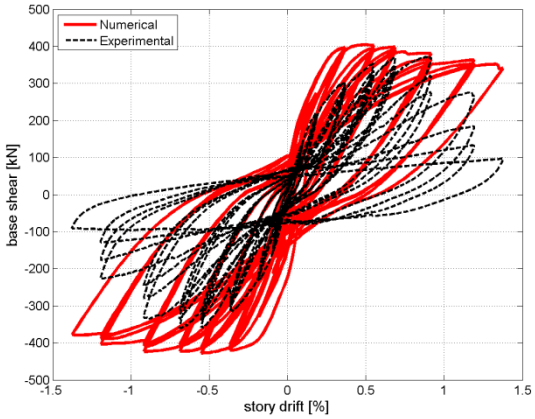

(c)

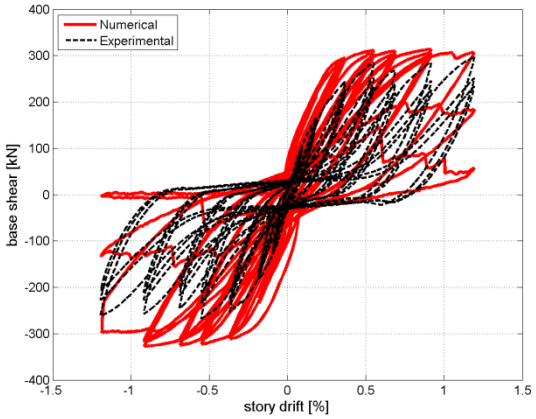

(d)

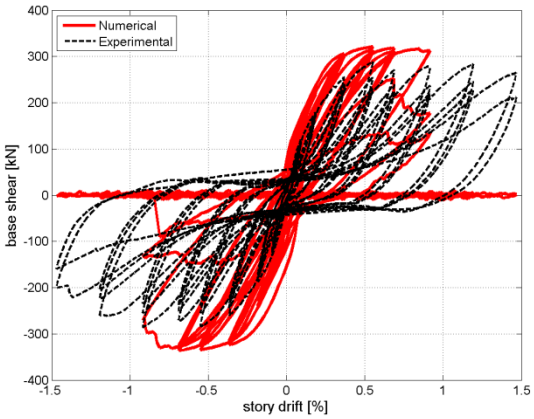

(e)

Figure 8.14: Comparison between the numerical cyclic simulations (type 1 models) and experimental response: (a) PW1; (b) PW2; (c) PW3; (d) PW4; (e) PW5.

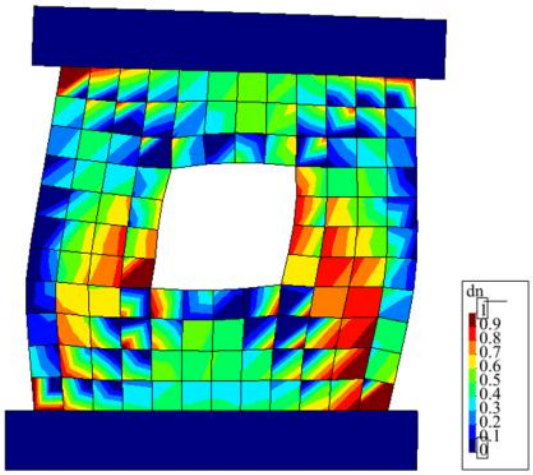

(a)

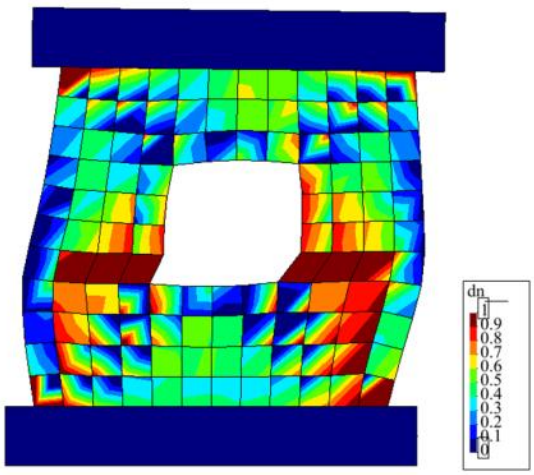

(b)

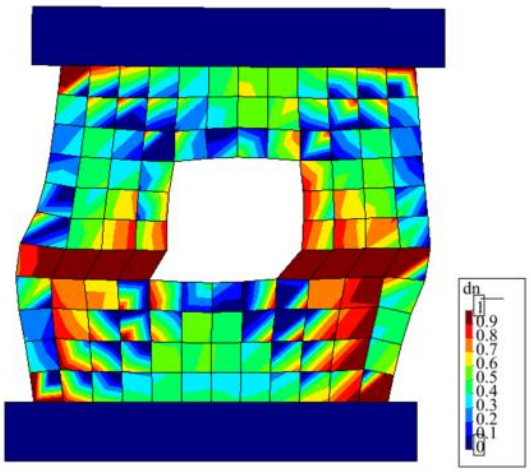

(c)

Figure 8.15:Color ontour maps of the damage variable d_n for specimen PW4 at the three peaks at 1.0% story drift: (a) first cycle; (b) second cycle; (c) third cycle.

The numerical simulations of the experimental tests (type B models) are represented in Figure 8.16 in terms of base shear vs. story drift together with the experimental responses. The presence of the zero-length elements allows to better reproduce the pinched shape of the experimental response and at the same time determines a reduction of the panel damage, particularly at the bottom. Contour maps of the damage variable d_n at a drift equal to 1% are displayed in Figure 8.17. The numerical response of type B models well correlate with the experimental evidences: the presence of base connectors, allowing a relative slips between the walls and the foundations, leads to a remarkable damage reduction and has to be considered in the design phase.

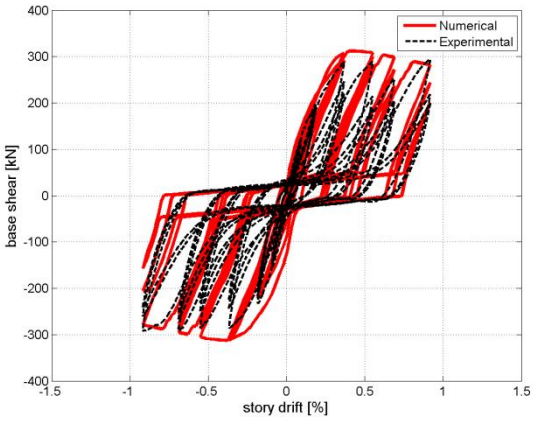

(a)

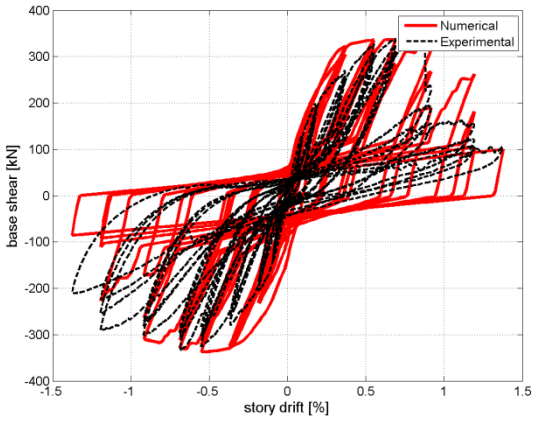

(b)

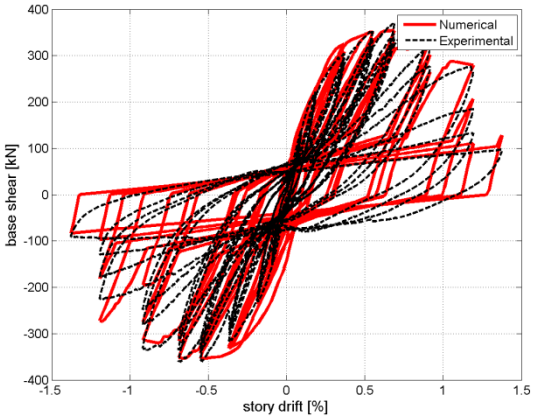

(c)

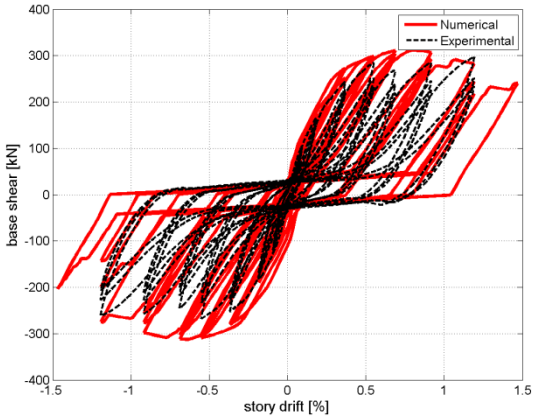

(d)

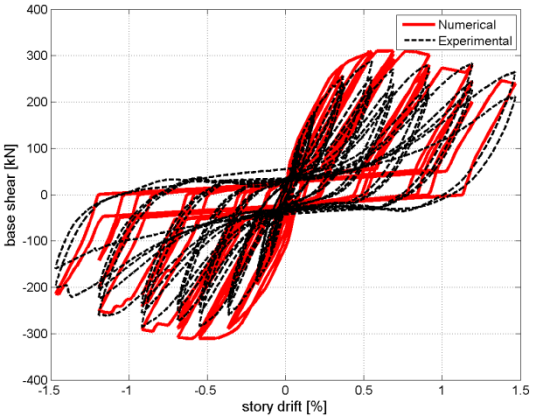

(e)

Figure 8.16: Comparison between the numerical cyclic simulations (type 2 models) and experimental response: (a) PW1; (b) PW2; (c) PW3; (d) PW4; (e) PW5.

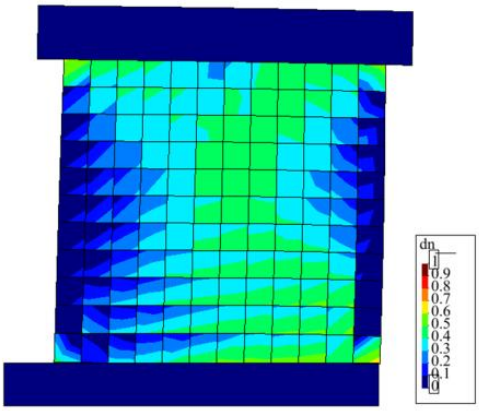

(a)

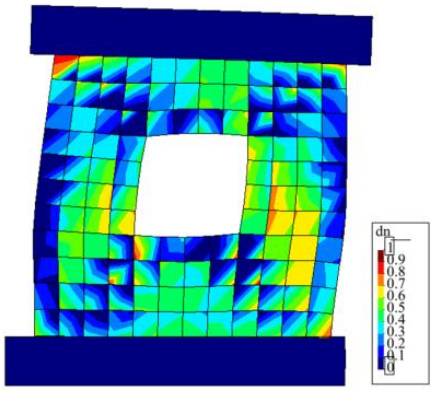

(b)

Figure 8.17: Color contour maps of the damage variable d_n at 1% drift for: (a) specimen PW1; (b) specimen PW4.

8.4.2. HSW specimen

The mesh geometry is made up four-node MITC shell elements (Dvorkin and Bathe 1984), allowing to account for the out-of-plane behavior, having dimensions of 50 cm. The slabs and the foundations are modelled as linear-elastic elements. The parameter values used for the 3D concrete Material are collected in Table 4. Steel yield strength of 450 MPa is used. It should be noted that linear-elastic out-of plane behavior is assumed. The assumption leads to a considerable reduction of the computational time (almost 10 times) and can be considered reasonable when no significant out of plane stresses are expected. Moreover, no zero-length elements are inserted between the walls and the foundations provided that no significant slips were observed during the experimental test.

Table 8.12: Parameter values for the 3D Concrete Material (HS specimen).

f_0^- [MPa]	$f_{0,2d}^-$ [MPa]	f_{ct} [MPa]	E_0 [MPa]	ν	β	A_n	B_n	A_p
15	18	0.1	28000	0.0	0.5	3.0	0.75	0.1

8.4.2.1. Cyclic analyses

The comparison between the numerical simulation and the experimental response is displayed in Figure 8.18a in terms of base shear vs. roof drift. For the sake of clearness, the last cycles are isolated and displayed in Figure 8.18b. The numerical model can reasonably simulate the main features of the experimental cyclic response such as the peak strength, stiffness and strength at different drifts, permanent (plastic) deformations during the reloading phases. Nonetheless, residual stiffness after high drifts is quite overestimated and strength degradation is not properly captured. Contour maps of the damage variable d_n are displayed in Figure 8.19. The peak of the negative damage d_n approaches to 0.85 at the corner base (the damage may correspond to initial concrete spalling) and seems to slightly underestimate the state of damage as obtained from experimental evidence. This may lead to the superior residual stiffness and less strength decay in the numerical simulations.

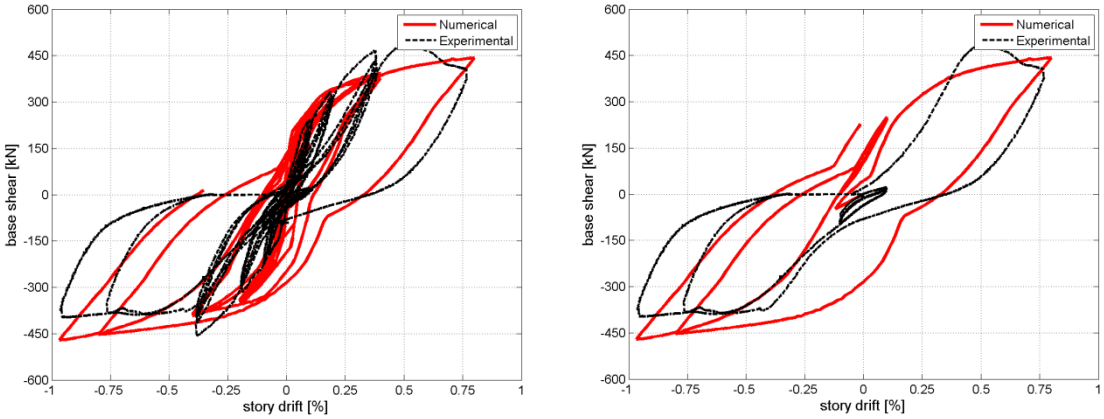

(a) (b)

Figure 8.18: Comparison between the numerical simulation and the experimental response: (a) entire cyclic response; (b)last imposed cycles.

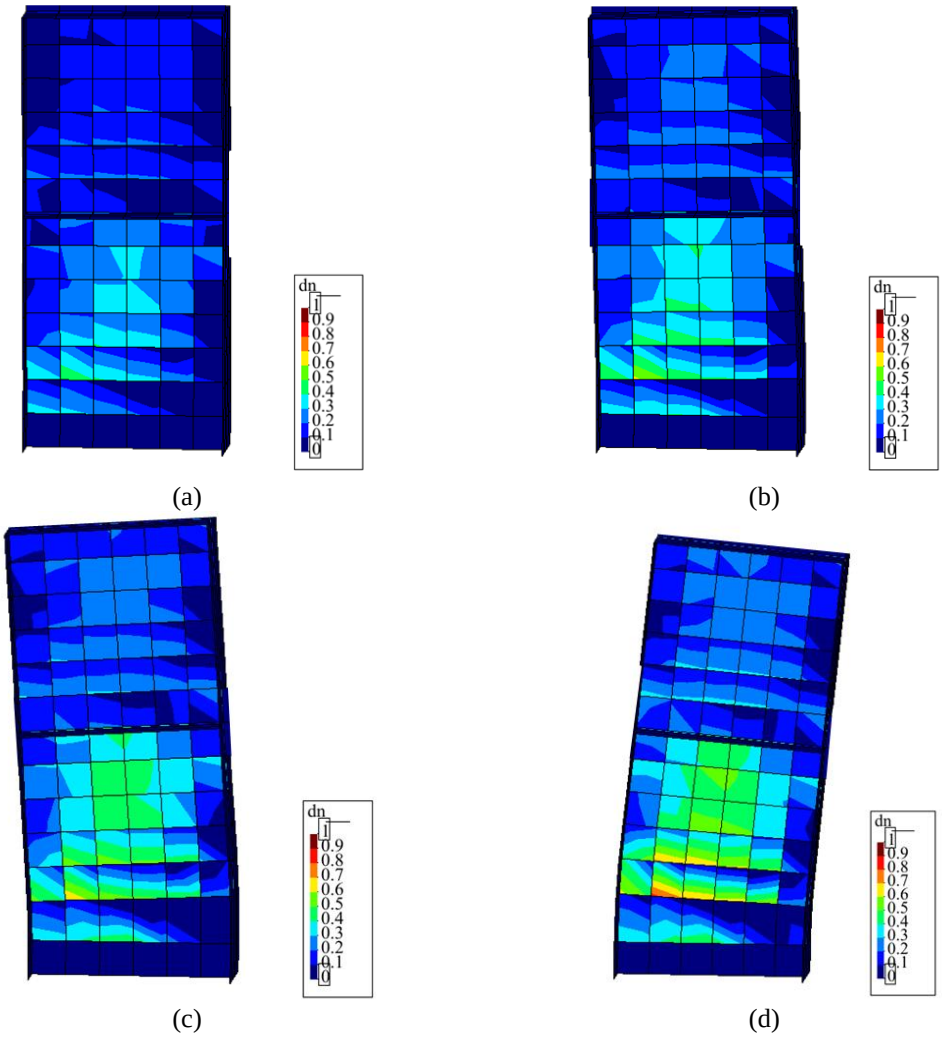

(a) (b)

(c) (d)

Figure 8.19: Color contour maps of the damage variable d_n: (a) 0.2% drift; (b) 0.4% drift; (c) 0.8% drift; (d) 1.0% drift.

The inclusion of the non-linear out-of-plane behavior of the flanges may increase the response accuracy at the prize of additional computational effort.

8.4.3. Concluding remarks

A wide experimental campaign has been developed through the last decades aimed at assessing the static and seismic response of reinforced concrete sandwich panels. Experimental tests included pseudo-static tests of both full-scale planar panels and a more complex full-scale I-shaped two-story structure. As the last step of the research work, a concrete damage model, recently proposed by some of the authors for the seismic analysis of reinforced concrete members, has been adopted in order to simulate the results of the experimental tests with the purpose of investigate the suitability of the model for the design of PSP structures under earthquake actions.

Based on the results of the numerical simulations the following conclusion can be drawn:

- The concrete damage model appears suitable for the seismic analyses of PSPs structures.
- The numerical models without connectors at the base (type 1 models) are not able to well reproduce the experimental cyclic response of the specimens: the wall peak strength is overestimated, while the ultimate displacement capacity is underestimated. Nonetheless, these models could be useful to evaluate the bearing capacity of the walls in the presence of connections which prevent from slips at the base.
- Results of the pushover analyses on the type 1 models indicate that the ultimate drift capacity of the tested panels is between 0.70% and 0.95%. However, additional experimental tests are necessary to validate these preliminary results.
- The connections between the wall base and the foundation largely affect the seismic response of walls and therefore have to be included in the model of the structure; the models including the connections (type 2 models) at the base

are able to well simulate the global experimental response in terms of base shear vs. story drift and the damage state.

- The connections at the base can be efficiently modelled thought simple non-linear elements as the zerolength elements available in the Opensees library once the appropriate hysteretic properties (i.e. the parameters governing the shape of the envelope response and the cyclic response) are assigned. Additional experimental results are necessary in order to further asses these parameters.

8.5. AN INSIGTH INTO THE 3D CONCRETE MATERIAL MODEL

The present section provides further insight into the 3D Concrete Material model. First, the response of a single plane concrete membrane element under different stress states is investigated with the purpose of underlining the capabilities and limitations of the model and of providing recommendations for the selection of the numerical values of the parameters. Then, specific aspects related to modelling of an entire RC wall (the same of section 7.3) are discussed with reference to the planar walls analysed in section 7.3.

8.5.1. Behavior in compression

8.5.1.1. Uniaxial response

The numerical response under cyclic uniaxial compression is represented in Figure 8.20 and compared with the experimental results from Sinha *et al.* 1964. The model parameters which are able to fit the experimental response are: A_n=6.0; B_n=0.75; β=0.6; $f_0^- = 0.6 f_c^{'}$ ($f_c^{'}$ being the peak experimental strength). When the initial elastic limit is passed, the plastic strain and the damage parameter increase. Clearly, the hysteresis of the reloading loop cannot be simulated by the model provided that the unloading process is assumed to be elastic.

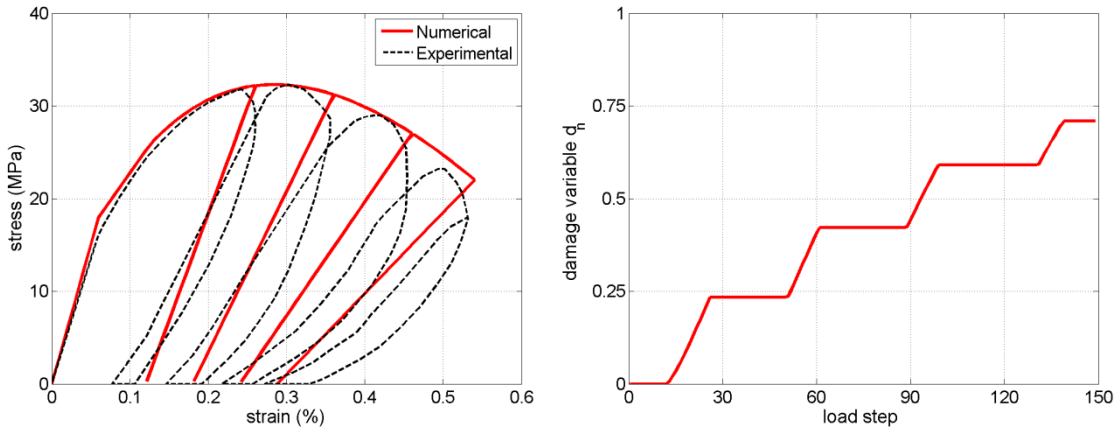

(a) (b)

Figure 8.20: Stress-strain response (a) and damage evolution under uniaxial compression(b).

The progression of the damage variable d_n is displayed in Figure 8.20. It can be noted that for this specific case the negative damage parameter is around 0.2 when the compressive peak strength is achieved. After a strength decay of about 25%, the damage parameter approaches 0.7. A value of d_n equal to 1.0 implies that the strength and stiffness of the material are completely lost. It should be underlined that the damage variable d_n monotonically increases since it depends on the maximum recorded damage threshold. This implies that the damage variable remains constant during an unloading/reloading cycle until the maximum effective stress is exceeded again.

8.5.1.2. Confinement effect

The 3D Concrete Material model is not able to directly account for the effect of the confinement due to the presence of transversal response (note that in a solid element the model would be able to capture the confinement effect). Nevertheless, as well known, the confinement plays a significant rule in the response of reinforced concrete structures. In this study, the effects due to the confinement on the material strength and ductility has been accounted based on the well-known confinement model proposed by Kent and Park 1971 by adjusting the values of parameters f_0^-, $f_{0,2d}^-$ and A_n . The following procedure is adopted: (i) the constitutive laws for the unconfined material are obtained according to the results of the experimental tests. (ii) the stress-strain relation for the confined concrete is estimated using the Kent and Park model. (iii) the model

parameters f_0^-, $f_{0,2d}^-$ and A_n are adjusted (with a fitting procedure) in order to match the Kent and Park 1971 stress-strain relationship.Table 8.13 gives the numerical values of A_n and k (k is the parameter of the Kent and Park model which multiplies the compressive strength in order to obtain f_{01d}) for transversal reinforcement ratios between 0.2% and 2.0%. For the sake of clearness, Figure 8.21 compares the stress-strain relations as suggested by Park and Kent 1971 with the corresponding one as obtained from the proposed model, for two specific values of transversal reinforcement ratios. Linear interpolation of the values of Table 8.13 is admitted for reinforcement ratios in the range of 0.2 to 2.0% (Figure 8.22).

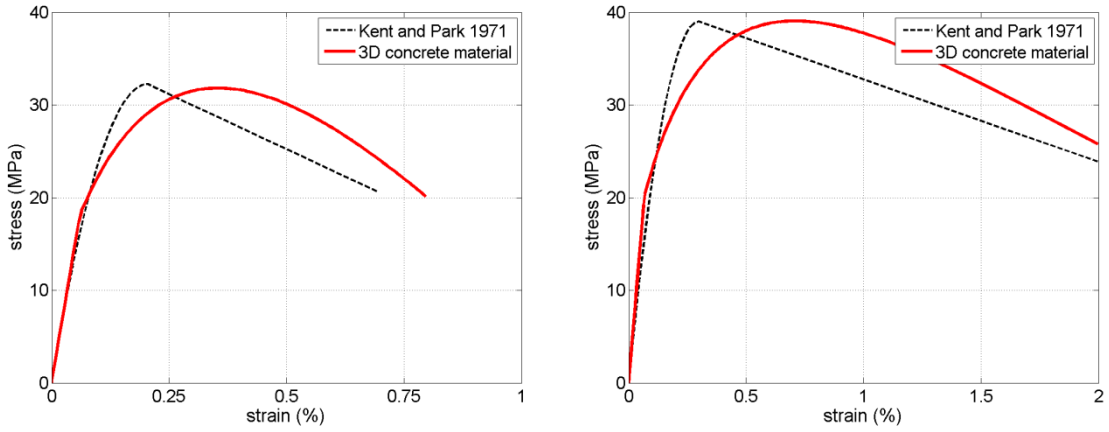

(a) (b)

Figure 8.21: Comparison of 3D concrete material model with uniaxial Kent and Park model: (a) ρ_t =0.2%; (b) ρ_t =2.0%.

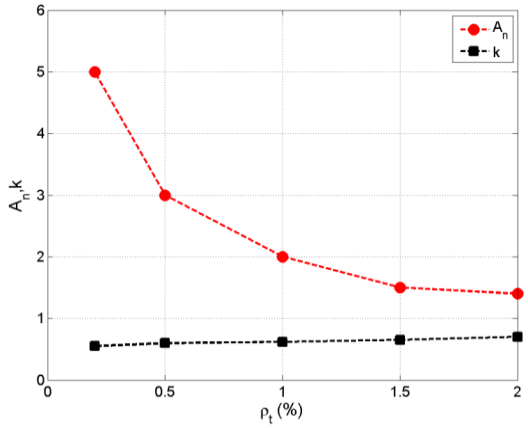

Figure 8.22: A_n and k vs. ρ_t.

Table 8.13: A_n and k for different transversal reinforcement ratio.

ρ_t [%]	A_n	K
0.2	5.0	0.55
0.5	3.0	0.60
1.0	2.0	0.62
1.5	1.5	0.65
2.0	1.4	0.7

8.5.1.3. Biaxial response

Figure 8.23 and Figure 8.24 display the numerical response for different states of biaxial compression. The following parameter values have been adopted for the simulations: A_n=2.0; B_n=0.75; β=0.6; f_0^-=0.6 $f_c^{'}$; f_0^-=1.2 $f_{0,2d}^-$. From Figure 8.23 it appears that for the case of biaxial isotropic compression the peak strength increases by 20% with respect to the case of uniaxial compression. At the same time the ductility decreases. This is consistent with the response of concrete under biaxial isotropic compression (Kupfer 1969). The progression of the damage variable d_n is also displayed in Figure 8.23. The damage variable d_n initially grows faster than the corresponding ones for uniaxial compression. After the peak strength is reached, the two damage curves grow at the same rate. The other curves of Figure 8.23 and Figure 8.24 (blue curves) represent the stress-strain response under biaxial compression for of a constant compression in one direction. It can be noted that: (a) as the constant compression increases, the peak strength also increases. (b) as the constant compression increases the ductility decreases. Moreover, the evolution of the damage in compression is the same as for the case of uniaxial compression. Figure 8.24 shows the numerical cyclic response for different cases of biaxial compression. Observations similar to those given for the monotonic response arise.

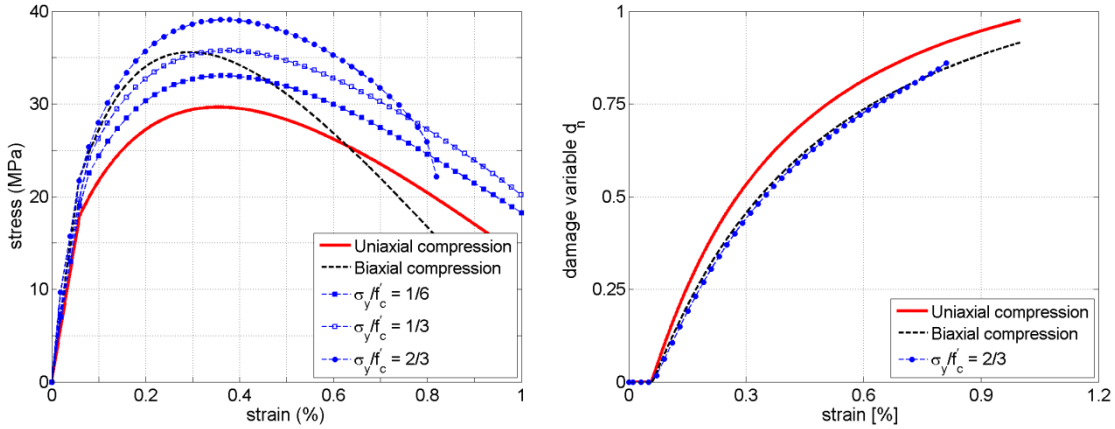

(a) (b)

Figure 8.23: Monotonic stress-strain response (a) and damage evolution (b) under uniaxial and biaxial compression.

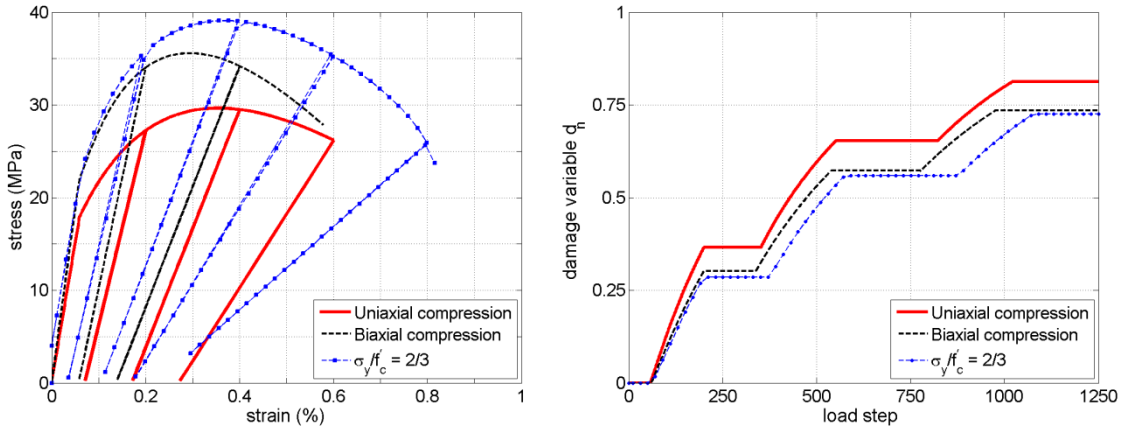

(a) (b)

Figure 8.24: Cyclic stress-strain response (a) and damage evolution (b) under uniaxial and biaxial compression.

8.5.2. Behavior in tension

8.5.2.1. Uniaxial response

The numerical response under cyclic uniaxial tension is represented in Figure 8.25 and compared with the experimental results from Gopalaratnam and Shah 1985. The model parameters which are able to fit the experimental response are: A_p=0.06; β=0.6.

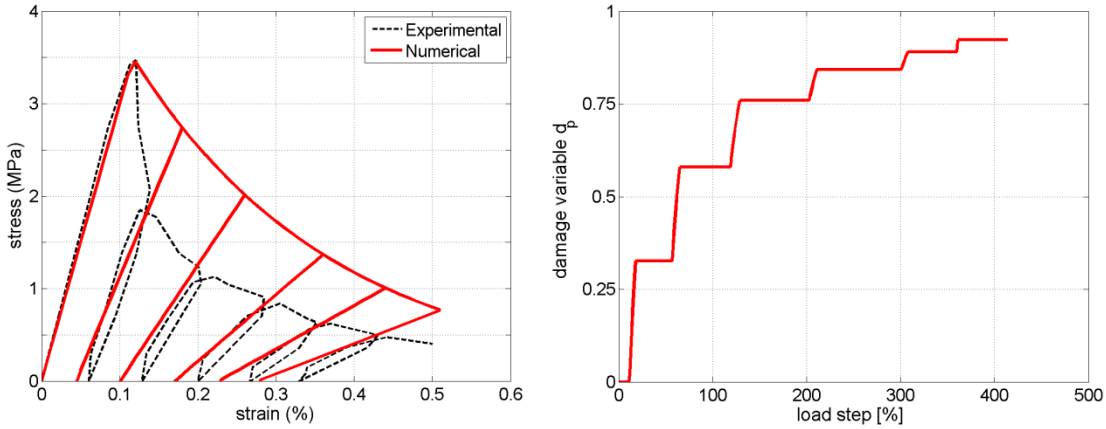

(a) (b)

Figure 8.25: Cyclic stress-strain response (a) and damage parameter evolution under uniaxial tension (b).

It can be noted that the model is capable to capture the softening response after that the tensile strength is reached. Also the stiffness degradation is well captured in an average sense. Clearly, as already observed for the case of the cyclic compression, the hysteretic loops of the unloading/reloading phase cannot be simulated by the present model.

Attention should be focused on the residual strain after complete unloading: they consistently increase even for relatively high strain and very low residual tensile concrete strength. The numerical model can capture very effectively this effect through the plasticity extended also for tensile stresses. The residual strains in tension are quite important because they affect crack closure state at loading reversals and they become particularly evident for cyclic shear tests of reinforced concrete membranes.

On the contrary, the gap between the experimental curve and the numerical one immediately after the peak strength does not preclude the effectiveness of the model for the purposes of the present work because of two reasons: the difference of the two curves is relatively insignificant in terms of dissipated energy having the concrete material a very low tensile peak strength compared to the compressive one; the post crack behavior for reinforced concrete elements subjected to tension is characterized by the steel response and by the narrow tension stiffening effect.

The evolution of the damage variable d_p is also shown in Figure 8.25. The damage parameter increases drastically at the beginning of the softening branch and then it approaches the unit asymptotically since the depletion of the fracture energy takes place at strains much larger than the elastic limit.

8.5.2.2. Tension stiffening effects

As well known, the analyses of reinforced and prestressed concrete structures based on a smeared crack approach generally include a tension stiffening relationship to estimate the average post-cracking concrete response. Many such equations have been developed over the years showing significant differences between each other (see Bentz 2005). A simple way to include the tension stiffening effect in the 3D concrete material model is to adjust the parameter A_p in order to match the desired tension-stiffening equations. In this study the formulation introduced by Bentz 2005 is chosen because it explicitly accounts for area reinforcement through the M parameter, defined as the ratio between the area of concrete participating in tension stiffening and the bar diameter. Figure 8.26 provides the comparison between the formulation proposed by Bentz 2005 and the response of the present model for three different amount of reinforcement (corresponding to M between 50 and 500). A_p decreases almost linearly as M increase.

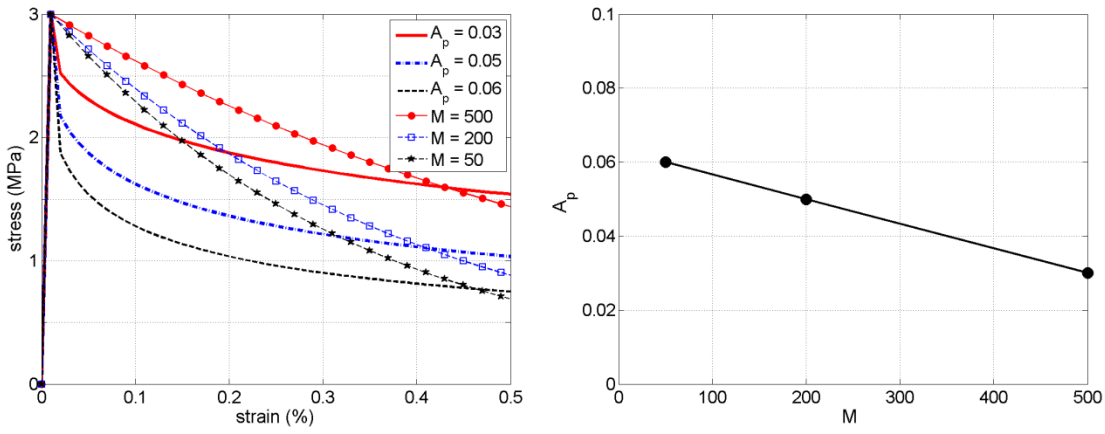

(a) (b)

Figure 8.26: (a) tension stiffening for different M (and corresponding Ap) values ; (b) Ap vs M.

8.5.2.3. Biaxial tension and tension-compression

The numerical response for a biaxial isotropic tension stress state is represented in Figure 8.27 and compared with the response in uniaxial tension. The parameters adopted for the numerical simulations are: A_p=0.2, β=0.6. The peak strength in the case of isotropic biaxial tension is reduced and the positive damage variable grows faster with respect to the case of uniaxial tension.

Figure 8.27 and Figure 8.28 display the monotonic and cyclic responses in biaxial tension-compression for the case of a constant tension in one direction (between 1/10 f_t and 0.5 f_t).

The graphs show that the presence of tensile stresses strongly reduces the compression peak strength. Furthermore, the ductility is strongly reduced.

The progression of the damage variables is also represented in Figure 8.27. It can be noted that both positive damage and negative damage increase and that the negative damage is higher with respect to case of uniaxial compression.

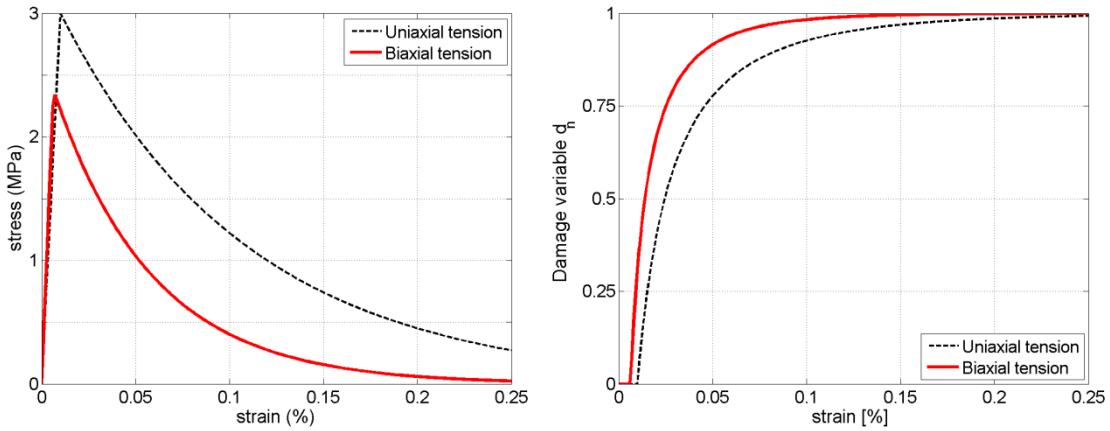

(a) (b)

Figure 8.27: Monotonic stress-strain response (a) and damage parameter evolution under uniaxial and biaxial tension(b).

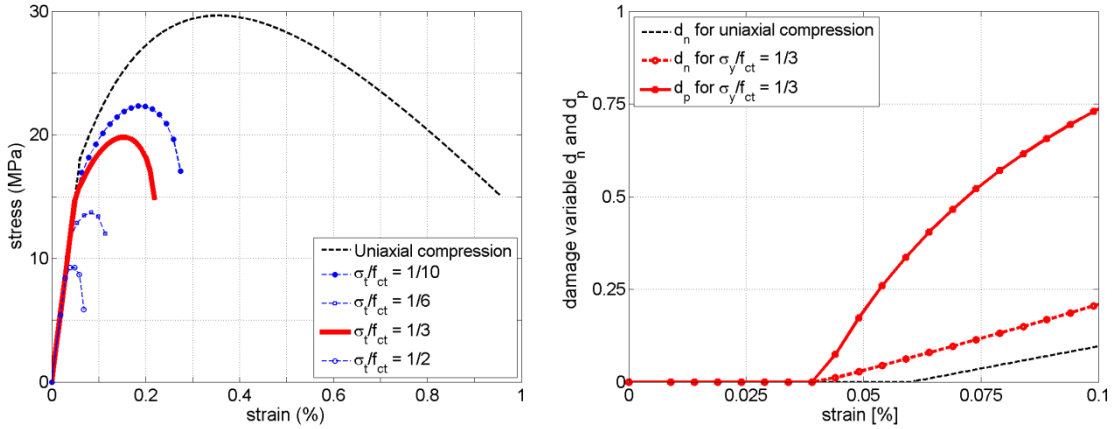

(a) (b)

Figure 8.28: Monotonic stress-strain response (a) and damage evolution under tension-compression (b).

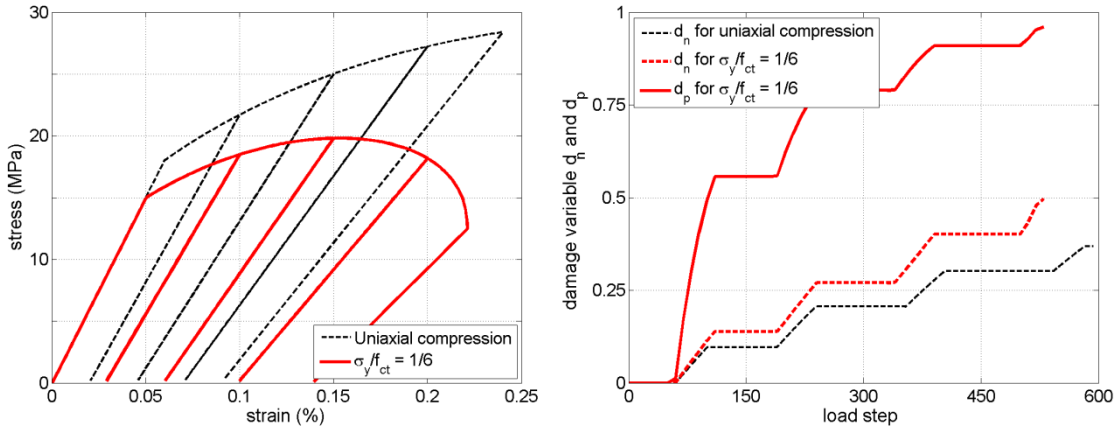

(a) (b)

Figure 8.29: Cyclic stress-strain response (a) and damage evolution under uniaxial compression and tension-compression (b).

8.5.3. Response under a more general load path

In order to highlight other features of the 3D Concrete Material model, the stress-strain response under two slightly different load paths, namely load Path A and load Path B, are displayed in Figure 8.30. The two load paths are characterized by an initial incursion into tensile field up to the initial inelastic threshold leading to damage in tension, followed by several cycles of compression-tension.

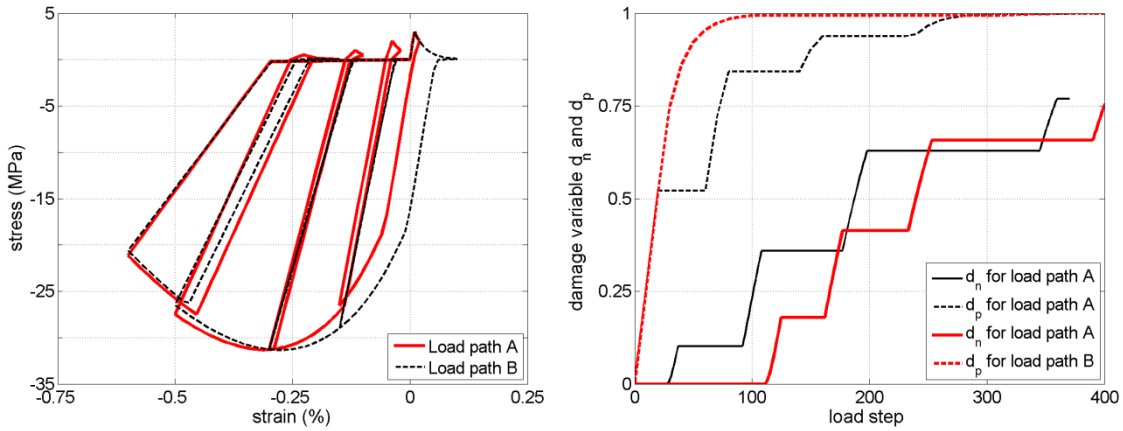

(a) (b)

Figure 8.30: Concrete stress-strain response (a) and damage evolution (b) under two different load paths.

They differ only in the first incursion into the inelastic tensile field: while in Load Path A the incursion in the tensile field is limited (the positive damage achieve a value equal to 0.55), in the Load Path B a further initial incursion in the tensile field leads to an almost complete damage in tension (the first unloading stiffness branch is almost horizontal). It can be noted the ability of the model in reproducing the softening behavior under tension as well as the subsequent stiffness recovery which takes place after the transition from tension to compression. In the compression field the model is able to reproduce the initial hardening followed by softening after the peak strength is reached. Due to the plasticity extended also in tension, in the case of accumulation of further plastic strains, the model exhibit a "shift" of the compression response which has been also observed in some experimental tests (Mansour and Hsu 20005).

8.5.4. On the response of RC members

8.5.4.1. Mesh objectivity

The sensitivity of the numerical response to the size of the mesh (generally known as the problem of mesh objectivity) has been analysed with reference to the planar RC wall (in specific specimen PW1) of section 7.3. A new model with a less refined mesh (element with double size dimension) has been developed in order to check the ability

of the characteristic length (Oliver 1989) to provide mesh objectivity. The values of the 3D concrete material parameters adopted for the new model are the same as those used for the original model (see Table 8.5), excluding parameter A_n whose values is determined in order to satisfy the equality of energy of fracture (in compression) for the two models. A value of A_n equal to 2.0 is adopted for the new model. In order to appreciate the ability of the model to provide mesh-independent results, two new models are developed:

- Model Double size mesh A (A_n=1.5 as the original model).
- Model Double size mesh B (A_n=2.0).

Figure 8.31 compares the monotonic push-over response and the cyclic response of the original model and the two new models. Both pushover response and cyclic response shows that if the material parameters are adjusted on the base of the mesh dimension, the model is able to effectively provide mesh-independent results. The contour maps of the damage variable d_n leading to DSL_6 (i.e. d_n approaches to 1.0) are displayed in Figure 8.32. It can be noted that all the three damage patterns are qualitatively similar. However, for the model Double size mesh A the DSL_6 is reached at 2.5% drift, while for the other two models it is reached at 1.6% drift. Therefore the model Double size mesh A is much more ductile and is not consistent with the experimental observations.

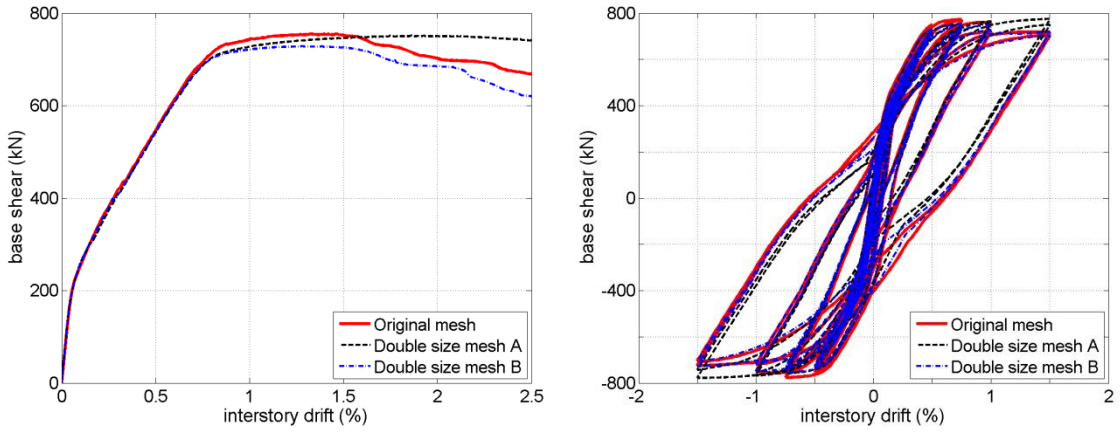

(a) (b)

Figure 8.31: Monotonic Push-over response (a) and cyclic response (b) of the two new models (Double size mesh A and Double size mesh B) compared with the original model (Original mesh).

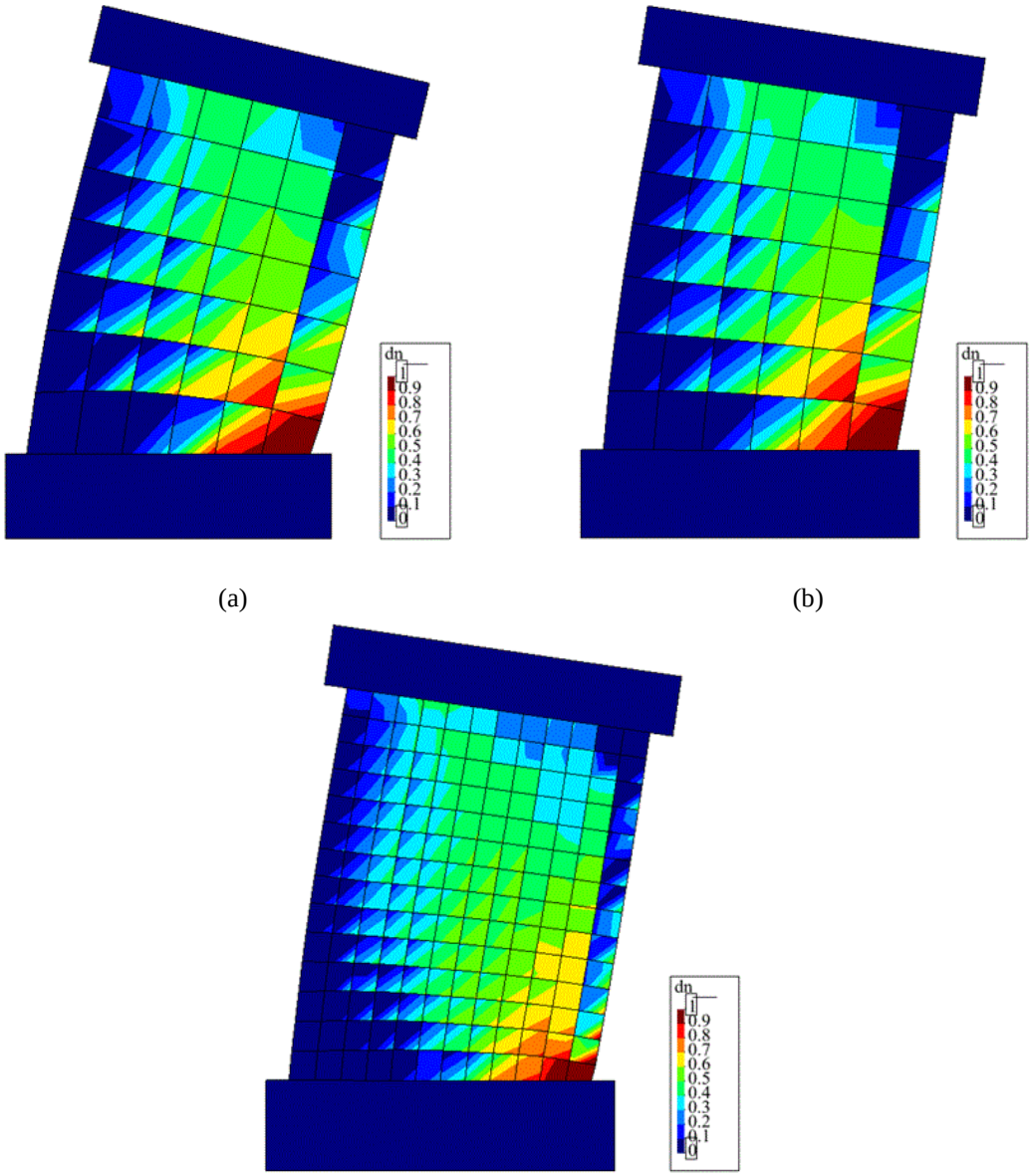

Figure 8.32: Contour maps of the damage variable dn at DSL6: (a) Double size mesh A; (b) Double size mesh B; (c) Original mesh.

8.5.4.2. On the Damage State Limits

The main point of strength of the proposed model from a practical point of view is its ability to reproduce the evolution of the concrete damage through only two scalar variables, thus allowing a graphical representation of the damage state through contour maps which are very useful as a quick tool to check the analyses results and monitor

the evolution of damage. Moreover, within the framework of performance based design, most of the current seismic design codes prescribe the achievement of multiple performance levels under different seismic design earthquakes (i.e. multiple performance objectives). Thus, the possibility of checking the reaching of code limit states through the use of contour maps appears really appealing. On the other hand, the simple representation of the contour maps of the damage variables does not allow the practitioner to a simple evaluation of the state of damage. Correlations between specific values of damage variables and physical damage mechanisms are necessary. For the case of common structures made of reinforced concrete walls the negative damage variable is the most significant variable (note that in the cases of cracks prevention or limitation is required the variable d_p plays an important rule).

In this section a simple approach to provide Damage State Limits (DSLs) for reinforced concrete walls based on the use of the contour maps of the damage variable d_n is proposed. Values of the negative damage d_n are correlated to the local stress-strain responses of concrete and steel. In this study, the following six DSLs are introduced:

- DSL_1. At this damage level the longitudinal rebars approach to the yielding and therefore can be considered as the "yielding point";
- DSL_2. At this level the concrete approaches its peak strength;
- DSL_3. At this level the concrete strength starts to decay and initial spallling could be observed;
- DSL_4. At this level the concrete residual strength is approximately equal to 0.8 the peak strength; spalling could be observed.
- DSL_5. At this level the concrete residual strength is approximately equal to 0.1 the peak strength; concrete approaches crushing;
- DSL_6. At this level the concrete has no residual strength. Typically also the rebars may fail due to buckling (or due to low-cycle fatigue in the case of cyclic loads).

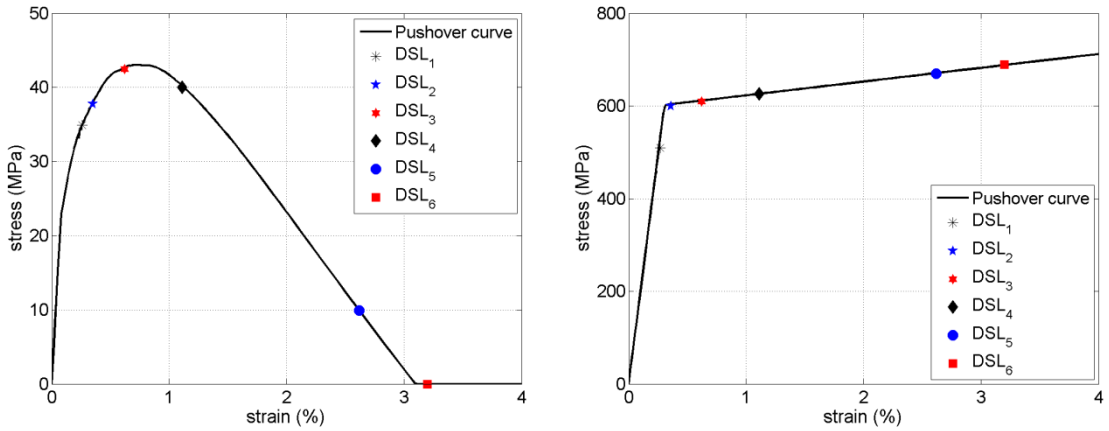

Figure 8.33: (a) DSLs superimposed to the concrete stress-strain response at the base of the boundary element; (b) DSLs superimposed to the steel longitudinal reinforcement stress-strain response at the base of the boundary element.

It has to be noted that the values of the damage variable leading to each DSLs are in general dependent on geometrical aspects, reinforcement layouts, materials mechanical properties. Values of d_n leading to each DSL for the studied RC walls are collected in Table 8.14.

Table 8.14: Values of damage variable d_n leading to each DSL.

DSL	1	2	3	4	5	6
d_n	0.6	0.7	0.8	0.9	0.95	1.0

A more general and rigorous approach to obtain a global damage index (in a integral form) is actually under developments based on the approach by Scotta et al. 2009 proposed for beam elements.

8.6. CONCLUSIONS

In this chapter a 3D Concrete Material model has been used to simulate the seismic response of RC shear walls. The model has been developed by Tesser (University of Padua) and his co-workers (Tesser *et al.* 2011) and actually is not still completely validated. For this reason before applying the model for the simulation of the

experimental tests on the RC sandwich panel walls introduced in chapter 5, numerical simulations of conventional RC shear walls has been conducted. Results show that the model allows to accurately simulate the cyclic response of RC shear walls. Then the model has been used to simulate the cyclic tests performed on the sandwich walls. It has been pointed out that the introduction of additional elements to simulate the sliding at the base of the panels has been necessary to appropriately reproduce the hysteretic response of the panel. The results highlights that special attention has to be devoted in the design of the connections at the base provided that they play a significant rule in the seismic response of the studied RC sandwich wall.

9. The seismic design of reinforced concrete sandwich squat walls

9.1. INTRODUCTION

The actual Italian building code (NTC08) does not provide specific design provisions for the seismic design of reinforced concrete sandwich walls. Recommendations are given to for the seismic design of RC shear walls. First of all, the recommended behavior factor q (in the CDB class of ductility) is around 3 for uncoupled wall structures and around 3-4 for coupled shear wall structures.

Modifications to the actions (as obtained from linear analyses) to be applied along the height of the wall are suggested in order to account for the shear-flexural interaction. Shear strength can be estimate based on classical strut and tie mechanism, i.e. following the approach for slender elements. However, it is explicitly recommended to account for the potential of sliding shear mechanisms. Moreover special attention should be devoted in order to prevent from brittle sliding shear failure at the connection between consecutive vertical walls.

In this chapter, which concludes the part B of the thesis, considerations for the seismic design of the studied reinforced concrete sandwich walls are provided.

9.2. ON THE MODELLING OF REINFORCED CONCRETE SADWICH SQUAT WALLS

The results of experimental tests and numerical simulations presented in the Part B of the thesis showed that the studied reinforced concrete squat sandwich walls exhibit a seismic behavior similar to that of conventional reinforced concrete shear walls designed with modern seismic details.

First of all, in the case of simple linear analyses a cracked inertia equal to 0.15 of the gross section inertia should be adopted to account for the sudden section partialization. A behavior factors equal to 4.0 (the value is conservative) can be adopted. The suggestions are based on both experimental results and numerical simulations.

In chapter 7 it has shown that conventional shear theories for reinforced concrete shear panels (MCFT and RA-STM) are able to reasonably estimate the shear strength of the full panels. If appropriate material constitutive equations are introduced (RCFT) the whole shear envelope response can be well reproduced. It has to be noted that the shotcrete of the tested walls exhibited a sudden degradation after that the peak tensile strength is reached, thus its contribution to the shear strength of the panel may be ignored for design purposes. A design simple formulation for the evaluation of the shear strength has been proposed. The formula can be used in the case of simple strength-based design. In the case of more complex seismic design (e.g. pushover analyses) the adjusted Refined Compression Field theory can be used to obtain the complete non-linear backbone curve representative of the shear behavior of the panel.

In chapter 8 it has shown that the continuum damage approach for conventional reinforced concrete elements can be successfully used to accurately reproduce the hysteretic behavior of the studied panels. The approach allows to well reproduce the damage progression and can be used when nonlinear time history analyses are required. Moreover, it has been noted that the connection at the base may have a significant influence on the seismic behavior of the walls and they have to be designed in an appropriate way. In more detail, a prior yielding of the connectors at the base may induce some sliding at the base which may prevent from large wall damages and therefore increase the ductility of the system. Details have to be included in order to hallow for the sliding at the base.

The results obtained through the numerical analyses also allowed to introduce damage limit states (in terms of interstorey drift).

9.2.1. Design shear strength and damage state limits

In this sections the design formula for the studied panels has obtained from the results of the experimental tests and numerical simulations presented in the chapters 7 and 8 are here summarized. The results have been already reported in the previous chapters but they are here summarized for the sake of clearness.

The design shear strength of a full panel is given by the following relations, based on the continuum mechanic approach and on the experimental evidence of negligible concrete contribution in tension:

$$V_d = \frac{L}{s} A_s f_{yd} \sqrt{1+\upsilon/\rho_m} \qquad \textbf{(9.1)}$$

Where A_s is area of the cross section of the mesh grid, L is the length of the panel, s is the size of the mesh grid, f_{yd} is the steel design stress ($f_{yd} = f_{yk}/1.15$), v is the non-dimensional parameter defined as ($\upsilon = N/Ltf_{cd}$), N is the axial load applied to the panel, t is the thickness of the panel, f_{cd} is the concrete design strength ($f_{cd} = f_{ck}/1.5$) and ρ_m is the mechanical reinforcement ratio ($\rho_m = A_s \cdot f_{yd} / (t \cdot s \cdot f_{cd})$). Note that the equation is valid for a square mesh grid.

Damage state limits were obtained from both experimental tests and numerical simulations according to the continuum damage approach. They are expressed in terms of intersory drift. Table 9.1 reports the values (conservative) of the DSLs which can be assumed as the code Immediate Occupancy (IO), Occupancy (O), Life Safety (LS), and Near Collapse (NC) limit states for the case of base connections allowing sliding at the base.

If the base connections do not allow for the sliding at the base the results of numerical analyses indicate a less ductile behavior. In this case the values collected in Table 9.2 appear more reasonable. Note that the values are not yet supported by experimental verification and therefore less reliable of the ones supported by experimental results.

Table 9.1: Values of drifts at each DLS.

d_n	IO	O	LS	NC
	0.15%	0.20%	1.0%	1.3-1.4%

Table 9.2. Values of drifts at each DLS.

d_n	IO	O	LS	NC
PW1	0.15%	0.20%	0.85%	1.0%

9.3. CONCLUSIONS

In the present chapter code-like design recommendations for the seismic design of the reinforced concrete sandwich panels infills studied in the part B of the thesis are given. They can be summarized as follows:

- The studied panels are characterized by a seismic response similar to that of conventional reinforced concrete shear walls.
- The proposed constitutive equations for the shotcrete in tension and for the embedded bars allows the Refined Compression Field theory to well reproduce the envelop response of the panels.
- A simple design equation for the evaluation of the shear strength, based on the continuum mechanic approach and on experimental evidence, is proposed.
- A damage model developed for seismic analysis of conventional reinforced concrete member has been successfully applied to reproduce the hysteretic experimental response of the wall.
- Damage state limits for the seismic design of the wall, based on the results of the experimental tests and numerical simulations, are given.

10. Conclusions and future developments

The study presented in this dissertation is focused on the analysis of the seismic response of two-dimensional squat elements and their effects to the behavior of building structures. Part A has been devoted to unreinforced masonry infills and in detail to the first developments toward a seismic-resistant unreinforced masonry infill system of superior seismic performances. Part B has been devoted to a specific reinforced concrete sandwich wall system. Summary and detailed discussions have been taken up at the end of the relevant chapters. The purpose of this chapter is to recapitulate the main findings, and to suggest some further research directions.

10.1. MAIN CONCLUSIONS OF PART A

Part A begins with a comprehensive review of modelling techniques and code provisions for infilled frame structures. Then state-of-the-practice techniques are applied for a real case to test the ability of actual modeling techniques to reproduce observed behaviors. The first developments toward a seismic-resistant unreinforced masonry infill system are presented. Design recommendations for the seismic design of the seismic-resistant masonry infills are finally provided. In summary, the following conclusions are drawn:

- The nonlinear equivalent strut model appears appropriate for the seismic analyses of infilled frame structures and the actual best candidate to be suggested for code-like analyses.
- The preliminary results of the experimental tests on the single innovative materials (clay bricks with alumina-based nanoparticles and additivated mortar) show that the masonry assembly could potentially be characterized by superior seismic performances.

- Design recommendations for the seismic design of the innovative infill are proposed. In detail the use of the nonlinear equivalent strut model is suggested. Infill expected strengths have been identified through the results of the preliminary experimental tests.

10.2. MAIN CONCLUSIONS OF PART B

Part B is focused on the study of the seismic behavior of a specific reinforced concrete sandwich panel system. First, the results of in-plane psuudostatic cyclic tests are described. Conventional compression field theories are then applied to study the monotonic shear response of the panels, while the panel hysteretic response is studied according to a continuum damage model. Design recommendations for the seismic design of the studied reinforced concrete sandwich walls are provided. In summary, the following conclusions are drawn:

- The studied RC sandwich squat walls are characterized by seismic performances (in terms of strength and dissipation properties) comparable to that of conventional reinforced concrete shear walls of similar geometrical (aspect ratio) and mechanical (reinforcement ratios) properties.

- Refinements to the compression field theories have been introduced in order to better simulate the monotonic envelope response of the panels. The refinements deal with the introduction of a new constitutive model for the shotcrete in tension and for the embedded bars. A simple formula for the estimation of the shear strength is proposed.

- The hysteretic response of the walls has been studied through a continuum damage model. Damage state limits have been identified.

- Design recommendations for the seismic design of the innovative infill are proposed. In detail: (i) cracked stiffness and behavior factors to be used for linear analyses; (ii) design equations for the shear strength; (iii) damage state limits to be used for nonlinear analyses.

10.3. FUTURE DEVELOPEMENTS

A list of future developments releted to the research works presented in this thesis are here summarized.

In the Part A of the thesis, presenting the first development toward a seismic-resistant infill system, only preliminary results have been presented. Therefore a number of issues are still to be addressed:

- The complete mechanical characterization of the single components (masonry bricks and additivated mortar). The first formulation of the "nano-additivated" clay brick mixture should be refined by further investigation on the influence of others alumina-based nanoparticles.

- The experimental characterization of the innovative masonry assembly. In more details:

    - triplet tests and diagonal compression tests will be carried out on small assemblies. These experimental tests should allow to evaluate the expected (design) shear strength of the masonry.

    - Cyclic tests on full-scale masonry infills. These tests will be useful in order to evaluate the actual mechanisms of failure of the innovative infills and therefore to verify the effectiveness of the design strength formula. Moreover the experimental tests will also allow to evaluate ultimate deformation capacities.

As far as Part B of the thesis, dealing with the seismic response of specific RC sandwich panels, is concerned, additional studies related to the damage model used to develop the numerical simulations should be carried out:

- the 3D damage model could be used in order to simulate recent shake table tests performed on a full-scale three-storey building made entirely of RC sandwich panels. The simulations could be useful in order to:

  - check the ability of the model in reproducing the response of more complex 3D structures.

  - try to better interprete some local responses obtained from the experimental tests (i.e. comparisons of stress.-strain responses at critical locations, damage evolution at critical locations, …)

- Additional parameteric analyses could be developed (at the material level) to further evaluate the effect of the single model parameters in order to provide a guide to easly select their values. This phase should be of fundamental importance to allow practical engineers to use the model for design purposes.

Appendix 1: Database of experimental tests on masonry specimens from the scientific literature.

Table A1.1: Bricks database.

Author/Product	Brick type	Brick geometry[cm]	strength					Elastic modulus	Poisson ratio
			Compression [MPa]		Tensile [MPa]			[MPa]	
			perpendicular	parallel	indirect	shear	direct		
Braga et al.	full clay	25x5.5x12					4.13		
Jukes and Riddington	full clay	21.5x6.5x10.25							
Jukes and Riddington	hallow clay	21.5x6.5x10.25		67.9					
Jukes and Riddington	hallow clay	21.5x6.5x10.25		18.3					
Meli	hallow clay			19.62					
Meli	hallow clay			21.09					
Meli	hallow clay			14.71					
Laner	hallow clay	40x20x20		27.2					
Laner	hallow clay	25x12x12		59					
Laner	hallow clay	30x15x25		33.3					
Page	concrete brick	39x19x14		32					
Unipor	full clay	36.5x23.8x24.7		2.3					
Porotherm	full clay	38x24x19.9	2						

Author/Product	Brick type	Brick geometry[cm]	strength					Elastic modulus	Poisson ratio
			Compression [MPa]		Tensile [MPa]			[MPa]	
			perpendicular	parallel	indirect	shear	direct		
Perlater	full clay	38x25x19	1.5	6					
Thermo plan	full clay	36.5x24.7x24.9		7.5					
Gabor et al.	full clay							13000	0.2
Atkinson		19.3x9.2x5.5		67.8	3.14			14701	0.22
Capozucca et al.	hallow clay	30x24x19		21					
Capozucca et al.	hallow clay	30x27x19		24					
MURATURA PORTANTE IN ZONA SISMICA, andil	hallow clay		6.81	20.42					
MURATURA PORTANTE IN ZONA SISMICA, andil	hallow clay		9.1	20.96					
MURATURA PORTANTE IN ZONA SISMICA, andil	hallow clay		7.95	20.43					
Da Porto et al.	hallow clay	24.9x29.8x24.1	5.94					3547	0.21
Da Porto et al.	hallow clay	24.4x29.1x25.2		18.26				7368	0.38
Valluzzi et al.	hallow clay	24.5x30.2x22.8		17.3					
Valluzzi et al.	hallow clay	24.5x29.3x19.7		16.1					
Valluzzi et al.	hallow clay	25.4x30x25		17.2					
Beconcini et al.	hallow clay	30x25x25		10		0.68			

Table A1.2: Mortar database.

Authors/product	**Mortar type**	**specimen**	**strength**				**Elastic modulus**	**Poisson ratio**
			Compression [MPa]	Tensile [MPa]			[MPa]	
				brasilian	direct	flexure		
Cantalupi	aerea				0.2			
Cantalupi	idraulica				2			
Cantalupi	cementizia				2.2			
Clericetti	aerea				0.2			
Clericetti	idraulica				0.6			
Clericetti	cementizia				1.5			
Russo	aerea con calce				0.2			
Russo	aerea con calce+pozzolanica				0.8			
Russo	cementizia				1.3			
Fabbrichesi	malta a presa lenta				2.2			
Fabbrichesi	malta a presa rapida				1			
Marcari	pozzolanica		4.5		1.57			
Vermeltfoort	preconfezionata		23		5.5			
Anzani et al.	idraulica		9		1.9			
Mayorca and Meguro	cementizia		8.2		0.7		8600	0.2
Valluzzi	idraulica		1.58	0.11	0	0.63	2590	
Capozucca			24.5		4.6	0		
Bernardini et al.	pozzolanica					1.1		
Tubi et al.	bastarda					2.67		

Augenti and Romano	pozzolanica					0	1000	
Ferrier et al.	cementizia					0	6000	0.2
Atkinson		cilindro	4.7	0.76		0	1050	0.06
Authors/product	**Mortar type**	**specimen**	**strength**				**Elastic modulus**	**Poisson ratio**
Atkinson		cubo	9.22	0.94		0	2109	0.05
Capozucca et al.	M1 as per UNI EN 1015		24.5			4.6		
MURATURA PORTANTE IN ZONA SISMICA, andil		UNI EN 1015	14			4	8500	
Da Porto et al.		cubo	9.22			4.28	9984	0.1
Valluzzi et al.	calce cemento M2	cubo	8.2			3.02	8809	0.28
Valluzzi et al.	fibrorinforzata	cubo	22			5	7000	0.14 – 0.21
Laboratorio prove materiali Pietro Pisa	malta indurita	4x4x15.8 cm	62			5.8		

Table A1.3: Masonry database.

Authors/product	**Compression strength [MPa]**	**Elastic modulus [MPa]**	**Shear**			
			Diagonal compression [MPa]	Triplets [MPa]	Friction coefficient	Poisson
Borri et al.	0.85	2000	0.2			
Corradi et al.			0.05			
Brignola et al.			0.05			
Brignola et al.			0.185			
Brignola et al.			0.318			
Brignola et al.			0.411			
Da Porto et al.	6.95	4424	0.206			0.45
Da Porto et al.	5.5	4300	0.35			0.25 - 0.36
Capozucca et al.			0.95			
Capozzucca et al.			0.39			
Beconcini et al.	2.9	6000	0.2			
Da Porto et al.	5.2	6500	0.15	0.4	0.77 - 1.9	
Da Porto et al.	4	5000	0.7	0.2	0.7 - 1.61	
Rotunno.			0.1	0.044		
Rotunno.			0.12	0.531		
Rotunno.			0.2	0.212		

Appendix 2: The first experimental tests on the innovative masonry infills

Table A2.1: Compression tests on standard specimens (S).

Specimen	$F_{rupture}$	f_t	a_1	a_2	a mean	h_1	h_2	h mean	w_1	w_2	w mean	Area*	Weight
	[daN]	[MPa]	[mm]	[mm]	[mm]	[mm]	[mm]	[mm]	[mm]	[mm]	[mm]	[mm^2]	[g]
S1	4420	53.35	29.12	29.23	29.175	27.77	27.79	27.78	28.42	28.37	28.40	828.4	38.4
S2	4625	55.29	29.27	28.88	29.075	27.94	27.8	27.87	28.74	28.8	28.77	836.5	38.3
S3	4350	52.81	28.55	29.15	28.85	28.01	27.89	27.95	28.68	28.42	28.55	823.7	37.9
S4	6478	78.60	29.12	29.03	29.075	27.76	27.8	27.78	28.35	28.34	28.35	824.1	38.4
S5	4275	51.08	29.31	29.17	29.24	27.69	27.68	27.69	28.7	28.54	28.62	836.8	38.1
S6	5567	66.81	29.34	29.07	29.205	27.43	27.53	27.48	28.55	28.51	28.53	833.2	37.7
S7	6912	83.25	29.32	29.26	29.29	27.89	27.82	27.86	28.37	28.32	28.35	830.2	38.8
S8	4305	51.58	29.11	29.17	29.14	27.89	27.87	27.88	28.78	28.5	28.64	834.6	38.4
S9	5018	60.21	29.21	29.13	29.17	27.87	27.87	27.87	28.6	28.54	28.57	833.4	38.2
S10	4850	57.96	29.44	29.45	29.445	27.98	27.97	27.98	28.46	28.38	28.42	836.8	39.1
S11	4083	48.32	29.47	29.12	29.295	28.03	28.02	28.03	28.86	28.83	28.85	845	38.6
S12	3670	43.32	29.45	29.53	29.49	28.07	28.05	28.06	28.73	28.73	28.73	847.2	38.6

Table A2.2: Bending tests on standard specimens (S).

Specimen	**F_u**	**f_t**	**l**	**h_1**	**h_2**	**h_3**	**h mean**	**w_1**	**w_2**	**w_3**	**w mean**	**Area***	**weight**
	[daN]	**[MPa]**	**[mm]**	**[mm]**	**[mm]**	**[mm]**	**[mm]**	**[mm]**	**[mm]**	**[mm]**	**[mm]**	**[mm^2]**	**[g]**
S1	199.3	22.68	105.87	27.88	28.06	28.07	28.00	28.34	28.92	28.47	28.58	800.2	140.8
S2	211.5	24.13	106.06	28.02	27.97	27.97	27.99	28.34	28.88	28.37	28.53	798.5	140.5
S3	210	23.86	105.97	27.94	28.02	28.08	28.01	28.37	28.88	28.55	28.60	801.2	141.5
S4	238.5	27.87	105.93	27.61	27.63	27.63	27.62	28.44	28.86	28.51	28.60	790.1	140.5
S5	291.8	31.84	105.29	28.31	28.6	28.73	28.55	28.51	29.05	28.47	28.68	818.6	147.4
S6	275.3	29.63	105.05	28.61	28.66	28.89	28.72	28.42	29.17	28.58	28.72	824.9	148.1
S7	257.5	28.25	105.27	28.47	28.48	28.37	28.44	28.25	29.22	28.74	28.74	817.3	146
S8	247.5	28.45	104.99	27.62	27.84	27.95	27.80	28.38	29.39	28.32	28.70	797.9	144
S9	237.3	26.60	105.08	28.06	28.15	28.13	28.11	28.32	29.45	28.59	28.79	809.3	145.3
S10	219.8	24.83	105.14	28.04	28.05	28.04	28.04	28.3	29.31	28.51	28.71	805	145.2

Table A2.3: Compression tests on standard+ sawdust specimens (P).

Specimen	**$F_{rupture}$**	**f_t**	**a_1**	**a_2**	**a mean**	**h_1**	**h_2**	**h mean**	**w_1**	**w_2**	**w mean**	**Area***	**Weight**
	[daN]	**[MPa]**	**[mm]**	**[mm]**	**[mm]**	**[mm]**	**[mm]**	**[mm]**	**[mm]**	**[mm]**	**[mm]**	**[mm^2]**	**[g]**
P1	3015	36.32	29.05	29.25	29.15	27.96	27.99	27.98	28.24	28.72	28.48	830.2	35.1
P2	3090	36.13	29.53	29.61	29.57	28.02	28.01	28.02	28.94	28.9	28.92	855.2	36.4
P3	3965	48.10	28.91	29.11	29.01	28.03	28.03	28.03	28.51	28.32	28.42	824.3	35.4
P4	3090	37.27	29.04	29.12	29.08	28.02	28.03	28.03	28.3	28.72	28.51	829.1	35.6
P5	2993	35.41	29.3	29.17	29.235	28.01	28.02	28.02	28.91	28.91	28.91	845.2	36.5
P6	2758	33.11	29.17	29.3	29.235	28.02	28.02	28.02	28.46	28.53	28.50	833.1	35.7
P7	2750	33.22	28.91	28.32	28.615	28.02	27.97	28.00	29.33	28.53	28.93	827.8	35.4
P8	3115	36.96	29.17	29.11	29.14	29.91	27.99	28.95	29.1	28.75	28.93	842.9	36.4
P9	3585	43.47	28.87	28.95	28.91	27.89	27.96	27.93	28.52	28.53	28.53	824.7	35.4
P10	3013	36.36	29.04	29.13	29.085	28.02	28	28.01	28.76	28.22	28.49	828.6	35.4
P11	2845	34.38	28.77	28.87	28.82	27.97	27.98	27.98	28.94	28.48	28.71	827.4	35.9
P12	3820	46.20	28.98	29.02	29	27.94	27.99	27.97	28.5	28.52	28.51	826.8	35.6

Table A2.4: Bending tests on standard + sawdust specimens (P).

Specimen	**F_u [daN]**	**f_t**	**l**	**h_1**	**h_2**	**h_3**	**h mean**	**w_1**	**w_2**	**w_3**	**w mean**	**Area***	**weight**
	*****	**MPa**	**mm**	**mm**	**mm**	**mm**	**mm**	**mm**	**mm**	**mm**	**mm**	**mm^2**	**g**
P1	115.8	13.53	106.5	27.59	27.65	27.68	27.64	28.5	28.91	28.27	28.56	789.4	128.9
P2	133.3	15.17	106.57	28.02	28.04	27.88	27.98	28.51	29.03	28.34	28.63	801.0	130.1
P3	138.8	15.70	106.74	28.05	28.02	27.97	28.01	28.57	29.2	28.42	28.73	804.8	131
P4	151.8	17.09	106.63	27.85	28.07	28.17	28.03	28.63	29.32	28.54	28.83	808.1	131.8
P5	124	14.03	106.38	27.95	27.99	27.98	27.97	28.52	29.33	28.53	28.79	805.4	130.5
P6	124.8	14.18	106.53	28.02	27.97	27.96	27.98	28.41	29.23	28.32	28.65	801.8	130.2
P7	119.3	13.58	106.35	27.93	27.97	27.96	27.95	28.43	29.25	28.3	28.66	801.1	130.1
P8	93.5	10.63	106.44	27.95	27.95	28.02	27.97	28.43	29.27	28.31	28.67	802.0	130.1
P9	130.3	15.05	106.44	27.77	27.77	27.65	27.73	28.46	29.23	28.46	28.72	796.3	128.9
P10	117.5	13.20	106.56	28.01	27.95	27.98	27.98	28.41	29.29	29.29	29.00	811.3	129.9

Table A2.5: Compression tests on standard+ sawdust + nanoparticles specimens (N).

Specimen	**$F_{rupture}$**	**f_t**	**a_1**	**a_2**	**a mean**	**h_1**	**h_2**	**h mean**	**w_1**	**w_2**	**w mean**	**Area***	**Weight**
	daN	**MPa**	**mm**	**mm**	**mm**	**mm**	**mm**	**mm**	**mm**	**mm**	**mm**	**mm^2**	**g**
N1	2483	31.06	28.42	27.94	28.18	28.01	28.14	28.08	28.35	28.39	28.37	799.5	33.9
N2	2255	27.44	28.77	28.61	28.69	27.95	28	27.98	28.4	28.89	28.65	821.8	34.5
N3	2593	32.26	28.6	27.96	28.28	27.7	27.76	27.73	28.46	28.38	28.42	803.7	33.7
N4	2663	31.84	29.17	29.09	29.13	27.95	27.96	27.96	28.68	28.75	28.72	836.5	35.2
N5	2535	30.41	29.1	29.1	29.1	27.97	28.01	27.99	28.92	28.37	28.65	833.6	35.2
N6	3245	39.27	29.2	29.18	29.19	27.97	27.89	27.93	28.36	28.26	28.31	826.4	35.1
N7	2813	33.81	29.2	29.05	29.125	27.97	27.97	27.97	28.49	28.65	28.57	832.1	35.1
N8	2835	33.85	29.13	29.07	29.1	27.97	27.98	27.98	28.67	28.89	28.78	837.5	35.3
N9	3450	41.72	29.14	29.18	29.16	27.97	27.99	27.98	28.49	28.23	28.36	827.0	35.1
N10	2883	34.87	29.14	29.23	29.185	27.96	27.85	27.91	28.38	28.28	28.33	826.8	35
N11	2988	36.25	29.04	29	29.02	28.01	27.99	28.00	28.48	28.32	28.40	824.2	35
N12	3158	39.90	29.19	29.06	27.94	27.94	27.96	27.95	28.3	28.35	28.33	791.4	35

Table A2.6: Bending tests on standard+ sawdust + nanoparticles specimens (N).

Specimen	**F_u [daN]**	**f_t**	**l**	**h_1**	**h_2**	**h_3**	**h mean**	**w_1**	**w_2**	**w_3**	**w mean**	**Area***	**weight**
	*****	**MPa**	**mm**	**mm**	**mm**	**mm**	**mm**	**mm**	**mm**	**mm**	**mm**	**mm^2**	**g**
N1	127.8	14.66	105.94	27.92	27.99	28.01	27.97	28.32	28.55	28.36	28.41	794.7	127.5
N2	126.5	14.47	105.95	27.96	27.99	28	27.98	28.33	28.68	28.37	28.46	796.4	127.4
N3	105	12.09	106.55	27.84	27.95	28	27.93	28.29	28.43	28.42	28.38	792.7	127.1
N4**	10.75	1.23**	106.65	27.84	27.94	28.03	27.94	28.31	28.92	28.47	28.57	798.1	129.9
N5	126.5	14.78	105.76	27.87	27.79	27.63	27.76	28.24	28.52	28.21	28.32	786.4	128.7
N6	147.8	17.09	105.55	27.83	27.91	27.92	27.89	28.2	28.59	28.27	28.35	790.7	128.3
N7	121.8	14.30	105.61	27.77	27.72	27.63	27.71	28.23	28.35	28.29	28.29	783.8	127.2
N8	147.5	17.05	105.47	27.65	27.9	28	27.85	28.28	28.66	28.4	28.45	792.2	128.5
N9	144.8	16.72	105.97	27.78	27.9	27.98	27.89	28.25	28.66	28.26	28.39	791.7	128.8
N10	138	15.84	106.25	27.54	27.98	28.31	27.94	28.28	28.68	28.37	28.44	794.8	129.4

**not considered for the evaluation of the mean properties (premature failure)

Appendix 3: Equivalent strut equations from litterature.

Holmes 1961

$$a = 1/3 D_{\text{inf}}$$

D_{inf} diagonal length of the infill

Stafford Smith and Carter, 1969

$$a = \frac{\pi}{2\lambda_h}$$

$$\lambda_{\text{h}} = \sqrt[4]{\frac{E_{\text{inf}} t_{\text{inf}} \sin 2\theta}{4 E_c I_c H_{\text{inf}}}}$$

λ_{h} stiffness parameter [m^{-1}]

E_{inf} infill elastic modulus

I_c column moment of inertia

H_{inf} infill height

Mainstone, 1971

$$a = 0.175\left(\lambda_h h_{col}\right)^{-0.4} D_{\text{inf}} \quad \text{for} \quad 4 \le \lambda_h \le 5$$

$$a = 0.16\left(\lambda_h h_{col}\right)^{-0.3} D_{\text{inf}} \quad \text{for} \quad \lambda_h > 5$$

Liauw and Kwan, 1984

$$a = 0.95 H_{\text{inf}} \cos\theta / \sqrt{\lambda_h H_{\text{inf}}}$$

θ strut inclination

Decanni and Fantin, 1986

Two sets of equations:

1. Uncracked conditions

$$a = \left(\frac{0.748}{\lambda_h H_{\text{inf}}} + 0.085 \right) D_{\text{inf}} \quad \text{for} \quad \lambda_h \le 7.85$$

$$a = \left(\frac{0.393}{\lambda_h H_{\text{inf}}} + 0.130 \right) D_{\text{inf}} \quad \text{for} \quad \lambda_h > 7.85$$

2. Cracked conditions

$$a = \left(\frac{0.701}{\lambda_h H_{\text{inf}}} + 0.010 \right) D_{\text{inf}} \quad \text{for} \quad \lambda_h \le 7.85$$

$$a = \left(\frac{0.470}{\lambda_h H_{\text{inf}}} + 0.040 \right) D_{\text{inf}} \quad \text{for} \quad \lambda_h > 7.85$$

Moghaddam and Dowling, 1988

$$a = 1/6 D_{\text{inf}}$$

Paulay and Priesteley, 1992

$$a = 0.25 D_{\text{inf}}$$

Durrani and Luo, 1994

$$a = \gamma D_{\inf} \sin 2\theta$$

$$\gamma = 0.32\sqrt{\sin 2\theta}\left(\frac{H^4 E t_{\inf}}{m E_c I_c b}\right)^{-0.1}$$

$$m = 6\left(1 + \frac{6a\tan\left(\frac{E_b I_b H}{E_c I_c L_{\inf}}\right)}{\pi}\right)$$

γ	effective width factor
E_b	beam elastic modulus
E_c	column elastic modulus
H	interstorey heigth

Bennet et al. 1996

$$a = \frac{\pi}{C\lambda_h \cos\theta}$$

C	empirical constant based on infill damage

Al-Chaar, 2002

$$a = 0.083CD_{\inf}\left(1 + \frac{2.574}{\lambda_h H_{\inf}}\right) \quad \text{for } L_{\inf}/H_{\inf} \geq 1.5$$

$$C = -0.3905\left(\frac{L_{\inf}}{H_{\inf}}\right) + 0.7829$$

$$a = 0.1106D_{\inf}\left(1 + \frac{6.027}{\lambda_h H_{\inf}}\right) \quad \text{for } L_{\inf}/H_{\inf} = 1.0$$

Linear interpolation is required for aspect ratios between 1.0 and 1.5

Papia et al. 2003

$$a = \frac{c}{z} D_{\inf} \left(1 / \lambda^*\right)$$

$$c = 0.249 - 0.0116\nu + 0.567\nu^2$$

$$\lambda^* = \frac{E_f t_{\inf} h'}{E_f A_c} \left(\frac{h'^2}{l'^2} + \frac{1}{4} \frac{A_c l'}{A_b h'} \right)$$

E_f	elastic modulus of the frame
A_c	column cross section
A_b	beam cross section
l'	length of the frame
h'	height of frame to mid-height of beam

References

Al-Chaar, G.K., 2002. Evaluating Strength and Stiffness of Unreinforced Masonry Infill Structures, US Army Corps of Engineering.

Altin, S., Ersoy, U., Tamkut, T., 1992. Hysteretic Response of Reinforced-Concrete Infilled Frames. J. Struct. Eng.

Amato, G., Cavaleri, L., Fossetti, M., & Papia, M. (2008). Infilled frames: influence of vertical loads on the equivalent diagonal strut model. Procedings of 14th WCEE, Beijing, China. CD-ROM, Paper, 05-01.

Asteris, P., 2008. Finite element micro-modeling of infilled frames. Electron. J. Struct. Eng. 1–11.

Asteris, P.G., Antoniou, S.T., Sophianopoulos, D.S., Chrysostomou, C.Z., 2011. Mathematical Macromodeling of Infilled Frames: State of the Art. J. Struct. Eng.

Asteris, P.G., Chrysostomou, C.Z., Giannopoulos, I.P., Smyrou, E., 2011. Masonry infilled reinforced concrete frames with openings, COMPDYN 2011, III ECCOMAS Thematic Conference on Computational Methods in Structural Dynamics and Earthquake Engineering, Corfu, Greece, May 26-28, 2011.

ASCE/SEI 41 (2007) Seismic Rehabilitation of Existing Buildings, American Society of Civil Engineers, Reston, Virginia.

ASCE-ACI Committee 445 on Shear and Torsion, 1998. Recent approaches to shear design of structural concrete. J Struct Eng 124:1375–1417.

ASTM E 519-81 1981. Standard Test Method for Diagonal Tension (Shear) in Masonry Assemblages, American Society for Testing Materials.

Beck H., 1962 Contribution to the analysis of coupled shear walls. Proc J Am Concr Inst ;59:1055–70.

Bathe, K.-J., Dvorkin, E.N., 1985. Short Communication A Four-Node Plate Bending Element Based On Mindlin/Reissner Plate Theory And A Mixed Interpolation. Internarional J. Numer. Methods Eng. 21, 367–383.

Bazzurro, P., Alexander, D., Clemente, P., 2009a. The MW 6.3 Abruzzo, Italy, Earthquake of April 6, 2009. EERI Special Earthquake Report. Earthq. Eng.

Belarbi, A., Hsu, T.T.C., 1994. Constitutive laws of concrete in tension and reinforcing bars stiffened by concrete. ACI Struct. J. 91, 465–474.

Benayoune, A., Samad, A.A.A., Abang Ali, A.A., Trikha, D.N., 2007. Response of pre-cast reinforced composite sandwich panels to axial loading. Constr. Build. Mater.

Benayoune, A., Samad, A.A.A., Trikha, D.N., Abang Ali, A.A., Ashrabov, A.A., 2006. Structural behavior of eccentrically loaded precast sandwich panels. Constr. Build. Mater.

Benayoune, A., Samad, A.A.A., Trikha, D.N., Ali, A.A.A., Ellinna, S.H.M., 2008. Flexural behavior of pre-cast concrete sandwich composite panel – Experimental and theoretical investigations. Constr. Build. Mater.

Benjamin, J., Williams, H., 1958. The behavior of one-story brick shear walls.

Bentz, E., 2005. Explaining the riddle of tension stiffening models for shear panel experiments. J. Struct. Eng.

Bertero, V., Brokken, S., 1983. Infills in Seismic Resistant Building. J. Struct. Eng.

Brignola, A., Frumento, S., Lagomarsino, S., Podestà, S., 2008. Identification of Shear Parameters of Masonry Panels Through the In-Situ Diagonal Compression Test. Int. J. Archit. Herit.

Bush, T., Stine, G., 1994. Flexural behavior of composite precast concrete sandwich panels with continuous truss connectors. PCI J.

Calderini, C., Cattari, S., Lagomarsino, S., 2010. The use of the diagonal compression test to identify the shear mechanical parameters of masonry. Constr. Build. Mater.

Calderini, C., Lagomarsino, S., 2008. Continuum model for in-plane anisotropic inelastic behavior of masonry. J. Struct. Eng.

Calvi, G.M., Bolognini, D., Penna, A., 2004. Seismic performance of masonry-infilled R.C. Frames: Benefits of slight reinforcements, in: 6th Portoguese Congress on Seismology and Earthquake Engineering.

Cavaleri, L., Fossetti, M., and Papia, M., 2005. Infilled frames: developments in the evaluation of cyclic behavior under lateral loads. Structural Engineering and Mechanics. 21:4, 469-494.

CEN., 2003a. Eurocode 8: Design of structures for earthquake resistance - Part 1: General rules, seismic actions and rules for buildings, prEN 1998-1, December 2003, Brussels.

Cervera, M., Oliver, J., Faria, R., 1995. Seismic evaluation of concrete dams via continuum damage models. Earthq. Eng. Struct. Dyn., 24(9), 1225-1245.

Chen, W. F., Saleeb, A. F., 1982. Constitutive equations for engineering materials (Vol. 1, p. 580). New York: Wiley.

Chioccarelli, E., Iervolino, I., 2010. Near-source seismic demand and pulse-like records : A discussion for L ' Aquila earthquake. Earthq. Eng. Struct. Dyn. 39, 1039–1062.

Chopra, A.K., Goel, R.K., 2002. A modal pushover analysis procedure for estimating seismic demands for buildings. Earthq. Eng. Struct. Dyn. 31, 561–582.

Colangelo, F., 2005. Pseudo-dynamic seismic response of reinforced concrete frames infilled with non-structural brick masonry. Earthq. Eng. Struct. Dyn. 34, 1219–1241.

Collins, M.P., Mitchell, D., 1991. Prestressed concrete structures. Prentice Hall, Englewood Cliffs

Crisafulli, F.J., 1997. Seismic behavior of reinforced concrete structures with masonry infills. Civ. Eng.

Crisafulli, F.J., Carr, A.J., 2007. Proposed macro-model for the analysis of infilled frame structures. Bull. New Zeal. Soc. Earthq. Eng. 40, 69–77.

Crisafulli, F., Carr, A., Park, R., 2000. Analytical modelling of infilled frame structures-a general review. Bull. New Zeal. Soc. Earthq. Eng.

Das, D., Murty, C.V.R., 2004. Brick masonry infills in seismic design of RC framed buildings : Part 1 — Cost implications 39–44.

Dawe, J.L., Seah, C.K., 1989. Behavior of masonry infilled steel frames. Can. J. Civ. Eng.

Decreto Ministeriale 26-03-1980 (1980), Norme tecniche per l'esecuzione delle opere in cemento armato normale, precompresso e per le strutture metalliche, Gazzetta Ufficiale 28-06-1980 n.176 (in Italian)

Decreto Ministeriale 3-03-1975 N. 40 (1975), Disposizioni concernenti l'applicazione delle norme tecniche per le costruzioni in zone sismiche, Gazzetta Ufficiale 8-4-1975, n. 93 - suppl, Italy (in Italian)

Dhanasekhar, M., Page, A., 1986. The influence of brick masonry infill properties on the behavior of infilled frames. ICE Proc.

Dolce, M., Cardone, D., Ponzo, F. C., Valente, C. 2005. Shaking table tests on reinforced concrete frames without and with passive control systems. Earthquake engineering & structural dynamics, 34(14), 1687-1717.

Durrani, A., Haider, S., 1996. Seismic response of RC frames with unreinforced masonry infills. 14th World Conf. Earthq. Eng.

Dvorkin, E. N., & Bathe, K. J., 1984. A continuum mechanics based four-node shell element for general non-linear analysis. Engineering computations, 1(1), 77-88.

Einea, A., Salmon, D., Tadros, M., Culp, T., 1994. A new structurally and thermally efficient precast sandwich panel system. PCI J.

Fib Bulletin 24, 2003. Seismic assessment and retrofit of reinforced concrete buildings, International Federation du Beton, Lausanne, Switzerland.

Kachanov, L., 1986. Introduction to continuum damage mechanics. Vol. 10. Springer, 1986.

Kappos, A. J., Ellul, F. 2000. Seismic design and performance assessment of masonry infilled RC frames. In Proceedings of the 12th World Conference on Earthquake Engineering, Paper (No. 989).

Klingner, R. E., Bertero, V. V., 1978. Earthquake resistance of infilled frames. Journal of the structural division, 104(6), 973-989.

Fardis, M.N., Bousias, S.N., Franchioni, G., Panagiotakos, T.B., 1999. Seismic response and design of RC structures with plan-eccentric masonry infills. Earthq. Eng. Struct. Dyn. 28, 173–191.

Fardis, M.N., Panagiotakos, T.B., 1997a. Seismic design and response of bare and masonry-infilled reinforced concrete buildings. Part II: Infilled Structures. J. Earthq. Eng.

Fardis, M.N., Panagiotakos, T.B., 1997b. Seismic design and response of bare and masonry-infilled reinforced concrete buildings. Part I: Bare Structures. J. Earthq. Eng.

Faria, R., Oliver, J., Cervera, M., 1998a. A strain-based plastic viscous-damage model for massive concrete structures. Int. J. Solids Struct. 35, 1533–1558.

Faria, R., Oliver, J., Cervera, M., 1998b. A strain-based plastic viscous-damage model for massive concrete structures. Int. J. Solids Struct.

Filippou, F., Popov, E., Bertero, V., 1983. Effects of bond deterioration on hysteretic behavior of reinforced concrete joints.

Flanagan, R., Bennett, R., 1999. In-plane behavior of structural clay tile infilled frames. J. Struct. Eng.

Flanagan, R., Bennett, R., Barclay, G., 1992. Experimental testing of hollow clay tile infilled frames.

Gambarotta, L., Lagomarsino, S., 1997. Damage model for the seismic response of brick masonry shear walls. Part I: the mortar joint model and its applications. Earthq. Eng. Struct. Dyn. 26, 423–439.

Gil-Martín, L., 2009. Refinements to compression field theory, with application to wall-type structures. ACI Special Publication, 265

Gopalaratnam, V., Shah, S., 1985. Softening response of plain concrete in direct tension. ACI J. Proc.

Goulet, C. A., Haselton, C. B., Mitrani-Reiser, J., Beck, J. L., Deierlein, G. G., Porter, K. A., Stewart, J. P., 2007. Evaluation of the seismic performance of a code-conforming reinforced-concrete frame building—from seismic hazard to collapse safety and economic losses. Earthquake Engineering & Structural Dynamics, 36(13), 1973-1997.

Gulec, C., 2005. Ultimate shear strength of squat rectangular reinforced concrete walls.

Gulec, C., Whittaker, A., Stojadinovic, B., 2008. Shear strength of squat rectangular reinforced concrete walls. ACI Struct. J.

Hashemi, S. A., and K. M. Mosalam. 2007. Seismic Evaluation of Reinforced Concrete Buildings Including Effects of Infill Masonry Walls. Pacific Earthquake Engineering Research Center.

Hashemi, A., Mosalam, K. M. 2006. Shake-table experiment on reinforced concrete structure containing masonry infill wall. Earthquake engineering & structural dynamics, 35(14), 1827-1852.

Hashemi, A., Mosalam, K.M., 2006. Shake-table experiment on reinforced concrete structure containing masonry infill wall 1827–1852.

Hendry, Arnold W., Bhek Pati Sinha, and S. R. Davies, eds. Design of masonry structures. CRC Press, 2003.

Hidalgo, P. a., Ledezma, C. a., Jordan, R.M., 2002. Seismic Behavior of Squat Reinforced Concrete Shear Walls. Earthq. Spectra 18, 287–308.

Holmberg A, Pelm E., 1986. Behavior of load bearing sandwich type structures Handout 49, State institute for construction research Lund (Sweden).

Holmes, M., 1961. Steel frames with brickwork and concrete infilling. ICE Proc.

Institut canadien du béton précontraint, Mitchell, D. 1987. Prestressed concrete basics. Canadian Prestressed Concrete Institute.

Ju, J., 1989. Energy-based coupled elastoplastic damage models at finite strains. J. Eng. Mech.

Kabir, M., Hasheminasab, M., 2002. Mechanical properties of 3D wall panels under shear and flexural loading. CSCE Conf.

Kakaletsis, D.J., Karayannis, C.G., 2008. Influence of Masonry Strength and Openings on Infilled R/C Frames Under Cycling Loading. J. Earthq. Eng.

Karsan, I. D., & Jirsa, J. O., 1969. Behavior of concrete under compressive loadings. Journal of the Structural Division.

Kaushik, H.B., Rai, D.C., Jain, S.K., 2006. Code Approaches to Seismic Design of Masonry-Infilled Reinforced ConcreteFrames: A State-of-the-Art Review. Earthq. Spectra 22, 961–983.

Kent, D., Park, R., 1971. Flexural members with confined concrete. J. Struct. Div. 97(7), 1969-1990.

Koutromanos, I., Stavridis, A., Shing, P.B., Willam, K., 2011. Numerical modeling of masonry-infilled RC frames subjected to seismic loads. Comput. Struct. 89(11), 1026-1037.

Kupfer, H., Hilsdorf, H., Rusch, H., 1969. Behavior of concrete under biaxial stresses. ACI J. Proc.

Lee, B.-J., Pessiki, S., 2006. Thermal performance evaluation of precast concrete three-wythe sandwich wall panels. Energy Build.

Lee, J., Fenves, G.L., 1998. Plastic-Damage Model for Cyclic Loading of Concrete Structures. J. Eng. Mech. 124(8), 892-900.

Lemaitre, J., 1985. A Continuous Damage Mechanics Model for Ductile Fracture. J. Eng. Mater. Technol.

Lemaitre, J., 1994. Mechanics of solid materials.

Lemaitre, J., Chaboche, J. L. Mechanics of solid materials, 1990.

Liauw, T., Kwan, K., 1985a. Unified plastic analysis for infilled frames. J. Struct. Eng.

Liauw, T., Kwan, K., 1985b. Static and cyclic behaviors of multistorey infilled frames with different interface conditions. J. Sound Vib.

Lowes, L.N., Lehman, D.E., Birely, A.C., Kuchma, D.A., Hart, C.R., Marley, K.P., 2010. Behavior , Analysis , and Design of Complex Wall Systems.

Lubliner, J., Oliver, J., Oller, S., Oñate, E., 1989. A plastic-damage model for concrete. Int. J. Solids Struct.

Madan, A., Reinhorn, A.M., Mander, J.B., Valles, R.E., 1997. Modeling of Masonry Infill Panels for Structural Analysis. J. Struct. Eng.

Magenes, G., Pampanin, S., 2004. Seismic response of gravity-load designed frame systems with masonry infills.

Mainstone, R., Weeks, G., 1972. The influence of a bounding frame on the racking stiffness and strengths of brick walls.

Mander, J., Nair, B., Wojtkowski, K., Ma, J., 1993. An experimental study on the seismic performance of brick-infilled steel frames with and without retrofit. Tech. Rep.

Manfredi, G., Masi, A., Pinho, R., Verderame,G.And Vona, M., 2007. Valutazione degli edifici esistenti in Cemento Armato,IUSS Press, Pavia, Italy. (in Italian)

Mazars, J., 1986 A model of unilateral elastic damageable material and its application to concrete. Fracture Toughness and Fracture Energy of Concrete, Elsevier, New York (1986): 61-71.

Mazars, J., Pijaudier-Cabot, G., 1989. Continuum damage theory-application to concrete. Journal of Engineering Mechanics, 115(2), 345-365.

Mansour, M., Hsu, T., 2005a. Behavior of reinforced concrete elements under cyclic shear. I: Experiments. J. Struct. Eng.

Mansour, M., Hsu, T., 2005b. Behavior of reinforced concrete elements under cyclic shear. II: Theoretical model. J. Struct. Eng.

Martín-Pérez, B., Pantazopoulou, S.J., 2001. Effect of bond, aggregate interlock and dowel action on the shear strength degradation of reinforced concrete. Eng. Struct.

Massone, L., 2009. Modelling of Squat Structural Walls Controlled by Shear. ACI Struct. J.

Massone, L., Orakcal, K., Wallace, J., 2006. Shear-flexure interaction for structural walls. ACI Spec. Publ.

Mazzoni, S., McKenna, F., Scott, M. H., Fenves, G. L. 2006. OpenSees command language manual. Pacific Earthquake Engineering Research (PEER) Center.

Mehrabi, A., Shing, P., 1997. Finite element modeling of masonry-infilled RC frames. J. Struct. Eng.

Mehrabi, A., Shing, P., Schuller, M., Noland, J., 1994. Performance of masonry-infilled R/C frames under in-plane lateral loads.

Mehrabi, A. B., Benson Shing, P., Schuller, M. P., Noland, J. L. 1996. Experimental evaluation of masonry-infilled RC frames. Journal of Structural engineering, 122(3), 228-237.

Mehta, P. K., Monteiro, P. J., 1993. Concrete. Structure, Properties, and Materials. 2nd ed. Englewood Cliffs: Pretince.

Moghaddam, H. A., & Dowling, P. J. 1987. The state of the art in infilled frames. Imperial College of Science and Technology, Civil Engineering Department.

Mohamad, N., Muhammad, H.M., 2011. Testing of Precast Lightweight Foamed Concrete Sandwich Panel with Single and Double Symmetrical Shear Truss Connectors under Eccentric Loading. Adv. Mater. Res.

Mörsch, E., 1922. Der, Eisenbetonbau (Reinforced concrete construction). Verlag von Konrad Wittwer, Stuttgart.

Mosalam, K., 1996. Experimental and computational strategies for the seismic behavior evaluation of frames with infill walls.

Mosalam, K. M., Ayala, G., White, R. N., Roth, C. 1997. Seismic fragility of LRC frames with and without masonry infill walls. Journal of Earthquake Engineering, 1(4), 693-720.

Mosalam, K. M., White, R. N., Gergely, P. 1997. Static response of infilled frames using quasi-static experimentation. Journal of Structural Engineering, 123(11), 1462-4169..

Naito, C., Hoemann, J., Beacraft, M., Bewick, B., 2012. Performance and Characterization of Shear Ties for Use in Insulated Precast Concrete Sandwich Wall Panels. J. Struct. Eng.

Negro, P., Colombo, A., 1997. Irregularities induced by nonstructural masonry panels in framed buildings. Eng. Struct.

Negro, P., Verzeletti, G. 1996. Effect of infills on the global behavior of R/C frames: energy considerations from pseudodynamic tests. Earthquake engineering & structural dynamics, 25(8), 753-773.

Orakcal, K., Sanchez, L., Wallace, J., 2006. Analytical modeling of reinforced concrete walls for predicting flexural and coupled-shear-flexural responses. Pacific Earthquake Engineering Research Center, College of Engineering, University of California, Berkeley.

Orakcal, K., Wallace, J., 2006. Flexural modeling of reinforced concrete walls-experimental verification. ACI Struct. J.

Page, A. W., 1978. Finite Element Model for Masonry, Journal Str. Div., Proc. ASCE, Vol. 104, No ST8, 1978, pp. 1267-1285.

Palermo, M., Gil-Martín, L.M., Trombetti, T., Hernández-Montes, E., 2012. In-plane shear behavior of thin low reinforced concrete panels for earthquake re-construction. Mater. Struct. 46, 841–856.

Paredes, J.A., Barbat, A.H., Oller, S., 2011. A compression–tension concrete damage model, applied to a wind turbine reinforced concrete tower. Eng. Struct.

Paulay, T., Priestley, M., Synge, A., 1982. Ductility in earthquake resisting squat shearwalls. ACI J. Proc.

Paulay, T., Priestley, M.J.N., 1992. Seismic Design of Reinforced Concrete and Masonry Buildings, Structural Safety.

PCI Committee on Precast Concrete Sandwich Wall Panels, 1997. State of the art of precast/prestresses sandwich wall panels. PCI J 1997;42(2):92–133.

Pessiki, S., Mlynarczyk, A., 2003. Experimental Evaluation of the Composite Behavior of Precast Concrete Sandwich Wall Panels. PCI J. 48, 54–71.

Polyakov, S., 1960. On the interaction between masonry filler walls and enclosing frame when loaded in the plane of the wall. Transl. Earthq. Eng.

Pramono, E., Willam, K., 1989. Fracture energy-based plasticity formulation of plain concrete. Journal of engineering mechanics, 115(6), 1183-1204.

Raffa, A. 2012. Primi sviluppi per la concezione di tamponamenti in laterizio "antisismici". Master thesis, Department DICAM, University of Bologna, Bologna.

Ramirez, J.A., Dilger, W.H., 2000. ACI 445R-99 Recent Approaches to Shear Design of Structural Concrete Reported by Joint ACI-ASCE Committee 445 1–55.

Rezaifar, O., Kabir, M., Taribakhsh, M., Tehranian, A., 2008. Dynamic behavior of 3D-panel single-storey system using shaking table testing. Eng. Struct.

Ricci, I., Palermo, M., Gasparini, G., Silvestri, S., Trombetti, T., 2013. Results of pseudo-static tests with cyclic horizontal load on cast in situ sandwich squat concrete walls. Engineering Structures, 54, 131-149.

Ricci, I., 2012. Sistemi strutturali cellulari a pareti portanti in cemento armato gettato in opera realizzate con la tecnologia del pannello di supporto in polistirene, Ph.D Thesis, Department DICAM, University of Bologna; Bologna.http://amsdottorato.cib.unibo.it/4886/.

Rosman R., 1964. Approximate analysis of shear walls subjected to lateral loads. Proc J Am Concr Inst;61:717–33.

Ritter, K., Engineer, S., 1899. Die bauweise hennebique.

Sabetta, F., Pugliese, A., 1996. Estimation of Response Spectra and Simulation of Nonstationary Earthquake Ground Motions. Bull. Seismol. Soc. Am. 86, 337–352.

Salmon, D., Einea, A., Tadros, M., Culp, T., 1997. Full scale testing of precast concrete sandwich panels. ACI Struct. J.

Scotta, R., Tesser, L., Vitaliani, R., & Saetta, A. (2009). Global damage indexes for the seismic performance assessement of RC structures. Earthquake Engineering & Structural Dynamics, 38(8), 1027-1049.

Scotta, R., Vitaliani, R., Saetta, A., Oñate, E., Hanganu, A., 2001. A scalar damage model with a shear retention factor for the analysis of reinforced concrete structures: theory and validation. Comput. Struct. 79, 737–755.

Sezen, H., Moehle, J.P., 2004. Strength and Deformation Capacity of Reinforced Concrete columns with Limited Ductility, in: Proceedings of the 13th World Conference on Earthquake Engineering.

Shing, P.B., Mehrabi, A.B., 2002. Behavior and analysis of masonry-infilled frames. Prog. Struct. Eng. Mater. 4, 320–331.

Simo, J.C., Ju, J.W., 1989a. Strain- and stress-based continuum damage models—II. Computational aspects. Math. Comput. Model.

Simo, J.C., Ju, J.W., 1989b. Strain- and stress-based continuum damage models—I. Formulation. Math. Comput. Model.

Smith, B., Carter, C., 1969. A method of analysis for infilled frames. ICE Proc.

Smith, B.S., 1962a. Lateral stiffness of infilled frames. J. Struct. Div., ASCE.

Smith, B.S., 1962b. Lateral stiffness of infilled frames. J. Struct. Div., ASCE.

Smith, B.S., 1967. Methods for predicting the lateral stiffness and strength of multi-storey infilled frames. Build. Sci.

Stafford Smith, B., 1967. Methods for predicting the lateral stiffness and strength of multi-storey infilled frames. Build. Sci.

Stafford-Smith, B., 1966. Behavior of square infilled frames. ASCE J. Struct. Div.

Stefano, M. De, Tanganelli, M., Viti, S., 2013. On the variability of concrete strength as a source of irregularity in elevation for existing RC buildings: a case study. Bull. Earthq. Eng.

Tamai, S., 1988. Average stress-strain relationship in post yield range of steel bar in concrete. Concr. Lib. JSCE.

Tanganelli, M., Viti, S., De Stefano, M., Reinhorn, A. M. 2013. Influence of Infill Panels on the Seismic Response of Existing RC Buildings: A Case Study. In Seismic Behavior and Design of Irregular and Complex Civil Structures (pp. 119-133). Springer Netherlands.

Tesser, L., Filippou, F. C., Talledo, D. A., Scotta, R., & Vitaliani, R. (2011). Nonlinear analysis of R/C panels by a two parameter concrete damage model. In III ECCOMAS Thematic Conference on Computational Methods in Structural Dynamics and Earthquake Engineering (pp. 25-28).

Trombetti, T., Silvestri, S., Gasparini, G., 2012. Results of Pseudo-Static Tests with Cyclic Horizontal Load on Concrete/Polystyrene Sandwich Bearing Panels with and without Openings, in: Strategi Di Sviluppo Sostenibile per Le Costruzioni in Cina, in Europa, E in Italia. pp. 509–518.

Tzmatzis, A., Asteris, P., 2003. Finite element analysis of masonry structures: Part I: Review of previous work. 9th North Am. Mason. Conf. 101–111.

UNI, EN. 772-1:(2002), 2002. Tests guidelines for masonry members–Compressive strength.

Vamvatsikos, D., Cornell, C.A., 2002. Incremental dynamic analysis. Earthq. Eng. Struct. Dyn. 31, 491–514.

Vecchio, F.J., Collins, M.P., 1986. The Modified Compression Field Theory for reinforced concrete elements subjected to shear. ACI Struct. J. 83, 925–933.

Verderame, G.M, Iervolino, I., Ricci, P. , 2009. Report on the damages on buildings following the seismic event of 6th of april 2009, V1.20 available on http://www.reluis.it

Whyte, C.A., Stojadinovic, B., 2013. Hybrid Simulation of the Seismic Response of Squat Reinforced Concrete Shear Walls. Pacific Earthquake Engineering.

Wood, R., 1978. Plasticity, composite action and collapse design of unreinforced shear wall panels in frames. ICE Proc.

Wu, J.Y., Li, J., Faria, R., 2006. An energy release rate-based plastic-damage model for concrete. Int. J. Solids Struct. 43, 583–612.

Yazdani, S., and H. L. Schreyer. "Combined plasticity and damage mechanics model for plain concrete." Journal of engineering mechanics 116.7 (1990): 1435-1450.

Žarnić, R., Gostič, S., Crewe, A. J., Taylor, C. A. 2001. Shaking table tests of 1: 4 reduced-scale models of masonry infilled reinforced concrete frame buildings. Earthquake engineering & structural dynamics, 30(6), 819-834.

Zarnic, R., Tomazevic, M., 1990. Behavior of Repaired Masonry Infilled R/C Frames. A Rep. to US-Yugoslav Jt. Board Sci.